UNIVERSITÀ
DEGLI STUDI
DI PADOVA

Sede Amministrativa: Università degli Studi di Padova

Dipartimento di
Fisica e Astronomia ”G. Galilei”

CORSO DI DOTTORATO DI RICERCA IN: FISICA

CICLO: XXX

DEVELOPMENT AND ANALYSIS OF N-TYPE DOPING PROCESSES FOR HIGH PURITY GERMANIUM

Coordinatore: Ch.mo Prof. Gianguido Dall’Agata
Supervisore: Prof. Davide De Salvador

Dottoranda: Virginia Boldrini

"Ogni giorno l'orizzonte un po' più in là."

Claudio Pellizzeni

"Every day the horizon a little further on."

Claudio Pellizzeni

Abstract

After a period of low interest, in the last two decades germanium has become one of the most studied semiconductors and now it is applied in many research fields such as microelectronics, photonics, solar energy and radiation detectors. The small bandgap, the high charge carrier mobility and its availability also with high purity are appealing properties that make Ge more suitable than Si in many cases. The tendency toward a scaling of devices and the continuous improvement of performances require higher doping levels and thinner junctions. Hence, a great effort is demanded to find new doping technologies.
The first aim of this work is the implementation of conventional and innovative doping processes on Ge, in order to achieve homogeneously doped layers characterized by a high density of electrically active doping atoms and no lattice damages. In parallel, another purpose is to satisfy a compelling open question that has arisen in the field of gamma detector research: the development of a suitable doping process to form a segmentable n-type contact on high purity Ge (HPGe), with negligible leakage under reverse bias.
In HPGe gamma detectors, which are big diodes, the n-type contact has been done by low-temperature diffusion of Li for 40 years. Lithium diffusion produces a thick (0.5 mm) doped region that is not effective in gamma collection (dead layer). The need to segment both contacts in order to permit gamma-ray tracking requires a change, since a thick contact is difficult to be segmented. Beside, Li would diffuse under low temperature annealing used to recover the radiation damage, thus compromising the isolation between segments.
In this work some doping technique have been applied to Ge and HPGe, in particular P spin-on diffusion, Sb diffusion from sputtered sources and Sb diffusion by laser thermal annealing. Many characterization techniques were used to evaluate morphological and electrical properties of doped layers and in all the cases, after optimization of the processes, continuous n^+ contacts were obtained.
After this crucial step, the doping methods were tested in order to understand if they alter the purity of HPGe material. For all treated HPGe samples, a characteri-

zation of electrically active contaminant concentration into the pure bulk has been carried out. A phenomenological model describing the contamination process under conventional annealing treatments was developed and used to asses solid-state diffusion doping processes. It turned out that out-of-equilibrium doping processes have higher possibilities to be successfully employed for the formation of HPGe n contacts, maintaining the purity.
Among them, laser thermal annealing results to be the most promising and finally, a preliminary p-HPGe small diode prototype was fabricated with such technique and successfully tested as a gamma-ray detector.

Contents

Introduction **v**

1 Interdisciplinary background **1**
1.1 Germanium doping applications 1
1.1.1 Microelectronics 2
1.1.2 Optoelectronics 4
1.1.3 Solar energy 7
1.2 Impurity diffusion in semiconductors 8
1.2.1 Fick's laws of diffusion and concentration profiles 8
1.2.2 Lattice defects 11
1.2.3 Impurity diffusion mediated by point-defects 13
1.2.4 Diffusion in germanium 16
1.2.5 Out-of-equilibrium diffusion through laser annealing 17
1.3 γ-ray detection 18
1.3.1 Photon interaction with matter 18
1.3.2 High purity germanium detectors: operation principle 23
1.3.3 HPGe detector contacts 26
1.3.4 Surface passivation 27
1.3.5 Detector configurations: from single shapes to detector arrays 28

2 Characterization techniques **33**
2.1 Imaging techniques 34
2.1.1 Scanning Electron Microscopy (SEM) 34
2.1.2 Atomic Force Microscopy (AFM) 36
2.2 Secondary Ion Mass Spectrometry (SIMS) 37
2.3 Rutherford Backscattering Spectrometry (RBS) 39
2.4 Van der Pauw electrical measurements 40
2.4.1 Setup description 44
2.4.2 Measurement protocol 48
2.4.3 COMSOL® modeling 51
2.4.4 Joint analysis of sheet resistance and SIMS profile 55

3 Optimal process parameters for P spin-on-doping of Ge **57**
3.1 Sample preparation . . . 58
3.1.1 Spin-coating of the source film . . . 58
3.1.2 Source film reticulation through curing . . . 60
3.2 Characterization and results . . . 62
3.2.1 Effects of environmental moisture on Ge surface in-processing 63
3.2.2 Curing time and temperature . . . 67
3.2.3 P spin-on doping at different temperatures . . . 72
3.2.4 Analysis of diffusion activation energy . . . 74
3.3 Conclusions . . . 75

4 Sb doping from sputtered sources **77**
4.1 Experimental . . . 78
4.1.1 Sb diffusion from sputtered sources in furnace . . . 78
4.1.2 Sb diffusion from sputtered source by LTA . . . 80
4.2 Results and discussion . . . 82
4.2.1 Sb diffusion in furnace from direct source . . . 82
4.2.2 Sb diffusion in furnace from remote source . . . 84
4.2.3 Sb diffusion via laser thermal annealing . . . 89
4.3 Conclusions . . . 93

5 Characterization of thermally-induced doping defects in bulk HPGe **95**
5.1 Experimental . . . 96
5.1.1 Sample preparation . . . 96
5.1.2 Contact formation for electrical measurements . . . 98
5.1.3 Setups for electrical measurements at low temperature . . . 100
5.2 Results and discussion . . . 101
5.2.1 Experimental data . . . 101
5.2.2 Resistance theoretical curves . . . 102
5.2.3 Contaminant concentration analyses . . . 105
5.2.4 Phenomenological model of contamination process . . . 109
5.2.5 Process window for standard doping annealing . . . 114
5.3 Conclusions . . . 116

6 Preliminary diode prototype in HPGe **119**
6.1 Experimental . . . 120
6.1.1 Sample preparation . . . 120
6.1.2 Measurement setup for diode and detector characterizations . 121
6.2 Results . . . 122
6.2.1 I/V diode characterization . . . 123
6.2.2 Detector operation test . . . 125

6.3 Conclusions 128

Conclusions **131**

Appendix **135**

List of publications **139**

References **141**

Acknowledgments **155**

Introduction

During the pioneering years of semiconductor electronics, a vast amount of exploration of basic devices and material physics was carried out on germanium, because in the mid-1900s it was available with the best crystalline quality achievable. This led to the formulation of several important theories and physical principles. At the same time and even earlier, the photo response properties of germanium were discovered. Thanks to its small bandgap (0.661 eV) it provides an optimum responsivity toward the near infrared. In 1960, when Ge started to be replaced by Si in the electronics industry, contemporary Ge-based radiation detectors were developed. Particularly devoted to gamma-ray revelation in the field of nuclear research, this kind of detectors exploited many of the electrical and physical properties of Ge: high pureness, small bandgap, high carrier mobility and, last but not least, relatively high Z to promote photon-matter interaction.

After a period of disinterest, in the last two decades a renewed interest has grown toward Ge in many application fields, thanks to its appealing properties. Indeed it is used in solar cells, photodiodes, LEDs, and other optoelectronic devices. Unfortunately, the current Si-based technology is already very close to the physical limits of scaling, because of difficulties in production processes and intrinsic problems such as *short-channel effects*, *thermal noise voltage* and *parasitic effects*. Electronics scientific research is taking a huge effort to experiment new technological routes based on completely different structures and physical phenomena. However, in order not to stop the continuous improvement of device performances in immediate future, it could be more feasible to pass to another material characterized by higher charge carrier mobility and easily integrable inside silicon IC platforms. In this respect, Ge is one of the most promising materials due to its charge carrier mobilities, which are about a factor 2 higher for electrons and a factor 4 for holes than those of Si at the highest carrier concentrations.

The aims of this thesis are manifold. Firstly, the implementation of conventional and innovative doping processes on Ge, with the purpose of achieving homogeneously doped layers, characterized by a high density of electrically active doping

atoms and no lattice damages. In parallel, our intent is to satisfy a compelling open question that has arisen in the field of gamma detector research: the development of a suitable doping process to form a segmentable n-type contact on High Purity Ge (HPGe), with negligible leakage under reverse bias.
Gamma-ray detectors are big cylindric diodes made of HPGe (10^{10} at/cm^3 growth impurity density), with two highly-doped surface contacts of p- and n-type, one acting as a rectifying contact since it forms a p-n junction with the bulk and the other acting as ohmic contact and barrier against the injection of minority carriers. Recently, in order to perform a refined gamma spectroscopy, big detectors composed of a spherical array of HPGe segmented diodes allowing ray-tracking (i.e. trajectory reconstruction) have been designed and partially produced. Since the late 1970s, Li diffusion (for n-doping) and B ion implantation (for p-doping) techniques are used for the contact formation. However, thick Li-diffused layers are undesired dead layers for gamma revelation and, moreover, Li high diffusivity prevents the possibility to refine the contact segmentation. Therefore, further research is needed to develop new doping processes specifically tested on HPGe that allow the substitution of Li diffusion.

The first two chapters of the thesis are dedicated to introduce the topics and the techniques:
Chapter 1 reviews the interdisciplinary background at the basis of this work. A brief description of impurity diffusion models in semiconductors is reported, for both equilibrium and out-of-equilibrium diffusions. The application fields of Ge doping processes are described in the second part of the chapter, with particular emphasis on HPGe detectors.
In chapter 2 all the characterization techniques that have been used to test the main properties of the fabricated doped layers are introduced. A particular focus is done on four-wire electrical measurements, a fundamental technique used to measure the electrical activation in doped layers. The implementation of such technique was started with my thesis and it was an important part of my activity.

In the following two chapters, the optimization and implementation of different n-doping techniques in Ge was performed, this part of the thesis is useful for both the general topic of Ge doping and the specific task of HPGe new contact development.
Chapter 3 describes the phosphorus Spin-On Diffusion (SOD) doping technique, well known in Si-technology but rarely applied to Ge. All steps and process

parameters in the experimental protocol have been optimized in order to obtain optimum results also on Ge.
Chapter 4 introduces equilibrium and out-of-equilibrium antimony diffusion from sputtered sources. The equilibrium annealing process was optimized in order to avoid the formation of surface defects, induced when the sputtered source is in direct contact with Ge. We also successfully doped Ge by Laser Thermal Annealing (LTA), using an ultra thin Sb layer (2nm) as a source. Such technique exploits the very high diffusivity of Sb in a molten surface layer that is formed for a very short time (100 ns) at the Ge surface, after a fast (10 ns) laser process. The results of characterizations in terms of chemical profile and electrical activation are included.

In chapter 5 the above processes were tested to answer a crucial question about their applicability to HPGe material: does the process change the purity of the material? This is a particularly intriguing problem. Suppose to have a cube cm of HPGe, the amount of (electrically active) atoms sufficient to contaminate is of the order of 10^{10} cm^{-3}, less than 1 atom over 10^{12} that is 0.001 ppb. Chapter 5 reports the characterization of thermally-induced doping defects in HPGe. We did it by directly looking at their effect on electrical properties of the bulk, since a direct measure of such small atom content is hard to be performed by other methods. We demonstrated that conventional equilibrium thermal-annealing processes, used to dope the surface, promote also the diffusion and activation of contaminant doping defects inside the bulk. The fact that such phenomenon occurs only after annealing, even if the surface doping is not performed, demonstrate that the contamination comes or from the furnace or from the external environment.
A simple empirical model has been written to evaluate this phenomenon. Assessment of conventional thermal annealing doping techniques demonstrated that they would hardly satisfy the purity requirement for HPGe detector fabrication. Instead laser annealing, that is an out-of-equilibrium process, maintains the bulk substantially unaffected.

In chapter 6 the fabrication of a preliminary diode prototype, whose n-contact has been done by LTA of antimony has been described. The operation of this prototype, first as a diode and then as a gamma-ray detector, has been tested and all results are presented. In particular, an optimum energy resolution of 0.62 keV is obtained for the 59.4 keV photopeak of ^{241}Am, and very good resolutions were exhibited even at higher gamma-ray energies of 300-400 keV for ^{133}Ba and ^{152}Eu sources.

Finally, in appendix, the diode characterization of a p-n junction created in HPGe with the technique of P spin-on diffusion is described.

Chapter 1

Interdisciplinary background

In paragraph 1.1 a short description of many possible applications of Germanium semiconductor will be introduced. All such applications deals with the control of doping that strictly depends on the understanding of diffusion mechanisms. Paragraph 1.2 will be devoted to the description of basic concepts concerning diffusion and the actual knowledge of such mechanisms in germanium. In Paragraph 1.3 a description of germanium based gamma detector will be reported. Doping control in such devices is the main aim of the present thesis.

1.1 Germanium doping applications

The peculiar behaviour of semiconductors, that is, the decrease of resistance with temperature, was first observed by Michael Faraday in 1833. After that discovery, many scientists were interested in that kind of material and made experiments that led them to observe numerous new phenomena, in particular the rectifying electrical behaviour and photoconduction [1]. It was soon understood that many semiconductor properties were strongly modified by the presence of traces of other elements within the semiconductor itself. In fact, Shelford Bidwell in 1885 and the German scientist Bernhard Gudden in 1930, each independently reported that the properties of semiconductors were due to the impurities contained within them [2, 3]. In the first four decades of the twentieth century, the semiconductor study was aimed at the construction of communication and detecting devices, such as radio and radar systems. In fact, while he was working on radars, during the II world war, John Robert Woodyard formally developed the semiconductor doping process and published it in 1950 with a US patent [4]. Almost simultaneously at Bell Labs, Sparks was doing researches on doping and he published an US patent in 1953 entitled

Method of Making P-N Junctions in Semiconductor Materials [5]. Meanwhile, in 1947, Bardeen, Brattain and Shockley built the first transistor, made of germanium: they observed that when two gold point contacts were applied to a Ge crystal, a signal was produced with the output power greater than the input [6]. Surely this discovery was the first milestone in the development of modern electronics. Apart for radios, radars and electronic devices, the doping of semiconductor led to many other applications during the twentieth century. In the field of optoelectronics, starting from a p-n junction, fundamental devices were built such as photodiodes, LEDs (Nobel Prize in Physics in 2014) and laser diodes. In the field of solar energy physics, the basic p-n junction is used to build photovoltaic cells. In the field of nuclear physics, diodes in high purity Ge operates as gamma-ray detectors (thoroughly described in Paragraph 1.3.2). This kind of device is the key example of how much impurity control in semiconductor is crucial. Large volume of active material are only obtainable thanks to purity level below 1 doping atom over 10^{12} atoms, probably the highest purity material in absolute. As will be shown, the challenge for improving such device is the development of doping processes that allow to keep such purity level.

1.1.1 Microelectronics

The scaling of Si-based metal-oxide-semiconductor (MOS) devices is approaching its technological and fundamental limits, thus new materials are needed to further improve the performances of integrated circuits (IC). Germanium was the semiconductor used in 1947 to build the first transistor, but then it was quickly supplanted by silicon, mainly due to the remarkable properties of Si oxide. SiO_2 is stable over time, it offers an optimum Si surface passivation and is a high-quality gate insulator. Ge doesn't have a stable oxide that can passivate its surface: GeO is volatile at 400 °C and GeO_2 is water-soluble and hygroscopic. Despite this, other Ge properties such as its high electron and hole mobilities and its small bandgap should allow to boost the drive current of transistors and carry out a further scaling in size and in the drain supply voltage V_{DD}. For these reasons, Ge is gaining a renewed interest for its high potential in IC applications and now it is regarded as a potential substitute for silicon.
For what concerns the gate insulator, research is doing a great effort to find a high-*k* dielectric compatible with Ge. For a material to be suitable as a gate dielectric replacement, it needs to satisfy several requirements, including high permittivity, sufficiently large band gap and proper band alignment to the semiconductor (with

1 eV offset to both bands), thermodynamic stability, good film morphology, and high interface quality. The latter properties are not easy to achieve because of the inevitable presence of instable GeO between Ge surface and the dielectric layer: during thermal annealing for the stack curing, over 400 °C, GeO degradates and evaporates damaging the interface. Some high-*k* dielectrics have been found to be not reactive with Ge, such as $LaYO_x$ [7] and the perovskite dielectric $SrHfO_3$ [8], the latter being also characterized by a low interface trap density (that represents the number of trapped charges per cm^2 per eV). Being known the optimal capping property of Si compounds over GeO during high temperature annealings [9], the use of an adequate capping layer such as $NiSi_x$ gate electrode has been suggested [7]. The matter of surface passivation is crucial in electronic devices. It concerns the reduction of the defect concentration at any interface, but also the neutralization of charged states present all over the surface. Another issue related to the dielectric choice is the presence of leakage current across the dielectric in the channel-off state (I_{off}). The leakage is due to the small bandgap of Ge (0.67 eV) and to the fact that the thickness of the gate oxide has become smaller than the limit for electron tunneling (3 nm). To solve this problem a gate dielectric with a conduction band offset $>$1 eV on Ge should be found. Since it seems that no single dielectric material can achieve everything required for an excellent gate stack, composite gate stacks could provide some much needed flexibility [10].

To achieve high performances in Ge-CMOS technology, another challenge should be faced regarding Ge doping. There is still a difficulty in activating a high density of doping atoms in Ge, especially in case of n-type dopants. The reasons are manifold. First, there are intrinsic limits related to Ge itself, such as the maximum solid solubility of dopants achievable with conventional thermal annealings. Then, there are the technological limits related to the standard doping technique employed by microelectronics industry, that is ion implantation. Ion implantation can damage the lattice structure when ions impact on Ge surface with high energy. Each individual ion produces many point defects in the crystal. Besides, the kicked-off interstitials can migrate and cluster with other atoms resulting in dislocations. Even in some cases, the amount of crystallographic damage can be enough to completely amorphize the surface of the crystal. Anyway, often a complete amorphization (recoverable with a thermal treatment) is preferable to a highly damaged lattice [11]. For these reasons, ion implantation + annealing (being it conventional or rapid) don't allow to obtain a high electrical activation of dopants. New doping techniques should be explored. At the moment, the most promising one seems to be ion implantation + laser annealing: the implanted sample is irradiated by a pulsed laser beam, so that

the surface layer is molten to a depth controlled by the laser pulse energy. In this way, a homogeneous redistribution of dopants confined within the molten layer can be obtained, because of the order of magnitude larger diffusivity in the liquid with respect to the solid phase, and higher dopant activation level are expected.
A last open problem is the difficulty to achieve low-resistance ohmic contacts on n-type Ge, which are fundamental for a high drive current I_{on}. The contact resistance at the metal/n-Ge interface is high because of the *Fermi level pinning* phenomenon. Due to the presence of donor or acceptor surface states with energy inside the semiconductor band gap, the Fermi level is pinned there and a high energy barrier is established between the metal and the semiconductor. The resistance caused by this Schottky barrier can be lowered if Ge doping level is very high: in this case the barrier is narrowed and electron tunneling is enabled through it. Another strategy is that to depose an auxiliary layer between Ge and the metal, characterized by a low conduction band offset on Ge. For instance, it has been shown that TiO_2, Y_2O_3 and NiGe reduce the Schottky barrier height as well as facilitates the unpinning of Fermi-level in n-type Ge [12].

1.1.2 Optoelectronics

Photonics and optoelectronics play an essential role in many areas of communication and information technology. Silicon optoelectronic devices suffer from negligible responsivity in the near infrared (800-1600 nm range), the preferred wavelength for fiber optical systems, and from the self-absorption in waveguide structures. These issues can be overcome by a low bandgap material: Ge is the natural choice.
As regarding *photodetectors*, in the early 2000s, GeSi heterostructures were built within the view of integrating these new devices on the standard silicon substrate. These photodetectors demonstrated a successful operation in normal-incidence geometry as well as waveguide geometry [13, 14]. Nevertheless, high dark current was not negligible limiting the signal-to-noise ratio and thus, the photo-detector efficiency. The high dark current was due to several factors: surface leakage currents, point-defects induced by ion-implantation and threading dislocations induced by the Si-Ge lattice mismatch. To eliminate at least one of these factors, a photodiode made only of germanium has been fabricated recently (see Fig. 1.1). Thanks to the high doping level achieved through ion implantation + laser annealing, optimum results have been obtained: an optical responsivity of about 0.48 A/W at 1.55 μm wavelength and -1 V bias and a really low dark current value of 1 pA/μm^2 at -1 V

voltage [15].

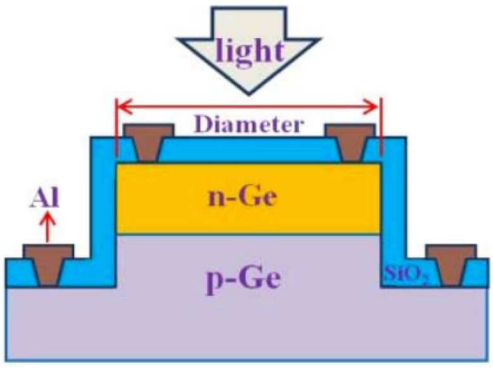

Figure 1.1. Schematic with cross-sectional view of a Ge p-n photodetector. [15]

Germanium is more suitable than Si also for applications based on electroluminescence, such as *light emitting diodes (LEDs)*, thanks to its pseudo-direct gap energy of 0.8 eV (1550 nm wavelength). But Ge is an indirect bandgap semiconductor and its use involves a greater technological effort than using direct-gap semiconductors such as GaAs, in which the recombination process with light emission is the favorite. Anyway, the difference between indirect and direct bandgap in Ge is only 136 meV and it has been shown that, by applying a tensile strain of 1.9% Ge becomes a direct bandgap material [16]. However, to favor Ge device integration on Si substrates, they are built on SiGe epitaxial layers and such a tensile strain would be too difficult to achieve. Moreover, with application of 1.9% tensile strain, the Ge direct band gap can be reduced down to 0.5 eV and the corresponding wavelength of the emitted light shifts to 2500 nm, which is far from the wavelength range used in telecommunications [17]. A more viable strategy turned out to be small tensile straining + high doping (up to $\sim 7\text{x}10^{19}$ cm^{-3}). It allows to have a high extrinsic electron population in the low-energy indirect L valleys, thus raising the Fermi level. In this way, at the same excitation level, the electron density in the Γ valley of n^+ Ge is significantly higher than in intrinsic Ge, resulting in a stronger direct gap light emission (see Fig. 1.2 [18]). Anyway, achieving such a value of active electron concentration is still a challenge, as well as avoiding the formation of point-defects and complexes of defects after Ge high doping. In fact, recently [19] the fabrication of a Ge n^+p shallow junction was reported, in which two emission peaks were seen. One due to direct bandgap luminescence, the other due to defects induced by ion implantation. Both dislocations or shallow/deep levels induced by point-defects can give rise to undesired luminescence.

In the field of data- and tele- communications, the possibility to integrate all pho-

tonic devices such as lasers, LEDs, modulators, optical fibers and photodiodes in a monolithic Si circuitry and/or CMOS technology, is really compelling. At the moment, the missing piece are laser diodes, that are IV group semiconductor lasers integrable on Si substrate. Germanium, with its pseudo-direct bandgap is the main candidate to become the active medium for electrically pumped lasing on Si. At MIT Institute in 2012 [20], the strategy to transform Ge into a direct-bandgap semiconductor through high doping + tensile strain was pursued (~4x10^{19} cm^{-3} doping level and 0.2% strain).

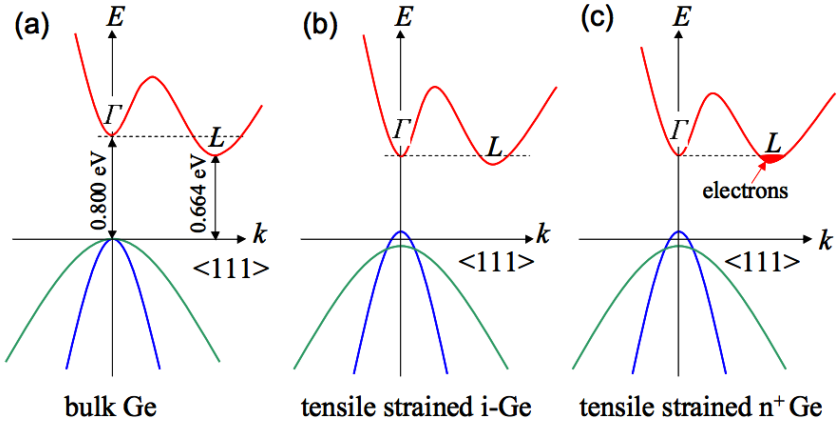

Figure 1.2. a) Schematic band structure of bulk Ge, showing its indirect gap. b) Difference between the direct and the indirect gaps can be decreased by tensile strain. c) The rest of the difference between direct and indirect gaps in tensile strained Ge can be compensated by filling electrons into the L valleys. [18]

P-doped Ge waveguide, acting as Fabry-Perot cavities, were grown inside SiO_2 trenches lying on a Si substrate. The waveguides were then covered with p^+-polySi and a metal Ti/Al stack. Laser emission wavelengths were observed between 1520 nm and 1700 nm in the different cavities, with a gain of nearly 200 nm. However, it has subsequently been shown that no real amplification corresponds to this gain, since it is completely neutralized by a strong parasitic absorption caused by the high density of charge carriers [21]. In 2015, a new technique has been used to transform Ge into a direct bandgap material [22], without introducing any mechanical strain or high density of charge carriers in order to avoid any absorption phenomena. They have grown a GeSn layer on a Ge/Si virtual substrate. An incorporation of Sn atom concentration in the range 6.5-11% should be sufficient to reduce the gap, bringing the energy of the Γ valley below that of the L valley. A strong photoluminescence with decreasing temperature has been observed, as the signature of a fundamental direct-bandgap semiconductor. For T<90 K, the observation of a threshold in emit-

ted intensity with increasing incident optical power, together with strong linewidth narrowing and a consistent longitudinal cavity mode pattern, highlighted unambiguous laser action. The laser quenching at 90 K has been related to Shockley-Reed-Hall recombination, therefore further research on surface passivation, doping and optical mode confinement would help increasing the operation temperature.

1.1.3 Solar energy

A solar cell consists of a p-n junction in which sunlight generates electron-hole pairs that are collected by the external circuit and provide electrical power. Light absorption is sensitive to the type of bandgap. Semiconductor materials with a direct gap are preferable because no phonons are required for carrier generation to take place. Besides, also the efficiency of a solar cell depends on the bandgap. In fact, if the incoming photons are too low in energy to be absorbed ($h\nu < E_G$) their energy is lost. Otherwise if they are too energetic, they must thermalize before being collected, thus some energy is lost as well.
A smart approach has been that to build solar cells made of many materials, in which the light enters and is completely absorbed while passing through layers characterized by different bandgaps. This kind of cell is called *multijunction solar cell*. Two or more thin film p-i-n junctions are stacked and connected in series. In this way, light that is not absorbed in the first junction passes to the second junction and so on. Normally, the first has the highest energy gap, it absorbs high-energy photons and transmits lower-energy photons to the other junctions. This technique is known as *spectrum splitting*. The most successful tandem

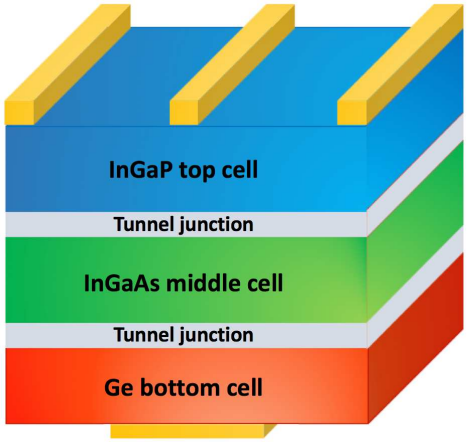

Figure 1.3. Schematic of a triple junction solar cell. The Ge junction is the bottom one because its bandgap is suitable to absorb the longest light wavelengths.

single-crystal solar cell uses Ge as a substrate. Ge has a convenient lattice constant that matches with GaAs and, in addition, its small bandgap allows to absorb longer wavelengths of light than Si. By growing thin-film epitaxial layers of III-V semiconductors on the Ge junction, a tandem cell with two or three junction can be formed. It is important to know that a tunneling junction must be located between two adjacent cells, as shown in Fig. 1.3. This junction is characterized by a very high doping level. In this way, the energy barrier is very narrow and, in reverse bias condition, charge carriers can easily cross it by tunneling. This intermediate junction is used as low-resistance contact between two adjacent cells, in order to avoid any voltage drop [23]. With the help of solar light concentration devices, multijunction cells can reach an efficiency of the 40% and, even if very expensive, they are used in those particular situations where high-efficiency energy generators are needed, for instance as in space applications.

1.2 Impurity diffusion in semiconductors

Diffusion is a process of atom migration through a solid medium. In semiconductors, that are solid crystals, diffusion is a walk through a crystal lattice. Usually it is a thermally driven process, well described by an Arrhenius or activation type of law if diffusion occurs at thermodynamic equilibrium. It means that the diffusion time should be long enough to allow the intrinsic lattice point-defects to reach an equilibrium density. Impurity diffusion is artificially carried out to build whatever kind of doped layer in semiconductors.

1.2.1 Fick's laws of diffusion and concentration profiles

Atoms in solids occupy energetically favourable sites. In equilibrium, thus in absence of any external force, they are distributed homogeneously within one continuous phase. Above the absolute zero temperature, thermal energy makes them vibrate around their lattice site, however these fluctuations cancel out on the average. When an external factor induces an inhomogeneity in the distribution, atomic movements will lead to a redistribution of species towards equilibrium conditions, to minimize the energy of the system. The first observations of such redistribution were done when the atomistic nature of solids was still ignored. Therefore, two phenomenological equations called *Fick's laws* were used to relate fluxes of atoms to the gradients of their concentrations. These formulas well describe the physics of impurity diffusion in semiconductor and are still widely used.

The concentration C is the number of atoms per unit volume. The first Fick's law of diffusion relates the flux of the species under consideration (flux that can be also considered as a diffusion current *J*) to the gradient of concentration.

$$J = -D \cdot gradC \tag{1.1}$$

Since the diffusion current is defined as the number of atoms that cross a unit area in a unit time interval, then from Eq. (1.1) it can be deduced that the dimensions of the proportionality coefficient *D*, called *diffusion coefficient*, are [l^2]/[t]. In general, the diffusion coefficient is a tensor of second rank but due to the high symmetry of crystals with diamond structure, it reduces to a scalar quantity.
But if you want to know how much the amount of a substance changes in a given volume V, upon generation, recombination and flux across the volume boundary S, you have to write an equation of continuity, where the generation and loss rates are called *G* and *R*.

$$\frac{\partial}{\partial t}\int_V C \cdot dV = \int_V (G - R) \cdot dV - \oint_S (J \bullet \overrightarrow{n}) \cdot dS \tag{1.2}$$

By applying the divergence theorem to the last term and considering infinitesimal volumes, Eq. (1.2) can be rewritten in the following form:

$$\frac{\partial C}{\partial t} = -divJ + G - R. \tag{1.3}$$

If we neglect the presence of sources and sinks by cancelling the *G* and *R* terms and use the expression of *J* given in Eq. (1.1), we obtain the second Fick's law of diffusion:

$$\frac{\partial C}{\partial t} = div(D \cdot gradC). \tag{1.4}$$

Certainly, if the coefficient *D* is independent of position it can be brought off the divergence operator. The temperature of the system has got a fundamental role in atom diffusion since it provides kinetic energy. The temperature dependence of the diffusion coefficient determined from experiments is usually found to obey an Arrhenius relation (Eq. (1.5)):

$$D = D_0 \cdot exp\left(-\frac{E_A}{k_B \cdot T}\right) \tag{1.5}$$

where D_0 is a prefactor and E_A is the activation energy of the diffusion process. The solution of Eq. (1.4), i.e. the diffusion profile of a species of atoms inside a crystal, is

dependent on the initial and boundary conditions.
If impurity atoms are present in a gas source around the semiconductor surface, then their concentration at the surface is approximately constant in time. In this first case of an inexhaustible source, the concentration profile inside the semiconductor is described by the following function:

$$C = C_{x=0} + (C_{t=0,x>0} - C_{x=0}) \cdot erf\left(\frac{x}{\sqrt{4Dt}}\right) \tag{1.6}$$

where *erf* stands for the error function (see Fig. 1.4). For the more interesting case of diffusion from the ambient gas into a crystal with null initial concentration, C(x,0)=0 is:

$$C = C_{x=0} \cdot \left(1 - erf\left(\frac{x}{\sqrt{4Dt}}\right)\right) = C_{x=0} \cdot erfc\left(\frac{x}{\sqrt{4Dt}}\right). \tag{1.7}$$

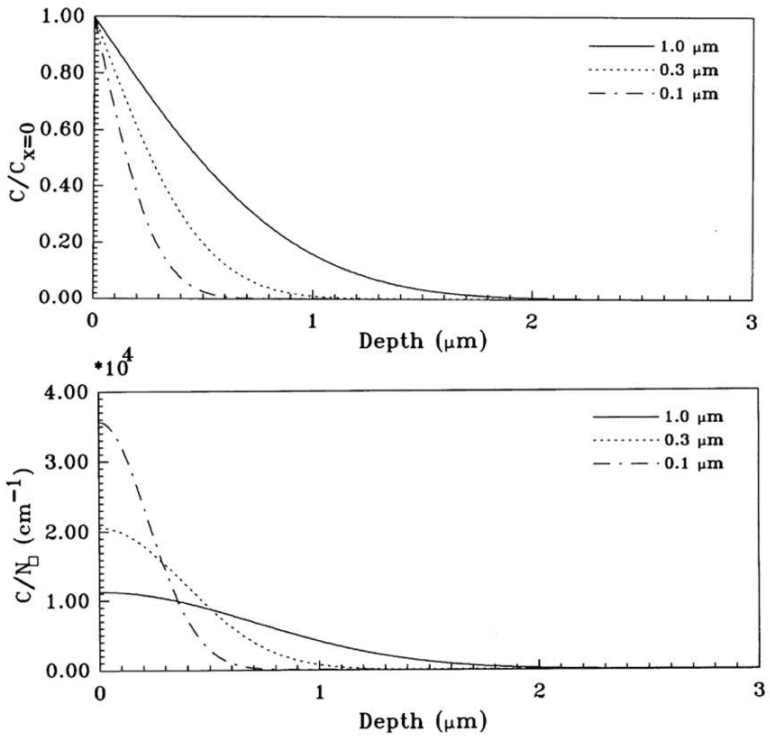

Figure 1.4. Comparison between error and gaussian functions, respectively plotted in the upper and lower part of the picture. Here they represent the impurity concentration profile inside a semiconductor. The error function (plotted for various values of $\sqrt{4Dt}$) is typical of diffusion from an inexhaustible impurity source. While the gaussian function (plotted for various values of $\sqrt{4Dt}$ as well) is typical of diffusion from a finite impurity source. [24]

Alternatively, if the source of impurities is a thin layer deposited on the semiconductor surface, containing a fixed number of atoms and describable with a delta function in x=0, then the concentration profile inside the crystal is a Gaussian distribution (see Fig. 1.4):

$$C = \frac{N}{\sqrt{\pi Dt}} \cdot exp\left(-\frac{x^2}{4Dt}\right) \tag{1.8}$$

where *N* is the total amount of material having entered the solid. It is of considerable practical importance to have some idea of how far an atom will diffuse into a solid during a diffusion experiment. An approximate estimate is given by the penetration depth, defined as the depth where an appreciable change in the concentration has occurred, after all the diffusion time t_{end} has elapsed. It can be calculated through the root mean square displacement of diffusing atoms (Eq. (1.9)) [24].

$$\sigma(t = t_{end}) = \sqrt{2Dt_{end}} \tag{1.9}$$

1.2.2 Lattice defects

Germanium has got a face-centered diamond cubic lattice. At temperature higher than 0 K, it contains native point defects as demonstrated by thermodynamic argumentations [25]. In a crystal, a point defect is defined as a deviation from the regular periodicity of the lattice in a single lattice position. Point defects can be present in a charged or neutral electronic state. Two different types of simple native point defects can occur in a pure crystal of germanium: vacancies and self-interstitials. A *vacancy* is a lattice site (normally occupied) with a missing atom. It is usually indicated with the symbol V. Vacancies can form, for instance, during the crystal growth. This defect can be in a positive, neutral or negative state depending on how the resultant unsatisfied bonds have rearranged themselves to accommodate the vacancy in the lattice. A *self-interstitial* is a germanium atom in excess in the lattice. It is an extra-atom incorporated into the structure during crystallization and it is forced to take up a position in the crystal that is not a crystal site. Both point defect types are represented in Fig. 1.5. These native defects can arise in several ways. They can be introduced during crystal growth, especially if this is rapid and crystallization is far removed from equilibrium. In particular, two mechanisms are responsible for native point defect generation: the Frenkel process and the Schottky one. The Frenkel process occurs when a Ge atom leaves spontaneously its substitutional site in a perfect crystal thus producing a vacancy. In this way the so-called Frenkel pairs, i.e. a

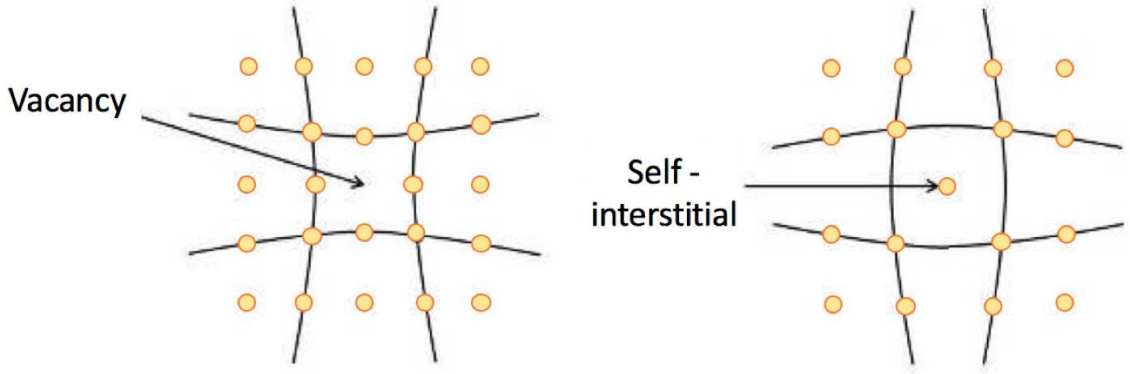

Figure 1.5. On the left a crystal lattice with an empty site is represented. This point defect is called vacancy. The drawing on the right shows an extra Ge atom positioned out of any lattice site. It is called self-interstitial. The lattice distortions indicate that the chemical-electrical bonds close to the point defect rearrange themselves to find the minimum energy configuration.

vacancy-interstitial couple is formed:

$$0 \longleftrightarrow V + I. \tag{1.10}$$

The reverse process, equally probable, is called annihilation.
The Schottky mechanism is the independent formation of vacancies and interstitials in crystals with high surface to volume ratio. What happens is that a vacancy can easily be generated in the bulk when an atom moves towards the surface. This process is thermodynamically possible because the atom that arrives at the surface suddenly attaches to a kink of a surface step, thus conserving the surface free energy of the crystal. According to the same Schottky mechanism, an interstitial is created near the surface when a surface atoms moves inside the bulk [26]. Other defects called *induced defects* can arise in a crystal due to external factors such as heating, irradiation with particles, mechanical stress, etc. But a population of native point defects will always be present even inside the purest crystal, because they are in thermodynamic equilibrium with the crystal itself and cannot be eliminated. They are also called *intrinsic defects*. When dealing with thermal treatments on semiconductor materials, for damage recovery annealings or doping purpose, it is better to remember that the population of intrinsic point defects increases with temperature [27]. In addition to point defects, there are many complex structural defects inside a crystal, that can be schematized in a dimensional order:

A. Zero-dimensional defects: point defects

B. One-dimensional defects: dislocations (linear complexes of defects)

C. Two-dimensional defects: surfaces, grain boundaries

D. Three-dimensional defects: point defect clusters, voids, precipitates.

1.2.3 Impurity diffusion mediated by point-defects

The introduction of controlled amounts of impurity dopants into substitutional positions in a semiconductor lattice, process also called *doping*, changes the electrical properties of the material making it suitable for electronic applications. Controlling or anticipating how dopants will be incorporated inside the lattice is very difficult, because the diffusion mechanisms can be manifold, often mediated by point defects. In this paragraph, the most important diffusion mechanisms in germanium will be described.
The most simple impurity diffusion processes are independent on point defects and are called *direct diffusion mechanisms*.

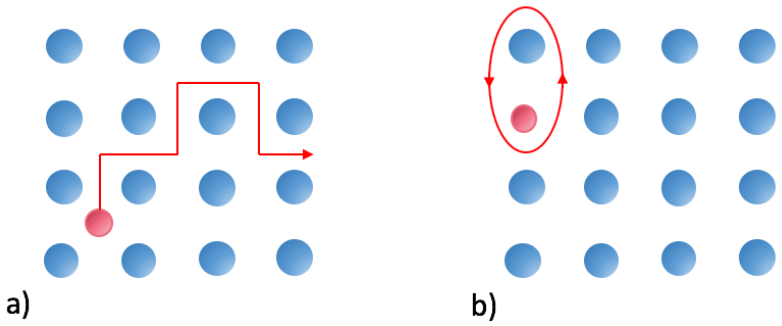

Figure 1.6. a) Direct interstitial mechanism exploited by an interstitial impurity to move across the lattice without coupling with a point defect. b) direct substitutional mechanism. A substitutional impurity moves from its lattice site to an adjacent one by exchanging its position with an atom of the Ge lattice. This process takes place rarely.

The most common, called *direct interstitial mechanism*, is typical of impurities that are smaller than Ge atoms such as Fe and H. These small atoms are dissolved mainly interstitially in the lattice and can diffuse from an interstitial site to another without requiring the presence of a point defect (see Fig. 1.6a). The other direct mechanism is called *direct substitutional mechanism*. It verifies when an impurity substitutionally dissolved into the lattice, i.e. that occupies a substitutional site, exchanges its position with an adjacent Ge atom (as shown in Fig. 1.6b). However, this process is very rare since for substitutional impurities it is more convenient to diffuse via point-defect mediated diffusion. The most common dopant elements for germanium, such as P, B, Ga, Sb and As, diffuse through processes mediated by intrinsic

point defects [28, 29]. Before describing them, let us define the following symbols for: V lattice vacancy, I self-interstitial, A_i interstitial impurity and A_s substitutional impurity.
The *Frank-Turnbull reaction* happens when an interstitial impurity reacts with a vacancy and occupies its substitutional site.

$$A_i + V \rightleftharpoons A_s \tag{1.11}$$

The reverse reaction is allowed and it is called *dissociative reaction*.
Cu is a typical diffuser that moves by this mechanism [28]. By dissociative reaction Cu produces vacancies. If there are many dislocations in the crystal, they trap vacancies and Cu atoms are enhanced in their diffusion. If there are no dislocations, vacancies can annihilate just at the surface, thus they accumulate and induce the reverse reaction with the result that Cu atoms slow down. The HPGe we use has got a high dislocation surface density (< 2000 counts/cm^2), as that used for commercial γ-ray detectors. According to Bracht in Ref. [28], in highly dislocated germanium, since vacancies are trapped by dislocations, Cu atoms diffuse through the Frank-Turnbull mechanism via the interstitial-controlled mode.
Cu_i + V $\leftrightarrow$ Cu_s
The effective diffusion coefficient for this mechanism is:

$$D_{Cu}^{eff} = (7.8 \times 10^{-4}) exp\left(-\frac{0.084eV}{k_B T}\right) cm^2 s^{-1}. \tag{1.12}$$

Eq. 1.13 reports the solubility of substitutional copper in Ge:

$$C_{Cu}^{eq} = (3.44 \times 10^{23}) exp\left(-\frac{1.56eV}{k_B T}\right) cm^{-3}. \tag{1.13}$$

The *kick-out reaction* takes place when a self-interstitial Ge atom displaces a substitutional impurity to an interstitial site.

$$I + A_s \rightleftharpoons A_i \tag{1.14}$$

The reverse reaction is allowed and is called *Watkins replacement mechanism*. In Ge, the only element that diffuses via this mechanism is boron [30, 31].
The *pair diffusion reactions* are two and occur when a vacancy or a self-interstitial forms a mobile pair with a substitutional impurity.

$$V + A_s \rightleftharpoons VA \tag{1.15}$$

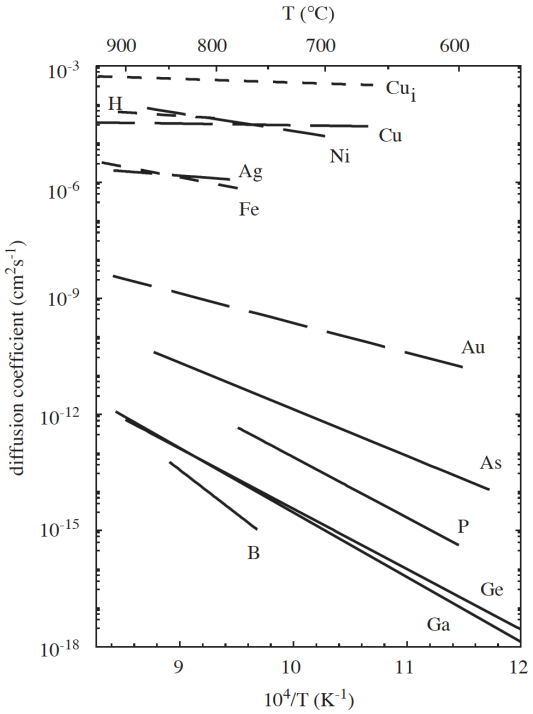

Figure 1.7. Solid lines represent diffusion data of elements that are mainly dissolved substitutionally and diffuse via the vacancy mechanism. Long-dashed lines illustrate diffusion data of elements, which are mainly dissolved on substitutional lattice site, but their diffusion, which is described on the basis of the dissociative mechanism, proceeds via a minor fraction in an interstitial configuration. The short-dashed lines indicate elements that diffuse via the direct interstitial mechanism. [28]

$$I + A_s \rightleftharpoons IA \tag{1.16}$$

The most frequent mechanisms are the last three, i.e. those where the impurity is substitutional and moves by means of a point defect.
In interstitial-mediated processes (Eq. (1.14) and (1.16)), the diffusion coefficient defined in Eq. (1.1) is proportional to the concentration of self-interstitials. While in the vacancy-mediated process (Eq. (1.15)) it is proportional to the concentration of vacancies [24]. Fig. 1.7 reports the temperature dependence of impurity diffusion coefficients in Ge, compared with self-diffusion. The various diffusion mechanisms are pointed out, particularly the difference between direct diffusion and point-defect mediated diffusion. Cu_i, Fe and H are dissolved interstitially in the lattice and move via the direct interstitial mechanism (short-dashed lines). Substitutional Cu, Ni, Ag and Au displace partially via interstitial-mediated diffusion (long-dashed lines). Instead classical dopant atoms like P, As, Sb [29] and Ga are dissolved substitutionally and move via the vacancy-mediated mechanism (continuous lines) [28]. Other details will be given in next paragraph.

1.2.4 Diffusion in germanium

An important concept when approaching to the doping of semiconductors is the *solubility* of dopants. The solubility of impurities in a solid phase is defined as the maximum (or saturation) concentration of that impurity, in thermodynamic equilibrium with the liquid phase of the matrix where it is dissolved. The solubility in the liquid phase is nearly always higher than in the solid one. It is influenced by the covalent (or ionic) radius of the solute [32]. Generally, as larger is the ionic radius, as lower is the solubility. In Ge, the maximum equilibrium solubility of dopants is relatively high for acceptors (i.e. p-type dopants), with value close to 5x10^{20} cm^{-3} for Al and Ga, except for B which has a maximum solubility around 1x10^{18} cm^{-3}. The equilibrium solubility of donors (n-type dopants) is in general lower than for acceptors, with P and As having values of $\sim$2x10^{20} cm^{-3} and $\sim$8x10^{20} cm^{-3}, respectively, and Sb having a significant lower value of 1.2x10^{19} cm^{-3} [33].
Vacancies mainly mediate the diffusion of both acceptors and donors in Ge under thermal equilibrium. This is due to lower formation energy of vacancies with respect to interstitials [34]. The B migration in Ge represents a special case since its diffusion process seems to be different, owing to a Ge self-interstitial mediated mechanism [31]. Donors in Ge are characterized by a quick diffusion, mediated by doubly negatively charged vacancies (V^{2-}). The mechanism is the following, being (A_s^+) a substitutional donor.

$$A_s^+ + V^{2-} \rightleftharpoons AV^- \tag{1.17}$$

Brotzmann, in Ref. [29], performed diffusion experiments of P, As, and Sb in Ge for intrinsic and extrinsic conditions, that is, the active dopant concentration is below and above the intrinsic carrier concentration. He found that, while for intrinsic conditions the profiles equal a complementary error function, under extrinsic conditions the profiles directly demonstrate an enhanced diffusion, with characteristic box-shaped profiles. According to this model, under extrinsic conditions, the diffusion coefficient of donors $D_A(n)$ is related to the intrinsic diffusion coefficient $D_A(n_{in})$ with the square of the equilibrium electron concentration (Eq. 1.18).

$$D_A(n) = D_A(n_{in}) \cdot \left(\frac{n}{n_{in}}\right)^2 \tag{1.18}$$

In the Brotzmann's work, the temperature dependance of the intrinsic carrier concentration (Eq. 1.19), and of P and Sb intrinsic diffusion coefficients (Eq. 1.20 and

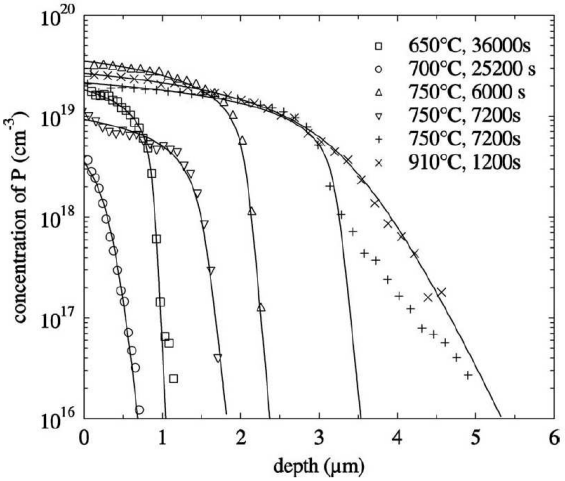

Figure 1.8. P diffusion profiles measured with SIMS after annealing at different temperatures and times [29].

1.21) are calculated:

$$n_{in} = 7.3^{+5.4}_{-3.1} \times 10^{20}\ exp\left(-\frac{(0.44 \pm 0.05)eV}{k_B T}\right) cm^{-3} \tag{1.19}$$

$$D_P(n_{in}) = 9.1^{+5.3}_{-3.4}\ exp\left(-\frac{(2.85 \pm 0.04)eV}{k_B T}\right) cm^2 s^{-1} \tag{1.20}$$

$$D_{Sb}(n_{in}) = 16.7^{+6.6}_{-4.7}\ exp\left(-\frac{(2.55 \pm 0.03)eV}{k_B T}\right) cm^2 s^{-1} \tag{1.21}$$

As an example, in Fig. 1.8 taken from Brotzmann work, concentration profiles of P measured with SIMS after diffusion annealing at different temperatures and times are reported. The profile at 700 °C has a maximum doping level below the intrinsic concentration n_{in}, while all other profiles above n_{in} at the respective temperature showing box-like shapes.

1.2.5 Out-of-equilibrium diffusion through laser annealing

Laser thermal annealing (LTA) is a doping technique studied for applications in the field of nano-electronics, with the purpose of reaching high doping levels over the solid solubility (i.e. above 1x10^{20} cm^{-3}). During a LTA process, laser irradiation causes the melting of a well defined region of the sample surface, which depends on the laser beam energy density, while the bulk remains almost not heated. Thus this method allows a precise spatial and temporal control. In the melted layer, dopant atoms are redistributed uniformly due to their huge diffusivity in the liquid phase

(10^{-5} cm^2/s) that is orders of magnitude higher than in the solid (10-12 cm^2/s). The rapid ($\sim$m/s) Liquid Phase Epitaxial Regrowth (LPER) results in the formation of high quality crystalline material with a high fraction of dopant incorporation [35]. This regrowth efficiently suppresses preexisting defects independently on the starting conditions. Essentially, high quality single-crystal materials can be produced even from deposited, amorphous or very damaged implanted layers. Thanks to this method, metastable Ge layers with carrier concentrations well above the solid solubility have been already demonstrated for antimony, starting from ion implanted layers [36,37].
Doped layers obtained by LTA show a partial electrical activation, however very high, whose causes are not fully understood. The most likely are residual defects, contaminants or clustering [38,39].

1.3 γ-ray detection

The study of the gamma radiations emitted by radioactive sources or after nuclear reactions is one of the best ways to investigate the structure of excited nuclear states. Gamma rays are emitted by an excited nucleus when it changes its energy state, while keeping constant its number of protons and neutrons. The energy carried by gamma rays is equal to the energy difference between the initial- and final- state of the nuclear transition. Therefore the main objective of gamma spectroscopy is to precisely measure the energy of the emitted radiation. Gamma rays are high-energy photons, i.e. they belong to the spectrum of electromagnetic radiation, with energy spanning from some KeV to 100 MeV. One of the most demanding requirement that gamma spectroscopy must meet is to provide detectors sensitive to such a wide energy range. To better understand the state of the art and the operating principle of gamma detectors, we first describe the mechanisms through which gamma photons interact with matter.

1.3.1 Photon interaction with matter

Unlike charged particles, which lose their energy continuously within matter through a sequence of numerous events, photons are absorbed or scattered in single events. The three major interaction mechanisms for gamma rays in matter, namely those that play an important role in radiation measurements are *photoelectric absorption*, *Compton scattering* and *pair production*. All these processes lead to a partial or complete transfer of energy from gamma photons to electrons of the medium and

this is at the basis of the detection mechanism.

Photoelectric absorption

In the photoelectric absorption process, the incident photon is completely absorbed by an atom of the medium. As a consequence an electron, which is called *photoelectron*, is ejected from one of the bound shells. A small portion of the energy released by the photon is used to break the bond between the photoelectron and the atom, while the rest is converted into photoelectron kinetic energy. Therefore the photoelectron carries off the majority of the original photon energy.
The photoelectric absorption can be accompanied by another radiative phenomenon called *fluorescence emission*. In fact the vacancy left in the bound shell is rapidly filled by a free electron from the medium, or by rearrangement of electrons from other shells. In both cases characteristic X-rays are emitted and reconverted into less energetic electrons through photoelectric absorption in less tightly bound shells. Sometimes, the migration of fluorescence radiation out of the active volume can affect the detector response because, even if small, a part of the incident gamma-ray energy has been lost. With less probability, the excitation energy released after the vacancy occupancy could be enough to ionize a further bound electron, which is called *Auger electron*.
Thus, the effect of the photoelectric absorption is the emission of a photoelectron that carries most of the gamma-ray energy together with one or more low-energy X-rays or Auger electrons corresponding to the absorption of the binding energy of the photoelectron. If the detector collects all of them, it is possible to reconstruct the original total energy of the incident gamma ray. By doing an experiment with monoenergetic gamma rays, one would obtain a simple delta energy distribution located at the energy of gamma-photons $h\nu$, as shown in Fig. 1.11 that reports an example of standard gamma spectrum. The photoelectric interaction occurs only in presence of atoms due to momentum conservation, but it is not the only way through which gamma rays interact with matter. Anyway it is the most probable for low-energy photons and high-Z materials.

Compton scattering

Compton scattering occurs with high probability for gamma rays of medium energy (from hundreds of keV to 7-8 MeV). The incident photon is scattered by a quasi-free electron belonging to the external shell of an atom, thus initially assumed

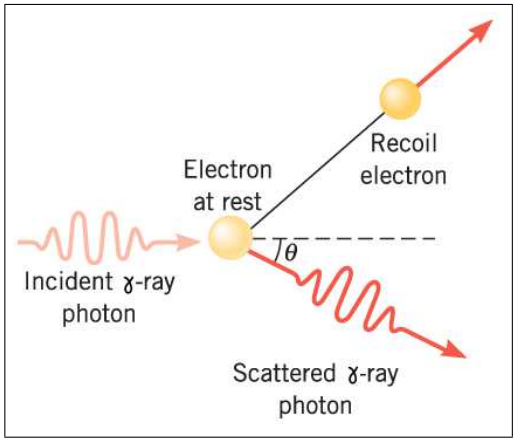

Figure 1.9. Compton effect. The incident photon is scattered by a free electron of the medium and is deflected through an angle θ. [40]

to be at rest. The photon is deflected through an angle θ with respect to its initial direction and part of its energy (*E-E'*) is transferred to the electron, which moves and is called *recoil electron* (Fig. 1.22). All scattering angles are possible, but the photon always keeps part of its original energy even in the limit case θ=π. This can be deduced also from equation (1.22) that is obtained by imposing simultaneously energy and momentum conservation. The equation represents a relation between the energy transfer and the scattering angle.

$$E' = \frac{E}{1 + \frac{E}{m_0 c^2}(1 - cos\theta)} \tag{1.22}$$

Gamma rays or photons can hit electrons with different scattering angles, thus transferring different energies. This implies a wide and continuous energy distribution for the scattered electrons, called *Compton continuum* (see Fig. 1.11), from which it is difficult to deduce the original energy of incident gamma rays. Moreover, because of the deflection given by Compton effect, the gamma ray might get out of the detector active medium leading to an energy loss. However, the effects of Compton scattering are not so disadvantageous.
In fact, modern detectors must allow not only to measure the energy of the incident γ but also to reconstruct the photon trajectory within the active volume. It is necessary to divide one of the contacts into isolated segments that will generate a linear electric field with the opposite contact. Each segment will collect only the charge generated in the active volume below itself. Once collected the different segment signals, Compton scattering formulas (together with pulse shape analysis) help in the chronological reconstruction of events, because they relate the energy deposited

at each event with the angle between the incoming and scattered photon. This new approach called *gamma-ray tracking* will be described in paragraph 1.3.5.

Pair production

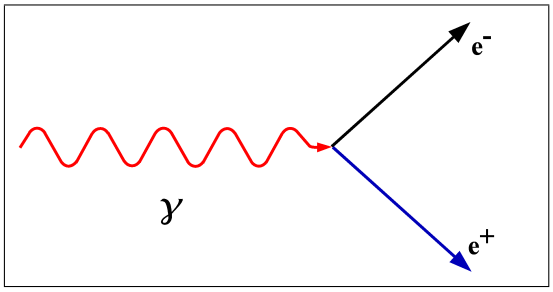

Figure 1.10. Pair production effect. A high energy incident photon, by exchanging its momentum with a nucleus, converts its energy in the generation of an electron-positron pair. The two particles are generated with opposite velocities.

In this third interaction process an incident gamma ray that enters the Coulomb field of an atom of the medium, totally converts its energy in the production of an electron-positron pair. The two particles are generated with opposite momenta, as it is shown in Fig. 1.10 and the presence of a massive nucleus is fundamental to ensure momentum conservation. This is a threshold process; in fact the photon must have at least twice the rest-mass energy of an electron, thus $2m_0c^2 = 1.022\ Mev$. In practice, the interaction probability via pair-production dominates for gamma rays with energy higher than several MeV. The energy excess $h\nu$ - $2m_0c^2$ is transferred to the pair in the form of kinetic energy [41]. While the generated electron can travel through the medium until it reaches the detector, the positron annihilates quickly, after slowing down, with another electron of the medium. This secondary interaction emits a pair of photons with energy of 0.511 MeV each. The annihilation photons may either escape or undergo further interaction within the detector, that if well collected contribute to the *full-energy peak*. If both annihilation photons escape only the electron and positron kinetic energies are deposited and the net effect is a *double escape peak* located at energy $h\nu$ - $2m_0c^2$. If only one annihilation photon escapes while the other is totally absorbed, these events contribute to the *single escape peak* located at energy $h\nu$ - m_0c^2 (Fig. 1.11).
Figure 1.12a reports the gamma ray absorption cross section for a standard detection material as function of photon energy. In the plot, all three main interaction phenomena are present: photoelectric effect, Compton scattering and pair production. The photoelectric interaction is dominating for low energy gamma rays ($<$ 500

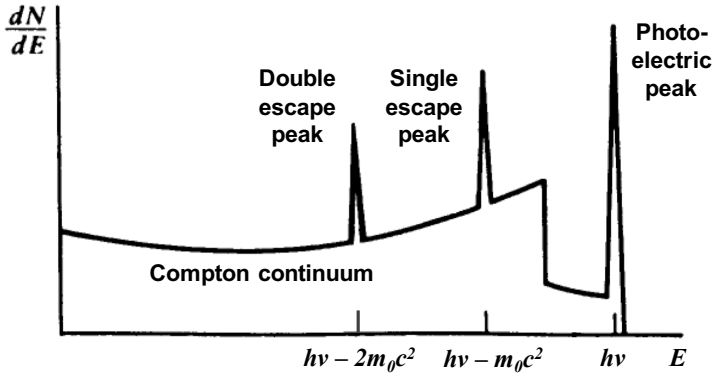

Figure 1.11. Gamma interaction spectrum. Apart for the Compton continuum, the photopeak due to photoelectric interactions and the pair-production peaks are shown.

keV). A discontinuity can be observed in the photoelectric absorption cross section: it represents a sudden increase in the interaction probability when gamma photons reach the binding energy of K-shell electrons, which then can be ejected. For gamma rays of energy higher than 500 keV the photoelectric cross section decreases exponentially, while that of Compton scattering becomes important. It dominates until 7 MeV of energy are reached, then pair production becomes the favoured interaction. Figure 1.12b instead shows the area where the interaction dominates in a plane defined by the atomic number of the absorber medium and the energy of incident gamma rays. The lines represent the value of Z and E_γ for which two effects have equal cross-section. The photoelectric effect dominates at low incident energies and in media with high atomic number. Compton effect is more probable for medium incident energies. Pair production is predominant for high energy gamma rays and high atomic number. Therefore, since gamma ray detection is done through photoelectric and pair production interactions, it is preferable to use an absorber medium with high atomic number. In the field of semiconductor detectors, both silicon and germanium could be easily employed. Anyway, germanium has got a higher atomic number (Z_{Ge} = 32 while Z_{Si} = 14) and more performing electrical properties. Indeed, its high electron and hole mobilities allow a fast collection of the charge generated by the passage of a gamma ray. Thanks to its small bandgap (0.6 eV) the energy needed for the creation of a hole-electron pair is low (2.96 eV) resulting in high energy-resolution. This last parameter is defined as the FWHM of the gaussian distribution of detected gamma rays, usually at 1332 keV. For Ge detectors the energy resolution is about *2 keV*, very low if compared with that of NaI scintillators (100 keV at the same incident energy) [41, 42].

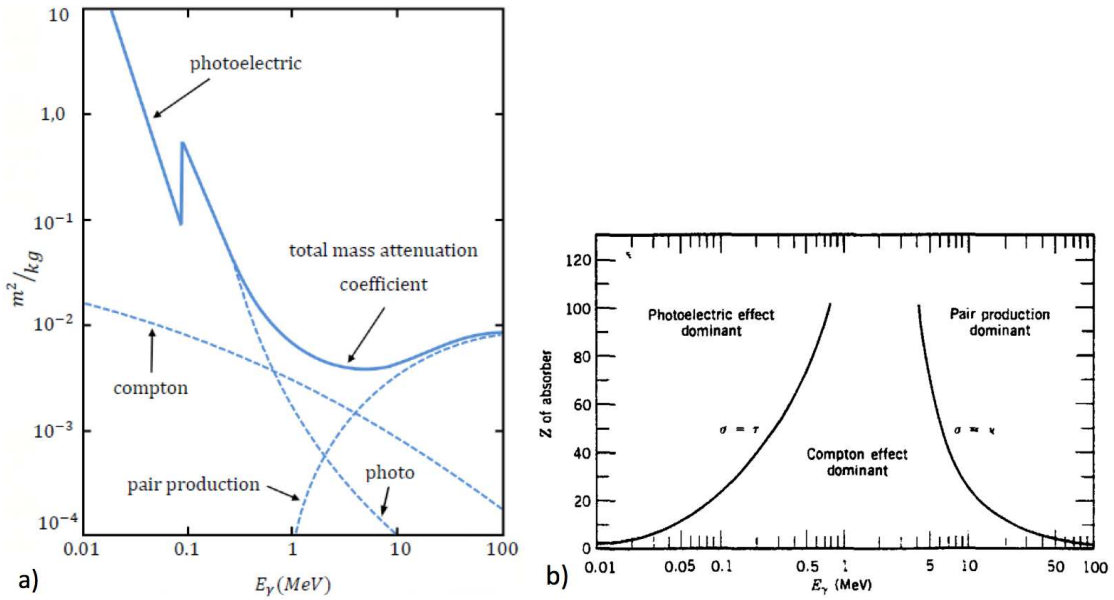

Figure 1.12. a) γ-ray absorption cross section for a standard detection material as function of photon energy. b) Relative importance of the three types of γ interaction. The lines represent the value of Z and E_γ for which two effects are equal. [41]

1.3.2 High purity germanium detectors: operation principle

As pointed out in the previous paragraph, germanium is to date the most performing semiconductor for gamma-ray spectroscopy in the wide energy range 50 keV - 10 MeV. For the purpose, standard microelectronic-grade Ge cannot be used, because the number of electron-hole pairs produced by the passage of a γ photon would be very much lower, about 3.5x10^5 at 1 MeV, than that of free charge carriers due to impurity ionization [43]. It is necessary to use high purity germanium (HPGe), available from the late 1970s and characterized by a net impurity concentration of 5x10^9 to 2x10^{10} cm^{-3}. At room temperature, mobilities of charge carriers are the same as for other doping levels, i.e. 3900 cm^2/Vs for electrons and 1900 cm^2/Vs for holes. Such a pure material can be grown through two different steps. The first is the zone refining procedure, through which a partial melting of Ge is done to attract impurities, exploiting their higher diffusivity and solubility in liquids. In this way impurities will tend to move with the molten zone and be concentrated at one side of the ingot after the process is completed, giving a material with a net electrically active impurity concentration of $\sim 10^{12}$ cm^{-3}. Then, the standard Czochralski single-crystal growth method is applied in hydrogen atmosphere (which can passivate some defects) and a net impurity concentration between 10^9 and 10^{10} cm^{-3} is obtained [44].

In order to detect gamma photons, the small bandgap of Ge is at the same time a positive and negative property. It is really useful to increase the detector resolution, because for each incident photon many electron-hole pairs are generated and in this way it possible to discriminate between very small differences in energy of different photons. However, a small bandgap also favours the thermal excitation of electrons across the forbidden zone. This means that at room temperature there is a thermal carrier concentration of about 2x10^{13} cm^{-3}. To suppress thermal carriers, germanium must be cooled under 200 K and to do this it is put inside a vacuum cryostat containing liquid nitrogen. Even at this concentration free charge carriers would cover those generated by the photon. The solution is to create a p^{+}-n or p-n^{+} junction in HPGe germanium (depending on the bulk type) in order to obtain a depletion region where impurities are completely ionized and free charge carriers removed. This would be the active medium for gamma ray detection. The depletion region can be extended to the whole germanium volume (except for the p+ or n+ layer) by reversely biasing the junction, thanks, once again, to the very low background doping of the bulk material. The thickness *d* of the depletion region for planar detector geometry depends on the applied reverse bias, as shown in Eq. (1.23):

$$d \cong \sqrt{\frac{2\varepsilon_r \varepsilon_0 V}{eN}} \tag{1.23}$$

where ε_r is the relative dielectric constant (ε_{Ge}=16.2), V is the applied potential and N is the doping concentration of the junction side under consideration. For instance, once a typical 2000 V is applied, with N = 10^{10} cm^{-3}, a huge 19 mm thick depletion layer can be obtained.

By considering a planar detector of cylindrical shape, for simplicity, and assuming a constant doping concentration throughout the volume, let's describe how the junction behaves when we apply a growing potential. At low reverse bias, the detector is only partially depleted, being ω the thickness of the depletion region, as shown in Fig. 1.13 a. This configuration is non-optimal because the undepleted zone is a dead layer for photon detection. In fact, charge pairs that are created in the undepleted zone after photon interaction with Ge, would immediately annihilate without generating any electric signal, since there is no electric field to separate them.

The electric field generated inside the detector has a linear behaviour with respect to the distance *x* from the top electrode (Eq. (1.24)).

$$E = \sqrt{\frac{2eN}{\varepsilon}} V \left(1 - \frac{x}{\omega}\right) \tag{1.24}$$

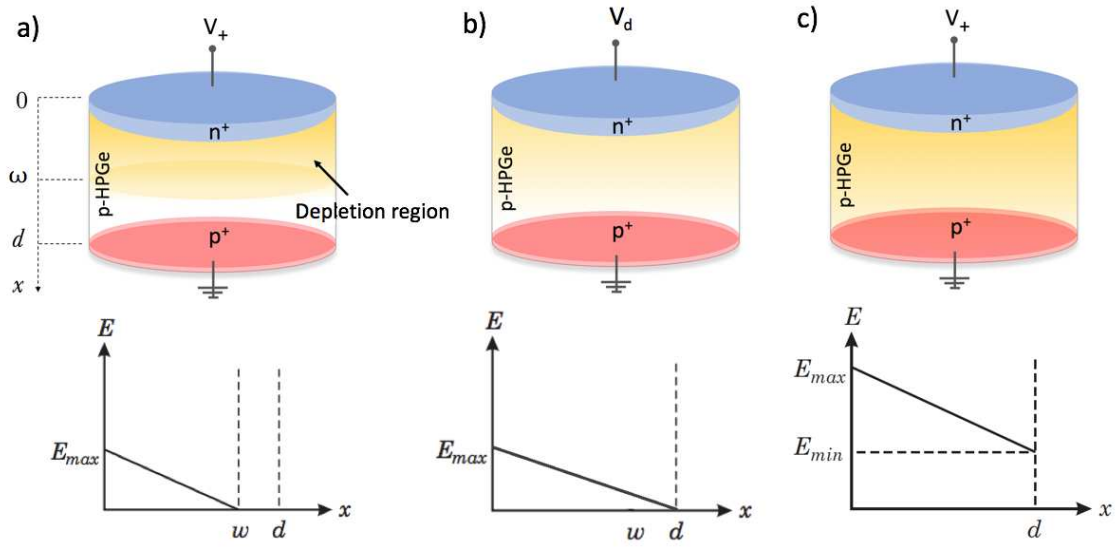

Figure 1.13. Schematics of a planar detector under different bias conditions. The depletion region is highlighted in yellow. For each case, the linear electric field is plotted as function of the depth. a) Low bias and partial depletion. b) When the value V_d is reached, the detector is totally depleted. c) Overbias and overdepletion condition.

When the applied voltage is increased up to V_d, total depletion is achieved and ω=*d* (Fig. 1.13 b). Increasing the bias voltage beyond this point (*overbias*, often called *overdepletion*) increases the field uniformly according to Eq. (1.25).

$$E = \frac{2V_d}{d}\left(1 - \frac{x}{d}\right) + \frac{V - V_d}{d} \tag{1.25}$$

At the bottom electrode the field is no longer null but it assumes the value E_{min}=$\frac{V-V_d}{d}$, see Fig. 1.13 c. Normally, sufficient overvoltage is applied so that the electric field is high enough to impart saturated drift velocities to charge carriers, minimizing the collection time and possible recombination and trapping effects. For instance, in germanium at the normal operating temperature of 77 °K, saturated electron velocities are reached at a minimum field of about 10^5 V/m. Anyway, one should not think that the electric signal related to an event starts after that charges have travelled through the detector and reached the electrodes. If this was true there would be a delay between the γ passage and the electrical signal and the detector would have bad timing properties. Instead, when carriers start their motion along the electric field lines, an image charge is generated at the electrode and the output pulse begins to form immediately [45].

1.3.3 HPGe detector contacts

The formation of the p^+-n or p-n^+ junction is achieved by starting respectively from a n- or p- type HPGe and then creating a highly doped surface layer. The p^+ contact is usually done through ion implantation of boron atoms at an energy of 50-100 keV and to a dose of 10^{14}-10^{15} cm^{-2}, thus obtaining a thickness of about 300 nm. The implanted layer need to be annealed at 250 °C for 1 hour to achieve electrical activation. The n^+ contact is usually done through lithium diffusion at 300 °C for 10-30 minutes. Due to its high diffusivity at low temperature, Li forms a contact several hundred of microns thick and unfortunately this is a thick dead layer for γ detection, since the field does not enter this highly doped (10^{19} cm^{-3}) region. However, not only a rectifying contact is needed to collect the γ signal, but also a secondary contact at the other end of the detector that should be ohmic for majority carriers and *non-injecting* or *blocking* towards minority carriers. When the applied electric field separates charges derived from a γ ray interaction, they are then collected by contacts. But if the secondary contact is not blocking, it injects carriers to replace those collected, in order to conserve the charge concentration. In this way, an additional bulk leakage current is generated. For bulk HPGe of p-type, the Li layer acts as the rectifying contact that forms the semiconductor junction, while the B layer acts as the ohmic/non-injecting contact (see Fig. 1.14). Vice versa if the bulk HPGe is of n-type. These standard doping techniques currently employed present some

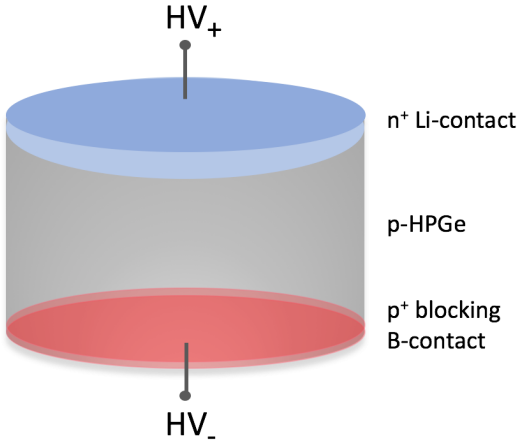

Figure 1.14. Schematic of a p-type planar detector. The Li-doped layer acts as the junction contact, while the B-doped layer acts as the ohmic/non-injecting contact.

technical and economic disadvantages. Li deposition and diffusion is an obsolete doping technique that leads to the formation of a dead layer at least 500 μm thick. Nowadays semiconductor science is proposing several doping techniques for the

formation of shallow junctions such as spin-on-doping, monolayer doping, laser thermal annealing and others. Of all these, one technique that satisfies all the requirements needed for the formation of an optimal n-type contact should be chosen and tested. Two important requirements are that the doped layer should be segmentable and resistant to the radiation-damage recovery annealings. With current technology (Li diffusion) it is not possible to do a fine segmentation, because Li diffuses in Ge even at room temperature and could modify the segment properties. The same problem occurs when the detector is heated for the recovery of radiation damages. Even if the annealing is done only at 100 °C (for $\sim$ 10 hours) Li diffuses thus damaging the contact.
As regarding the formation of the p contact, boron ion implantation is an expensive technique and it is not within reach of all research laboratories. With a view to allow research labs to build homemade HPGe detectors, it could be advantageous to find an alternative method. Besides, ion implantation is hard to be performed on geometrically complex surfaces.

1.3.4 Surface passivation

The electrical and chemical passivation of intrinsic surfaces of gamma detectors is a crucial topic. By looking at the planar detector scheme in Fig. 1.14, one can notice that there is a huge intrinsic surface all around the lateral surface of the cylinder. The surface is the most critical element of single crystals. There, the crystal lattice is abruptly interrupted leaving free dangling bonds and lattice defects. The first can react with atmosphere forming bonds with impurities or even molecules present in the external environment. While lattice defects such as vacancies or dislocations can provide empty electronic states. If these states are charged, the surface becomes conductive and produces a background current between the two contacts that can disturb or destroy signal collection. These properties make intrinsic surface a certain source of leakage current. When testing the I/V characteristic of an HPGe diode that one wants to use as a detector, the contribution of surface leakage current is seen as a constant increase of reverse current as the reverse voltage is increased. Therefore, the presence of surface leakage current would cover any signal due to the passage of a gamma photon. One way to passivate the surface of semiconductor materials could be to cover them with oxides. However, in case of germanium, its oxides GeO and GeO_2 are not stable for long-term operation because they are water-soluble and decompose by heating. Industries generally use to cover intrinsic surfaces with a sputtered layer of SiO_2 or amorphous Ge, due to their high stabil-

ity. Unfortunately, it has been observed that these dielectric layers influence the detector electric field near the surface, modifying it until causing the formation of a dead layer several millimetres thick [43]. Some new passivation routes have been proposed such as hydride, chloride and sulphide termination, within researches for microelectronic devices [46, 47]. But in the work by Maggioni et al. [48], three passivation treatments have been studied precisely in view of the development of a gamma-ray HPGe detector. Therefore, the electrical properties of the obtained surface Ge termination have been evaluated from time to time, together with the measurement of leakage current, depletion voltage, dead layer, detector efficiency and detector resolution. Tested treatments were: methanol passivation, low- and high- hydride termination and sulphide termination. All of them showed a thinner dead layer than commercial devices, less than 1 mm thick for hydride and methanol terminations while thicker for S-termination (see Fig. 1.15). In this case the thick dead layer also implies an inactive volume of about 10%. This result is mirrored by the measurement of the depletion voltage: S-termination is characterized by the highest value ($\sim$ 2000 V) because the dead layer distorts the electric field. As regarding detector efficiency and resolution, values are comparable for all the treatments. Maybe the most important measurement is that of leakage current across the passivated surface. All treatments showed a very low value ($\leq$ 4 pA) but methanol termination provided the lowest one ($\leq$ 2 pA). For this reason, in this thesis the methanol-terminated passivation treatment is used.

1.3.5 Detector configurations: from single shapes to detector arrays

First HPGe diodes were created in a simple cylindrical shape, called *planar* (Fig. 1.14), by cutting slices from grown ingots. Then, B and Li contacts were done at the two end surfaces of the cylinder. Planar diodes have got a diameter of few centimetres and are only 1-2 cm thick since, even by applying high voltage, that is the maximum depletion thickness that can be obtained. This kind of detector has got a small active volume, anyway it is characterized by a uniform distribution of the electric field and can be efficiently used to collect gamma spectra in the low energy range, from 10 keV to few hundred keV. In order to increase the active volume available for the detection of high energy gamma photons, a different detector shape was designed, called *coaxial*. It is a cylinder with an inner cylindrical hole along its axis. The two contacts are done on the outer and inner surface of the cylinder, that can have a diameter of 6-8 centimetres and can be 7-11 cm long. In this way, the thickness to deplete is small because it corresponds to the distance between the two con-

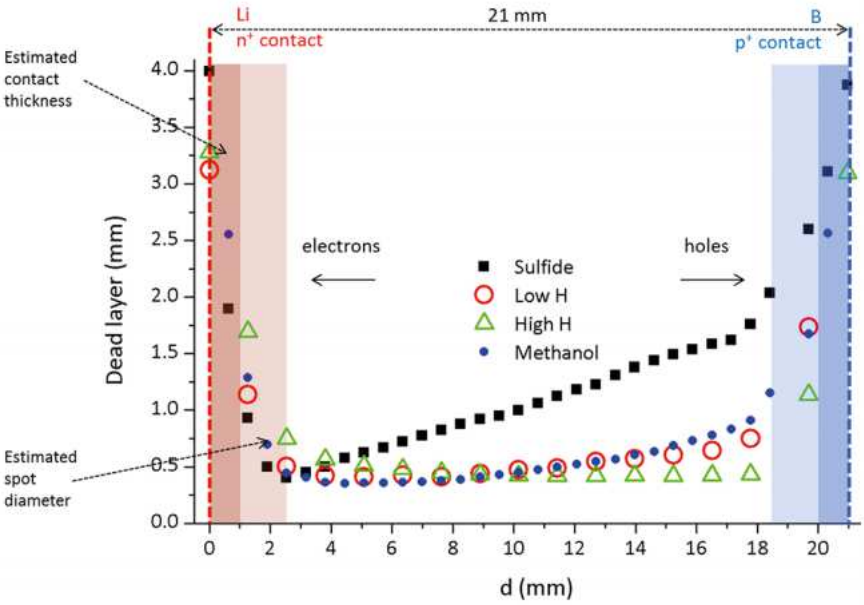

Figure 1.15. Thickness of the dead layer formed under the surface after different passivation treatments, as function of lateral position, in a coaxial detector [48].

tacts, while the active volume is really big. With this kind of detector it is possible to collect spectra of high-energy gamma photons until 10 MeV. A true coaxial diode would have a uniform radial electric field. However, as it was said in the previous

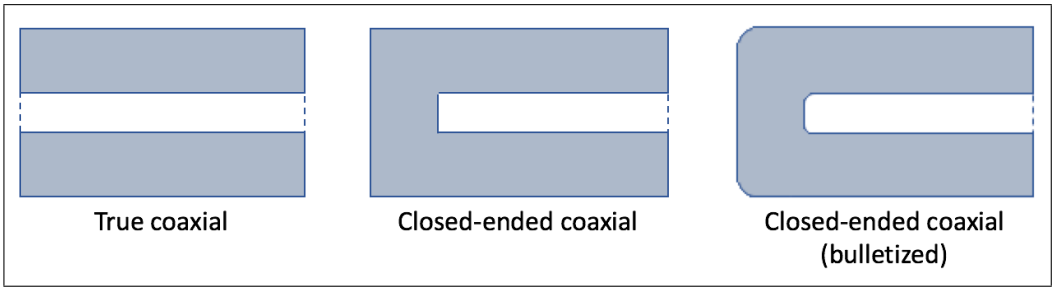

Figure 1.16. Three common shapes of coaxial detectors.

paragraph, under the intrinsic surface (that is found at the two ends of the cylinder) there is a dead layer few mm thick. Since gamma photons enter there, some of their energy could be lost. Moreover, it is very difficult to electrically isolate the intrinsic surface when high voltage is applied between contacts and if passivation is not complete, some leakage current could be seen. For all these reasons, commercial available coaxial diodes have got a closed end, that is the inner cavity doesn't reach the other end of the cylinder. The outer contact is done also on the closed end sur-

face, in order to avoid the formation of a dead layer. In this detector configuration photons enter from the closed end. Due to not symmetrical contacts, the electric field generated inside the detector is not uniform. In particular, there is a region of reduced field strength near the corners of the crystal where carrier velocities can be lower than normal. Some manufacturers round the corners of the closed end and of the cavity to help eliminate the low-field regions (see Fig. 1.16). This procedure is called *bulletizing*.
Nowadays, a typical experiment of gamma spectroscopy is carried out through a complex detector array, that is a set of HPGe detectors arranged to form a sphere, in order to cover the whole solid angle. In reality, as anti-Compton shields and cryogenic capsules are needed, just a part of the solid angle is covered. These big detector arrays are located along the beam of an accelerating facility and positioned where a nuclear event with gamma decay occurs. In this way, all γ rays emitted can be detected. The first 4π detector arrays, built during the late '80s and '90s,

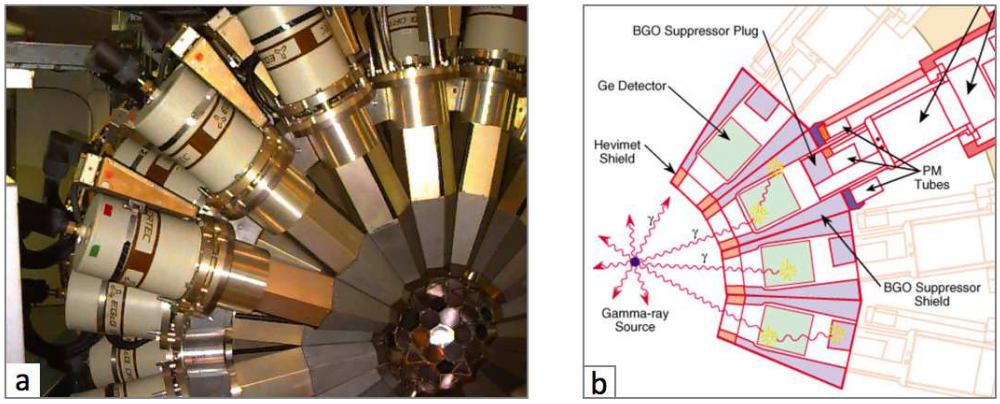

Figure 1.17. a) Picture of part of the GAMMASPHERE detector array [49]. b) Schematic of the detectors composing GAMMASPHERE: single HPGe diodes surrounded by the anti-Compton shield in BGO [50].

were GAMMASPHERE (for the US collaboration) and EUROBALL (for the European collaboration). GAMMASPHERE had 110 hexagonal detectors, each of which was made up of an n-type HPGe cylindrical diode surrounded by a hexagonal BGO anti-Compton shield (see Fig. 1.17a and 1.17b). Anti-Compton shields are blocks of a high-Z material, called BGO, which surround HPGe diodes. Their function is to detect and suppress the events caused by photons that interact via Compton effect in Ge and then scatter out of the active detector volume. If this type of events were not suppressed, only part of the photon energy would be measured by the HPGe detector, contributing to the Compton continuous distribution. The Compton continua of all γ rays would sum and make it difficult to detect a weak full-energy peak

on the Compton background.In GAMMASPHERE 95% of 4π are covered with detector modules and the Ge detectors cover 46% of 4π. EUROBALL was completed later, in the late 90s, and its design followed a different route. It is composed of very large composite detectors called *cluster* detectors. Each of them is made up of seven n-type HPGe coaxial diodes grouped in a single cryostat and surrounded by a single anti-Compton shield (see the schematic shown in Fig. 1.18). The cluster detector has an excellent efficiency at high energy due to the adding back of Compton-scattered events. GAMMASPHERE and EUROBALL have similar efficiency and resolving power, but due to their different design they have different peculiarities and are complementary. They led to a formidable gain in the knowledge of the nuclear structure, but in order to increase the limit of observation a new approach was required: gamma ray tracking arrays were the following step. The new concept in

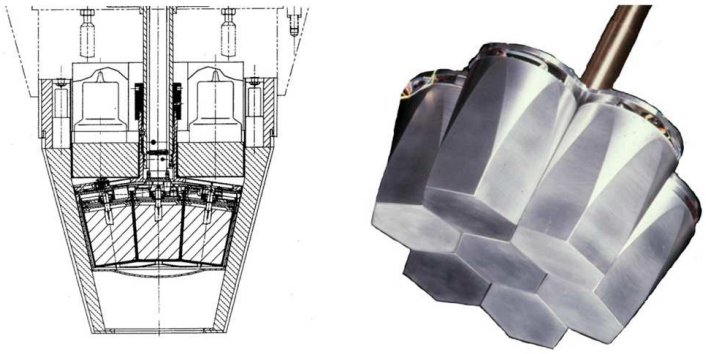

Figure 1.18. Schematic and picture of one cluster module composing the EUROBALL detector array. Seven HPGe coaxial diodes are grouped together and surrounded by a single anti-Compton shield [43].

array design is based on γ-ray tracking in highly segmented HPGe detectors. The idea is to surround the target by a 4π shell of 100-200 position-sensitive Ge detectors. Using digital electronics and pulse-shape analysis techniques it is possible to identify the energy, time and position of every interaction point of a γ-ray as it interacts, scatters and is finally absorbed in the 4πball. A high segmented HPGe detector is a diode where the outer contact should be separated into multiple small contacts called *segments*, well electrically isolated from each other. In this way, by collecting signals coming from each segment of the active volume, one can trace the photon trajectory. Both collaborations, the European and US one, have designed a tracking detector array. They are respectively called AGATA (Fig. 1.19) and GRETA (Fig. 1.20). At the moment, AGATA has been built to cover almost 1π of the solid angle, by mounting 32 encapsulated segmented detectors. Once completed the 4π, it will have 180 encapsulated detectors. Each one contains a single HPGe crystal elec-

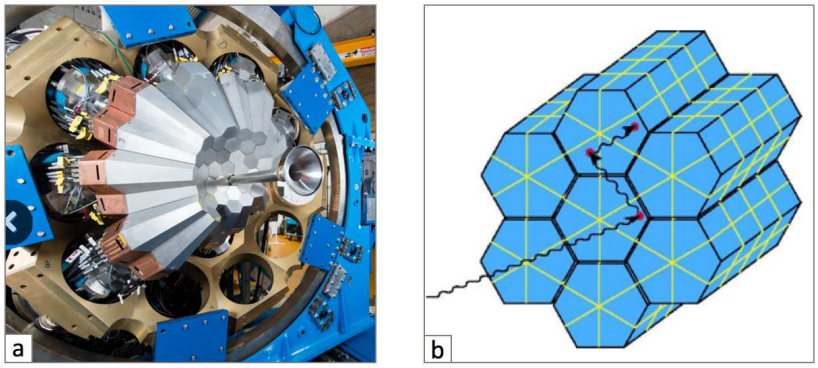

Figure 1.19. a) AGATA with 32 HPGe crystals at GANIL facility, September 2016 [51]. b) Schematic that describes how anti-Compton shields are not required when ray-tracking is feasible.

trically segmented into 36 segments. The US collaboration has designed the array

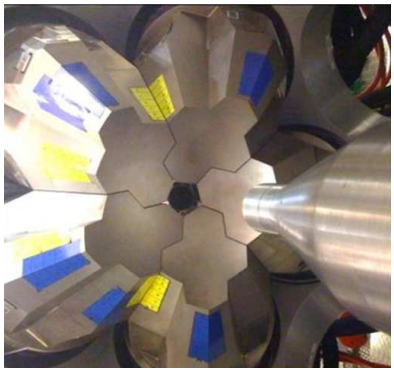

Figure 1.20. Gretina in 2011 with three quadruple clusters [52].

GRETA. Once completed, GRETA will be composed of 120 highly-segmented HPGe coaxial crystals grouped in modules of 4. Until now the small GRETINA array has been built with 28 segmented crystals (Fig. 1.20).
Monte Carlo simulations of γ-ray tracking using the measured values of position resolution have been carried out over a broad energy range and these predict that a 4π array of 100-200 detectors will have a sensitivity improved by several orders of magnitude compared with EUROBALL and GAMMASPHERE [43].

Chapter 2

Characterization techniques

When dealing with the study or processing of materials, being able to apply some characterization techniques is crucial. In many cases, a characterization analysis is the only way to understand if the performed treatment has been successful. When semiconductor doping processes are carried out, there are no visible modifications of the material at the macroscopic level. So, you don't know anything about the result: if dopant atoms entered, if they are electrically activated, if the semiconductor has remained crystalline, what kind of defects has formed and so on. Unfortunately, the only visible macroscopic effect could be an undesired damaging of surfaces. First, it is important to check the state of the semiconductor surface, especially when using doping processes that involve thermal annealings. Particularly, in case of germanium, its surface is so reactive that it is not rare to observe the formation of damages such as cracks, pin-holes or cleaning signs. This kind of features can be identified with the use of optical imaging, if their size is of the order of hundreds of microns, or otherwise with Scanning Electron Microscopy (SEM) or Atomic Force Microscopy (AFM) imaging. Next, through Secondary Ion Mass Spectrometry (SIMS), one can understand if dopant atoms have entered the material, and at which concentration. This characterization technique allows to trace the profile of atom concentration as function of the depth. If the aim of the process is obtaining a density of free charge carriers or any modifications in the semiconductor energy bands, it is fundamental to measure the electrical activation of dopant atoms. The electrical characterization can be done through four-point probe electrical measurements, by using the Van der Pauw method and exploiting the Hall effect. Rutherford Backscattering Spectrometry (RBS) is a versatile technique, sensitive to the lattice structure particularly when performed in channeling mode. Information on the first tens of nanometers can be obtained, for instance regarding the presence of lattice defects near the surface such as clusters, dislocations or contaminants. Moreover, it can de-

tect the concentration of a particular element also in multi-element systems.
In this chapter, all of the above-mentioned characterization techniques will be described, with particular focus on four-point probe electrical measurements that were for the first time directly performed by the research group during my PhD thesis. In particular, the setup of the measurement apparatus, in collaboration with technical personnel, was one of the topics of my activity.

2.1 Imaging techniques

2.1.1 Scanning Electron Microscopy (SEM)

The SEM is one of the most versatile instruments available for the examination and analysis of the microstructural characteristics of surfaces. The primary reason for the SEM's usefulness is the high resolution that can be obtained when bulk objects are examined; advanced research machines are available that have achieved resolutions equal or below 1 nm, our instrument has got a reliable resolution of 100 nm. The area to be characterized is irradiated with a finely focused electron beam, which may be static or swept in a raster across the surface of the specimen, causing the emission of secondary electrons, backscattered electrons, Auger electrons and photons of various energies. The signal of greatest interest are the secondary and backscattered electrons, since they vary according to differences in surface topography. In fact, an important feature of the SEM is the three-dimensional appearance of the specimen image, direct result of the large depth of field, as well as to the shadow-relief effect of the secondary and backscattered electron contrast. The sample is kept under high vacuum (10^{-5} Torr), as the air would prevent the beam emission since secondary electron have low energy. Besides, the sample must be conductive (or metallized), otherwise it could produce electrostatic discharge that would disturb the detection of secondary electrons (germanium, specially at high purity, has a low enough resistivity to avoid this problems). The electron column consists of an electron gun and two or more electron lenses. The electron gun produces a source of electrons and accelerates them to an energy in the range 1-30 keV (in our instrument). At this stage the beam diameter is too large to generate a sharp image at high magnification. Thus electron lenses are used to reduce the diameter and place a small, focused electron beam on the specimen, as shown schematically in Fig. 2.1a. So the electron beam emerges from the final lens into the specimen chamber, where it interacts with the near-surface region of the specimen to a depth of approximately 1μm and generates signals used to form an image. The actual formation of an image requires a scan-

ning system to construct the image point by point. The electron detector consists of a scintillator, a light pipe and a photomultiplier tube and it is located to the side of the specimen. It is electrically isolated from the rest of the microscope and it is kept at a positive voltage of about +300 V, in order to attract the secondary electrons from anywhere in the specimen chamber [54]. As regards the microanalysis, Energy

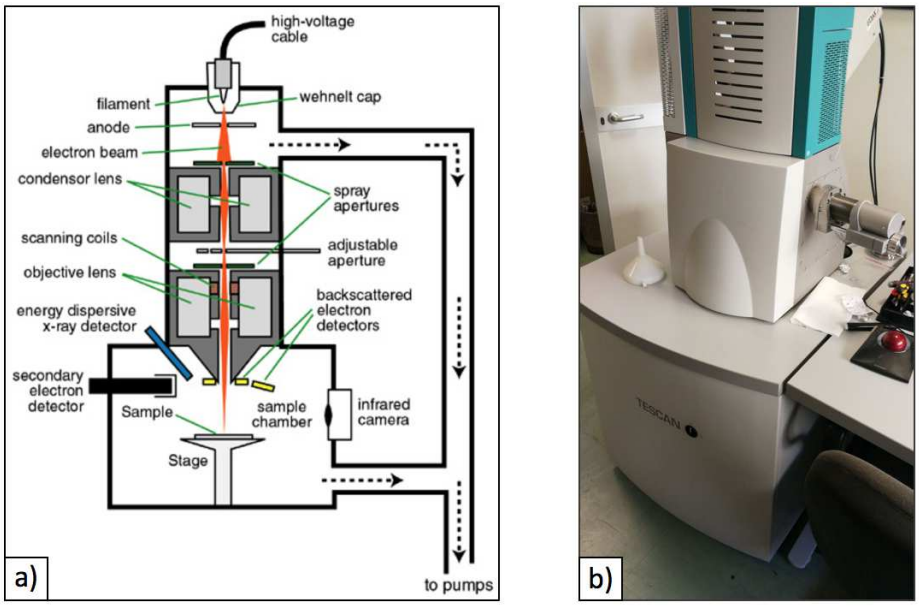

Figure 2.1. a) Schematic draw of the electron column, the system of lenses and the electron detector [53]. b) Tescan Vega3 XM apparatus located at INFN-LNL.

Dispersive X-ray spectrometry (EDX), the instrument exploits the X-rays emitted by sample upon the incidence of the accelerated electron beam [55]. These are detected by a special detector called Energy Dispersive Spectrometer (EDS). Its working principle is based on the interaction between X-rays and an appropriate material. Our apparatus has got a high purity germanium crystal. It is kept under high vacuum conditions and at a temperature of -192 °C with the help of liquid nitrogen. After the interaction between photons and crystal an electric current is generated and amplified. The resulting image consists of an X-rays spectrum, from which it is possible to obtain the chemical composition of the analyzed material, since every peak of the spectrum corresponds to a precise atomic species. The SEM microscope used in this work (by Tescan) was located at the INFN National Laboratories of Legnaro (LNL) and it is shown in Fig. 2.1b.

2.1.2 Atomic Force Microscopy (AFM)

The AFM (Atomic Force Microscopy) belongs to the group of SPM microscopes (Scanning Probe Microscopy), which study the surface morphology of a sample and possibly other properties (like capacity, electronic properties, ferroelectric domains, etc.), by using a probe. The AFM consists of many components. The most important is the tip because it is the part that interacts with the sample. It is usually made of silicon and it can be characterized by a conical or pyramidal shape. It is $10 \div 15$ μm long, while its radius of curvature, which is the most important parameter because it is related to the resolution, is about $3 \div 30$ nm (in our instrument the tip radius is $<$10 nm for a resolution of 0.6 nm). The tip is at one end of the cantilever, which is a rectangular piece of silicon with length about 150 μm and thickness about 5 μm, whose main property is the elasticity. In fact, the elastic constant of the cantilever determines the possibility to measure the interaction between the tip and the surface. The tip is attracted or repulsed by the sample surface, because of mechanical contact forces and Van Der Waals forces that arise between the atom of the surface and those of the tip. The Van Der Waals forces are short-range intermolecular forces and they include: electrostatic interactions between dipoles, polarization forces and repulsive forces due to the Pauli exclusion principle. The tip is attracted at long distances and repulsed at very short distances (because of the Pauli exclusion principle). These interactions deflect the cantilever. Another important component is a piezotube, that is a piezoelectric material which accumulates electric charge in response to mechanical stress and deformation. In some AFMs the piezo tube supports the sample and moves it nearer or farther the tip (as in the scheme 2.2a), otherwise it could be connected to the cantilever and move it up or down (as in our system). The operating principle is the following: a laser diode sends its beam to the cantilever and, after reflecting on it, the beam arrives to a photodiode. Depending on how the cantilever is deflected, the beam will hit different points of the photodiode surface, which is divided into four quadrants. Thus the photodiode can provide a current signal proportional to the cantilever deflexion, which enters a feedback system. This system executes different operations depending on the working mode. In *contact mode*, which is the most commonly used in case of quite flat surfaces, the tip-sample force is kept constant so, once measured the cantilever flexion, the feedback system acts by stretching or shortening the piezo tube. This measurement mode is one of the fastest and allows to obtain the highest resolution. However it is risky, because in case of a very irregular surface the feedback system could not have time to change the tip-sample distance, causing a damage of the sample surface but also of the tip

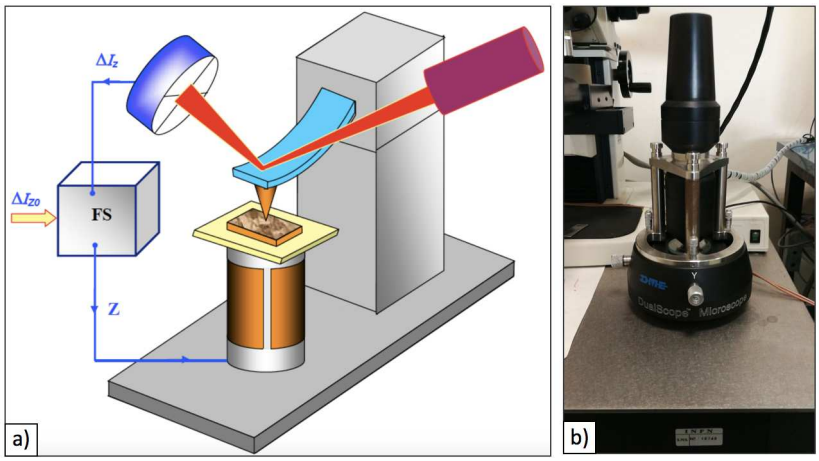

Figure 2.2. a) Schematic representing the operation of an AFM. The movements of the cantilever are transformed into a current through a laser and a photodiode. This current enters a feedback system that drives a piezotube. b) DME DualScope AFM apparatus, located at INFN-LNL.

itself. Between the non-contact modes, the most commonly used is the *oscillating mode*, in which the cantilever oscillates periodically up and down and variations of the interaction force with the surface act modifying the oscillation amplitude. The main advantage that comes from this type of measurement is due to the high signal-to-noise ratio for modulated signals, which allows to work when the forces between tip and surface are very weak. In this work we used a DME DualScope AFM microscope in non-contact mode (Fig. 2.2b), located at the INFN National Laboratories of Legnaro (LNL).

2.2 Secondary Ion Mass Spectrometry (SIMS)

Secondary Ion Mass Spectrometry (SIMS) is a technique that measures the chemical concentration profile of impurities in the surface region of a solid matrix, with sensitivity in the part per billion (ppb) to part per million (ppm) range. The technique is destructive, since it uses a primary beam of ions to sputter the sample surface. Between the atoms emitted from the sample surface, just the 2% are charged secondary ions that can be accelerated and sent to a mass spectrometer. This selects the ions of interest and then a detector count them. One-dimensional concentration profiles function of depth can be obtained by counting the selected secondary ions. The secondary ion yield as function of time can be converted into a concentration depth profile by a proper calibration procedure. The depth scale is obtained by measuring the final crater depth with a profilometer. While the calibration between the

yield and impurity concentration is done by quantitative comparison to standards characterized by the same matrix as the sample and known impurity concentration, measured of course with the same conditions. The instrument used for this work is a *Cameca IMS 4f* located at the Physics and Astronomy Department of the University of Padova. A schematic of this complex machine is shown in Fig. 2.3. This

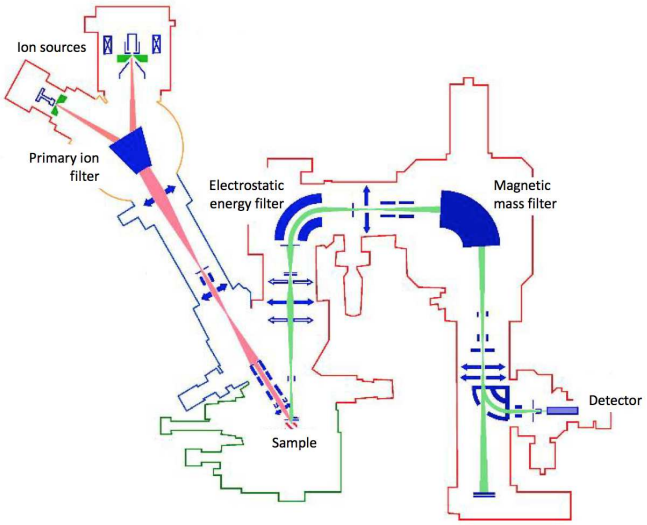

Figure 2.3. Schematic representing the Cameca IMS 4f secondary ion mass spectrometer used for this work.

instrument has two primary ion sources available, one of O_2^+ ions and one of $^{133}Cs^+$ ions. The choice of the source is based on the sample to be measured and it is done looking for yield maximization while avoiding undesired matrix effects. Primary ions are accelerated by a high voltage and focused through a complex system of lenses until a beam spot of some tens of microns and controlled energy is obtained. The beam impacts on the sample surface and erodes it with a continuous and homogeneous motion, thus in rastering mode. The emitted secondary ions are then accelerated and filtered by an electrostatic sector analyser (ESA), which selects only ions with a well defined kinetic energy. The selected beam is again accelerated and focused before entering the magnetic sector analyser (MSA), which selects the mass of interest. Finally these ions are sent to the detectors, a photomultiplier or a Faraday cup.

This technique is not suitable to strictly characterize the surface. In fact, the SIMS signal in the first few nanometers (first 10 or 20 nm) is typically affected by artifacts due to the native oxide, or due to surface transient effects related with the establishment of a steady state between the primary beam ions incorporation and removal. Nevertheless, for deeper thicknesses the technique is very refined and generally the

impurity concentration profile is characterized by an uncertainty less than the 10%.

2.3 Rutherford Backscattering Spectrometry (RBS)

The Rutherford Backscattering Spectrometry is a technique of long history and today it is of fundamental use in the study of materials. It is complementary to the SIMS because it allows to accurately characterize the surface, but it has also a good resolution in depth. Moreover it allows in principle to analyse solid components made of different elements without non-linear effects that often affect SIMS in these cases (matrix effects).
It consists in sending a beam of high-energy alpha particles against the sample surface; then, from the analysis of the alpha scattered at large angles, the surface density of impurities present inside the solid matrix is quantified, together with its depth. The main physical phenomenon exploited in this technique is the Coulombian interaction between the nuclei of the sample in analysis and the accelerated alpha particles that impinge on it, which in our case are $^4He_{++}$. To ensure that scattering is of Coulombian type and that no nuclear reactions occur, $^4He_{++}$ particles are accelerated at about 2 MeV. At this energy, the backscattering cross-section σ(E,θ) on all elements more massive than Be is described by the Rutherford formula:

$$\sigma_R(E,\theta) = \left(\frac{Z_1 Z_2 e^2}{4E}\right)^2 \cdot \frac{4(\sqrt{m_1^2 - m_2^2 sin\theta} + m_2 cos\theta)^2}{m_2 sin^4\theta \sqrt{m_1^2 - m_2^2 sin\theta}} \tag{2.1}$$

where θ is the scattering angle, (Z_1, m_1) and (Z_2, m_2) are the atomic numbers and masses of the incident and target ions, respectively, and E is the incident particle energy. This equation implies that, for a given incident particle, heavy atoms are much more efficient scattering centers than light atoms. Therefore, backscattering spectrometry is much more sensitive to heavy elements than to the light ones.
We can understand how impurity atoms that are inside the sample can be recognized simply through the analysis of the scattered beam, by applying energy and momentum conservation principles and writing the expression for the backscattering energy:

$$E_{out} = K \cdot E_0 = \left(\frac{m_1 cos\theta + \sqrt{m_2^2 - m_1^2 sin^2\theta}}{m_1 + m_2}\right)^2 \cdot E_0 \tag{2.2}$$

where *K* is also called *kinematic factor*. Being E_0, m_1 and θ experimental parameters, by measuring the energy of the backscattered beam we can calculate m_2 and thus identify the target element. The quantification of the areal density N_s of the i^{th} target

element, i.e. the number of atoms per unit area, is obtained from the detector solid angle Ω, the integrated peak counts A_i, the number of incident ions Q and the cross-section $\sigma_i(E, \theta)$, using the following formula.

$$(N_s)_i = \frac{A_i cos\theta_i}{Q\,\Omega\,\sigma_i(E,\theta)} \tag{2.3}$$

The technique, once known the solid angle and the number of impinging atoms, allows to accurately determine the chemical profiles of elements on the basis of the well known Rutherford cross section. From the knowledge of the stopping power of a material for a particular ion (defined as the energy loss per distance covered into the target dE/dx), it is possible to relate the energy of the scattered particles to the depth travelled in the sample.
The measurements present in this work were done at the AN2000 accelerator located at the INFN National Laboratories of Legnaro (LNL). The complex apparatus consists of a particle accelerator, a scattering chamber and an acquisition system. The accelerator is a linear Van der Graaf, with 2 MeV maximum energy. The helium ion beam is selected and focused along a line that arrives to the scattering chamber. Both the beam line and the scattering chamber are kept under high vacuum. Inside the chamber, samples are mounted on a powered goniometer manageable from remote. The detectors, that are reversely biased diodes, are mounted in a movable system that allows to select the backscattering angle to which the measurements are performed. The chamber walls are electrically isolated from the rest of the apparatus, because it is used as a Faraday cage to accurately measure the current impinging on the sample (from which the incident charge Q is calculated). Through a electronic chain and an acquisition software, the instrumentation is remotely controllable and RBS spectra can be collected.

2.4 Van der Pauw electrical measurements

Four-point probe, or in general four-wire, electrical measurement is a very useful technique in the field of semiconductor research. In the in-line configuration (Fig. 2.4a), this technique allows to measure the semiconductor resistivity, simply by delivering a constant current through the outer two probes and measuring the induced voltage between the inner two. The reason why four wires are used instead of two, is that in this way you can make a measure independent on the resistances of leads and contacts. In fact, the circuit made of the inner leads and the voltmeter is dominated by the huge resistance of the voltmeter, therefore just a very small contribution

of the current flowing in the sample will deviate into it. In this way, the potential drops due to lead and contact resistances are negligible and the real potential difference induced by the resistance of the sample can be measured. The same kind

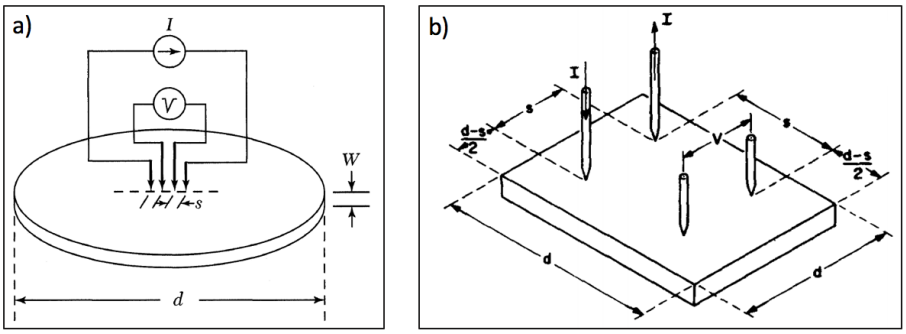

Figure 2.4. a) Schematic representing an in-line four-point probe system. b) Schematic representing a square four-point probe system. [56]

of measurement can be done with a square array of point-probes, by delivering the constant current through two adjacent probes and measuring the induced voltage between the other two, so that the two couples of contacts are parallel, see Fig. 2.4b. By knowing the current value I that you are delivering and the measured potential difference ΔV, in both configurations (in-line and square) the sample resistivity ρ is calculated by applying a multiplicative correction factor related to the quantity d/s, where d is the sample size and s the probe spacing. The two points giving the current drive a sort of dipolar field into the sample (not exactly dipolar because of the sample boundaries) and the voltage drops at the voltage probe tips linearly depend on the applied current through a geometrical factor [57]. Such factor depends on the sample shape and tip position.

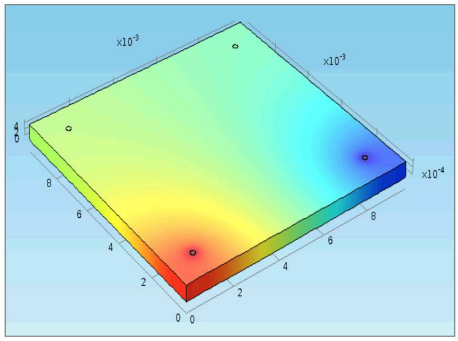

Figure 2.5. Simulation representing the electrostatic potential caused by two tips close to the side of a square.

In Fig 2.5 the electrostatic potential caused by two tips close to the side of a square

is shown. The calculation of correction factors will be described in paragraph 2.4.3. Before 1958 Hall-effect measurements, used to measure the charge-carrier density inside a semiconductor, were done only on rectangular test bars (Fig. 2.6), in the following way. A constant current is delivered along the x-axis through contacts M and

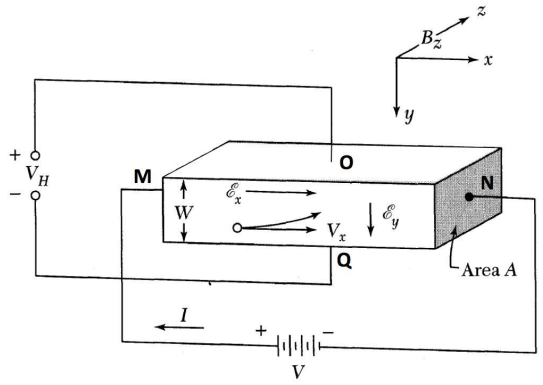

Figure 2.6. Rectangular test bar conventionally used to do Hall-effect measurements. [56]

N and a magnetic field B is applied along the z-axis. The Lorentz force will exert an average upward force on charge carriers flowing in the x-direction. The upward directed current causes an accumulation of carriers at the top of the sample, that gives rise to a downward-directed electric field. Since there is no net current flow along the y-direction in the steady state, the electric field along the y-axis exactly balances the Lorentz force and carriers drift only in the x-direction. The established electric field is known as *Hall field* and the voltage induced between O and Q contacts *Hall voltage* [56]. The Hall field results equal to:

$$E_H = \frac{1}{nq} JB \tag{2.4}$$

where R_H=1/(nq) is called the *Hall coefficient*.
In 1958/59, Van der Pauw published two important papers [58, 59] in which he demonstrated that it is possible to perform both resistivity and Hall measurements in flat samples of arbitrary shape (Fig. 2.7) without knowing the current pattern, if the following conditions are fulfilled:

- the four contacts are at the perimeter of the sample;
- the contact size is sufficiently small;
- the sample thickness is homogeneous;

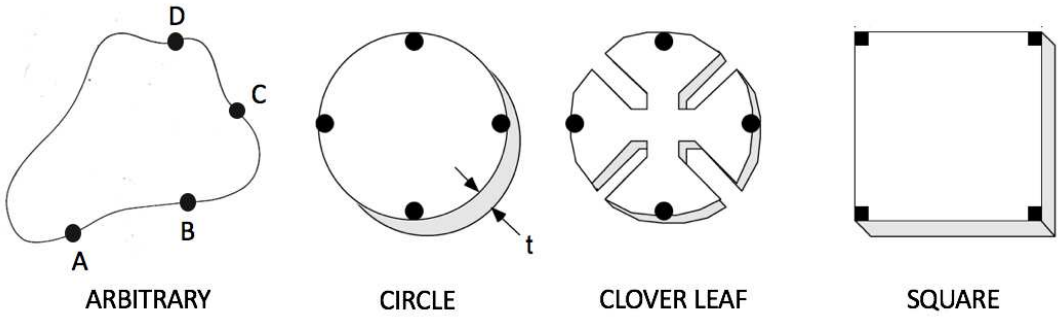

Figure 2.7. Various sample shapes that can be used to perform resistivity and Hall measurements according to the Van der Pauw method.

- the surface of the sample is singly connected, i.e. doesn't have isolated discontinuities.

For what concerns the resistivity measurement, in his theorem he demonstrates that the following equation holds:

$$exp\left(-\frac{\pi t}{\rho}R_{AB,CD}\right) + exp\left(-\frac{\pi t}{\rho}R_{BC,DA}\right) = 1 \tag{2.5}$$

where t is the thickness, ρ is the resistivity of the material and the resistances $R_{AB,CD}$ and $R_{BC,DA}$ are described in Eq. (2.6) and (2.7).

$$R_{AB,CD} = \frac{V_D - V_C}{I_{AB}} \tag{2.6}$$

$$R_{BC,DA} = \frac{V_A - V_D}{I_{BC}} \tag{2.7}$$

If these resistances are measured, then the resistivity ρ can be calculated form Eq. (2.5).
Regarding the Hall-effect, Van der Pauw showed that if the above geometric conditions are respected, one can perform Hall measurements on a flat arbitrary sample in the following way.
The current signal is delivered at contacts A and C and then the voltage has to be measured at contacts B and D (see Fig. 2.8), before and after the application of a magnetic field orthogonal to the sample surface. The Hall coefficient can be calculated as follow.

$$R_H = \frac{t}{B}\frac{\Delta(V_D - V_B)}{I_{AC}} \tag{2.8}$$

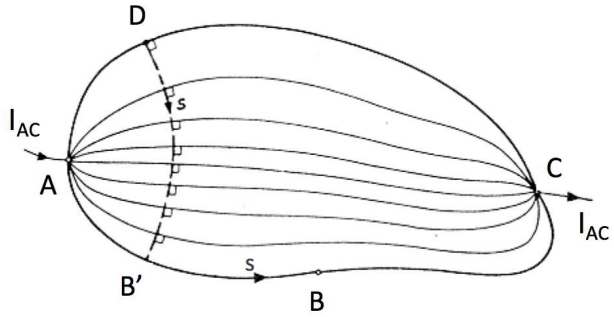

Figure 2.8. The transverse electric field E_t produced by the magnetic field is integrated along the path s that runs from D to B' (orthogonally to the current stream-lines) and then from B' to B along the perimeter. [58]

This relation holds because, if the geometrical requirements are respected, the outer current stream-lines that run along the perimeter of the sample determine the boundary conditions, and they don't change their direction when a magnetic field is applied. Therefore, the effect of a magnetic field on the electric potential is such that between two arbitrary points, D and B, an additional Hall potential difference $\Delta(V_D\text{-}V_B)$ is built up equal to:

$$\Delta(V_D - V_B) = \int_D^B E_H \, ds = R_H B \left(\int_D^{B'} J \, ds + \cancel{\int_{B'}^{B} J \, ds} \right) = R_H \, B \, \frac{I_{AC}}{t} \tag{2.9}$$

where E_H is the transverse Hall field described in Eq. (2.4). The integral from B' to B is null because, along the perimeter, the current stream-lines don't change when the magnetic field is applied and a transverse field does not arise. Equation (2.9) leads directly to Eq. (2.8).
The Van der Pauw method allows to perform both resistivity and Hall measurements on pieces of semiconductor material of arbitrary shape, simply by placing all four contacts or point-probes on the front surface. This is actually a rapid method to characterize small square samples.

2.4.1 Setup description

Our setup for electrical measurements according to the Van der Pauw method is quite simple, but it is sufficiently refined to have accurate results. It consists of a small chamber, that can be also evacuated for variable temperature measurements, containing a ceramic sample holder and the square four-point probe contact system (Fig. 2.9). Points are gold plated and very thin (∅ = 0.5 mm). Each one is equipped with a spring and is sustained by a long arm so to lean gently on the sample surface. The instrument also offers the possibility to use a printed circuit instead of the

four-point probes. If the sample is equipped with metal contacts, it can be bonded to the printed circuit pads. The setup is completed with a permanent magnet for

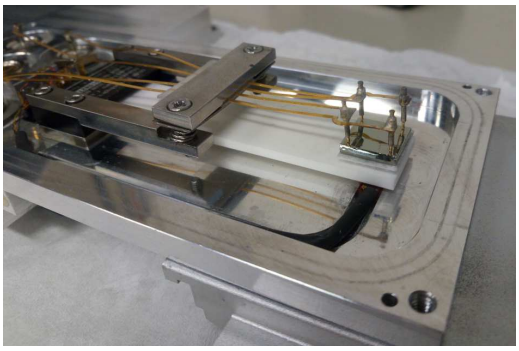

Figure 2.9. Four-point probe contact system.

Hall measurements, a sourcemeter, a switch matrix and a remote control. Current signals are provided by a Keithley 2600 sourcemeter, which is used also for voltage measurements. It is remotely controlled through a customized software, which exploits a switch matrix to make permutations of the four contacts. In fact, each measured value of resistivity or Hall coefficient, is the result of many voltage measurements that are done by permutating the four contacts, in order to compensate as much as possible the errors induced for instance by contact resistances or doping inhomogeneity.

Two apparatus for variable temperature measurements

In the field of semiconductor research, the possibility to perform electrical measurements with varying temperature is very important, because semiconductor materials change their electrical properties depending on the temperature regime. Particularly, the energy gap, the density of intrinsic charge carriers, the density of ionized extrinsic doping levels are function of temperature.
In a first period, we used a customized setup for variable temperature electrical measurements, that is called *setup No.1*. It is partially shown in Fig. 2.10a and it is composed of a liquid-nitrogen (LN2) cryostat, a temperature controller remotely managed and a source-meter with acquisition software for electrical measurements. The sample to be measured is positioned inside the cryostat, at the end of the cold finger, where it is sustained by a sample holder. This consists of a metallic block containing an electrical resistor and a thermocouple. Above it, a piece of sapphire wafer (thermo-conductive material) is fixed to sustain the sample. After having positioned the sample (that in this case must be equipped with metal contacts), four

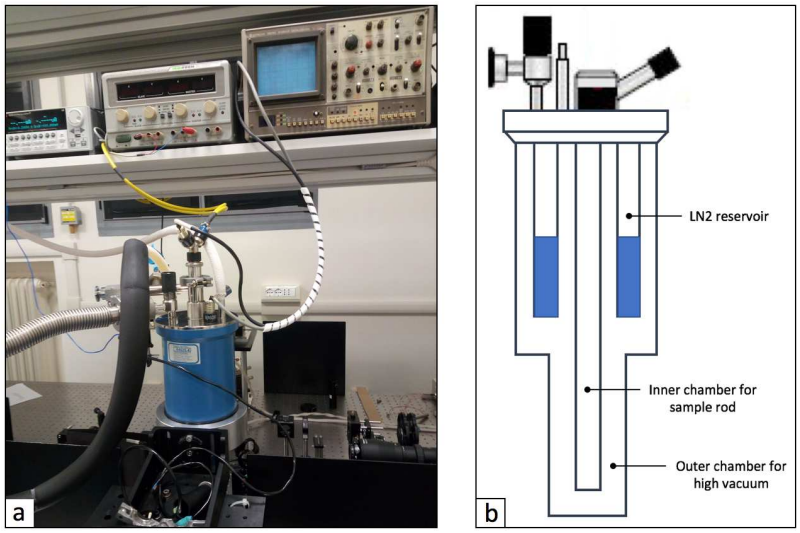

Figure 2.10. Setup No.1 for sheet resistance measurements at low temperature. a) Picture of part of the setup: in the foreground there is the cryostat, with various pipeworks needed for nitrogen injection/exhaustion and for chamber vacuum. b) Schematic of the cryostat: the inner chamber houses the sample rod and is filled with He gas; the intermediate chamber is filled with liquid nitrogen; while the outer chamber is kept in high vacuum to avoid the external condensation.

wires are bonded to metal pads through malleable indium and the whole is pressed against sapphire through a PEEK bridge (Fig. 2.11). In Fig. 2.10b a schematic of the

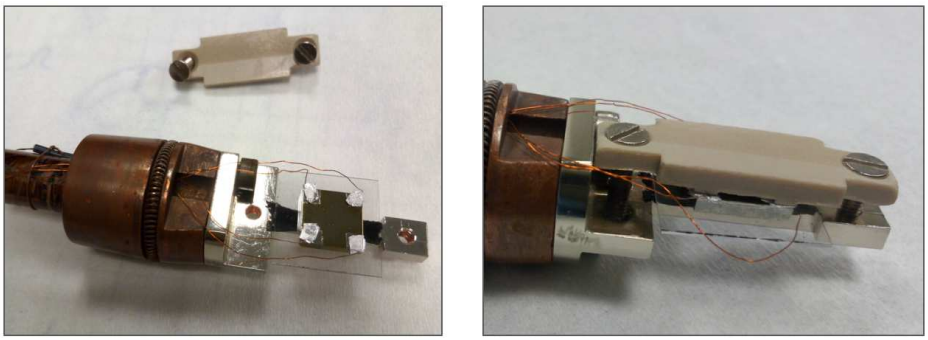

Figure 2.11. Sample holder. On the right a bridge made of PEEK material is positioned above the sample (already contacted with Cu wires and malleable In) and fixed with screws to keep the sample stable.

cryostat is reported. The cold finger is located in the inner chamber of the cryostat, filled of He gas. It acts as the refrigerator medium. LN2 instead is in the intermediate chamber and it is isolated from the external environment by an outer chamber under vacuum. Thanks to an external temperature controller that controls the resistor of the sample holder, each temperature value within the range [120-300] K can be set. Very important is the use of two vacuum pumps, a rotary one and a turbo-

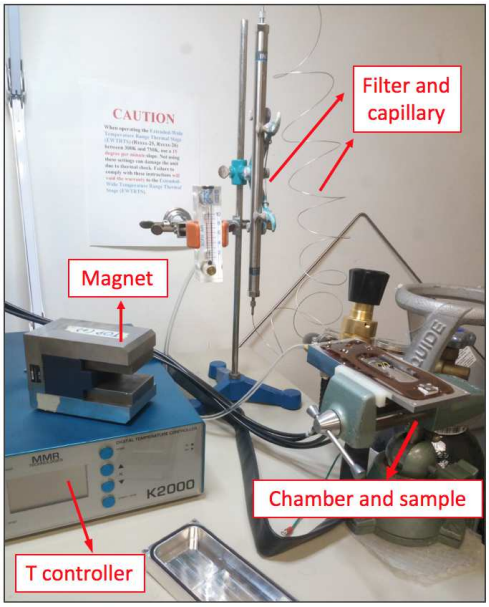

Figure 2.12. Setup No.2: on the right there is the vacuum chamber opened, with a sample placed on the Joule-Thomson refrigeration circuit. The thin cylinder behind is the N_2 gas filter, connected both to the N_2 tank and the vacuum chamber through capillary tubes. On the left, there is the permanent magnet and the temperature controller.

molecular one. During the setup preparation, they are used to evacuate the inner chamber before He filling. Then, they are used to do and keep a good vacuum in the outer insulating chamber. This cryostat doesn't allow to do Hall measurements, because it is not possible to put a magnetic field close to the sample, due to the mechanical form of the cryostat. Therefore, we performed only the sheet resistance measurements at several temperature values, by using the Van der Pauw method.
At a later period, we had the opportunity to buy and instal a temperature control system as a completion of the four-point probe apparatus described at the beginning of this paragraph 2.4.1. Its installation was part of my activity. The complete apparatus is shown in Fig. 2.12 and it will allow us to perform more complete electrical measurements with varying temperature, including the Hall effect thanks to the possibility of applying a magnetic field. This second apparatus for variable temperature electrical measurements is called *setup No.2*. In this case the temperature control system is different: first, a thermal stage for sample sustain and cooling is installed inside the vacuum chamber. It is composed of a Joule-Thomson micrometer refrigeration circuit, in which high-pressure N_2 is injected and expanded, provided with a ceramic stage for thermal contact with the sample. N_2 gas is purified through a filter-dryer system to remove both the water and the other condensable contami-

nants and then is injected into the refrigeration circuit at a pressure of ∼124 bar (1800 psi). During the operation the chamber is kept at 5×10^{-3} bar vacuum level through a rotary and a turbomolecular pump. The system is complemented by a remotely-manageable temperature controller. With this apparatus a wide range of temperature can be investigated [77-700] K. The shape of the sample chamber is quite thin, so it is now possible to use a permanent magnet to induce a homogeneous magnetic field on the sample and perform Hall effect measurements.

2.4.2 Measurement protocol

In this thesis two kinds of samples have been measured with this technique: massive HPGe samples (1 cm^2 area, 2 mm thickness) in which the electrical properties of the whole bulk volume are investigated; alternatively, samples either thin or thick, of HPGe or Ge, in which just the processed surface layer has to be characterized. In the latter case, the doped surface layer is created above a HPGe substrate (already highly resistive), or above a conventional Ge substrate (more conductive) but of opposite carrier type with respect to the surface layer. In this way, if the doping process was good, a p-n junction is formed between the surface layer and the Ge substrate, and the resistive depletion region provides enough electrical isolation between the two (Fig 2.13).
Otherwise, if the fabricated surface doping is not efficient or continuous, leakage down into the substrate will occur and the substrate electrical properties will be measured. This phenomenon has been used as a rapid preliminary test about the quality of fabricated contacts.

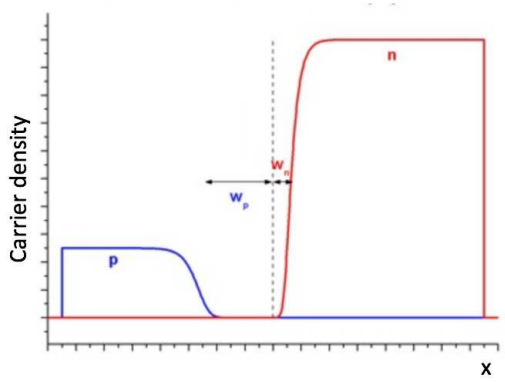

Figure 2.13. Asymmetric p-n junction. The higher the doping level in the surface layer (red profile), the thicker the resistive depletion region w_p inside the substrate (blue profile).

Resistivity measurements

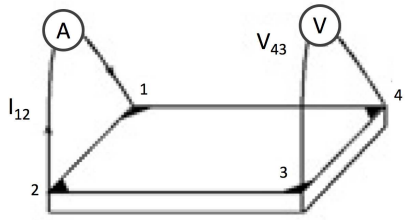

Figure 2.14. Parallel-contact configuration for resistivity measurements.

The adjacent contacts placed at the corners of a square sample are enumerated from 1 to 4, as can be seen in Fig. 2.14. Then, to perform a resistivity measurement, a positive current is delivered at the two forcing electrodes and the voltage induced through the other parallel couple of contacts is measured. This is done automatically with the help of a software for 8 different contact permutations (always in parallel couples, never crossed), including also the switch of contacts for each couple; then these measurements are repeated by delivering current of negative sign. Thus, in total 16 voltage values are collected and averaged, of course taking into account the current sign. The first quantity to be calculated is the sheet resistance, that is the resistivity per unit thickness. It is useful to evaluate the conduction properties of a very thin layer, sheet resistance can be thought as the resistance of a thin layer of square shape contacted at two opposite sides. The unit of sheet resistance is Ohm (Ω·cm/cm) but, in order not to confuse it with a normal resistance its unit is referred as *Ohm per square* ($\Omega/sq.$ or $\Omega/\square$).
By averaging the 16 (V/I) quantities, in order to compensate errors due to a not perfectly square contact placement, and applying the correction factors, we obtain the sheet resistance of the sample or surface-layer. From it, the resistivity ρ can be calculated by multiplying R_s by the thickness t, when it is known (Eq. (2.10)).

$$\rho = R_s \cdot t \tag{2.10}$$

An important practical choice, in order to have accurate measurements, is the intensity of the current to drive during measurements. It is crucial because if the current is not high enough to induce a detectable potential difference, false or erroneous voltages could be measured. On the contrary, if the current is too high, heating effects could arise within the semiconductor affecting the result.
In order to find the correct working current, a series of sheet resistance measurements are done probing a wide range of currents. A plot R_s *vs.* I is drawn looking

for a plateau, so a region where the sheet resistance doesn't change with current. Then, a value of current within that plateau is chosen [60].

Hall-effect measurements

For the measurement of the Hall coefficient, the chamber containing the sample is inserted inside the permanent magnet of constant magnetic field 0.625 T. In this case crossed couples of contacts are used, as it is shown in Fig. 2.15, in order to be sensitive to the Hall voltage. Hall voltages are measured after delivering a positive

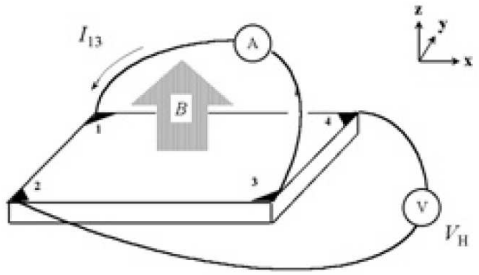

Figure 2.15. Crossed-contact configuration for Hall measurements.

current for 2 different contact permutations, and then repeating the measurements by delivering current of negative sign. The same is done after having inverted the magnetic field. Thus 8 voltage values are measured and they are averaged taking into account the current signs. The first quantity to be calculated is the Hall coefficient independent on sample thickness (because sometimes we could not be aware of it), as shown in Eq. (2.11).

$$RH_s = \frac{\langle V \rangle}{IB} \tag{2.11}$$

From it, the carrier number by unit area of the sample can be calculated, also called *dose*:

$$n_s = \frac{1}{RH_s \cdot e} \tag{2.12}$$

If the thickness is known, one can calculate the Hall coefficient by multiplying RH_s by t and the volume density (concentration) of charge carriers by dividing n_s by t. Therefore, the system allows to directly measure two physical quantities, the sheet resistance/resistivity and the dose/concentration of active carriers (calculated from the Hall coefficient). Then, with these two quantities one can derivate the value of

carrier Hall mobility, as the ratio between RH_s and R_s:

$$\mu = \frac{RH_s}{R_s}. \tag{2.13}$$

Also for Hall-effect measurements, a preliminary RH_s *vs. I* curve is created and the working current is chosen within a region of constant RH_s.
In cases where the Hall-effect measurement can not be accomplished, due to the impossibility of applying a magnetic field or due to high measurement errors, one can still estimate the dose of active carriers. It could be done by measuring the sheet resistance, take mobility values from the literature and then derive the carrier dose through Eq. (2.13) and (2.12). This procedure will be adopted in paragraph 5.2.3.
An interesting question, still not enough investigated, is the relation between Hall mobility and drift mobility. In fact, it has been proven that charge carriers move with a different velocity in the semiconductor when magnetic field is applied, due to a second order effect. Unfortunately there is not thorough literature on this behaviour [61, 62]. It can be quantitatively described by the following relation between drift and Hall mobilities:

$$\mu_{Hall} = r_H \cdot \mu_{drift} \tag{2.14}$$

where the multiplicative factor r_H is called *Hall factor*. As regarding germanium, Hall factor values are known only for carrier concentrations higher than 10^{14} cm^{-3} [63].

2.4.3 COMSOL® modeling

In practice the geometric requirements at the basis of the Van der Pauw method, for resistivity and Hall measurements, are not always met. Particularly those regrading contact size (that should be point-like) and contact position (contacts should be placed at the four vertexes of a square sample). If these conditions are not met, an error is introduced in both resistivity and Hall measure. In the literature there are many papers reporting correction factors for samples and contacts of various shape [64]- [75].
Almost all of them used the finite element method to solve equations, find the potential distribution in 2D and then calculate correction factors. First attempts were done manually, while in the last two decades software packages have been used to carrie out all calculations thus increasing the accuracy. We decided to calculate correction factors with the modeling software *COMSOL® Multiphysics*, in order to

consider from time to time the peculiar geometry we are dealing with. The software uses the finite element method to discretize geometries and solve physical partial differential equations numerically. In particular, we use equations of electrostatic and magnetostatic and the charge-continuity equation, solved in stationary regime.

$$\begin{cases} \vec{\nabla} \cdot \vec{J} = Q_j \\ \vec{E} = -\vec{\nabla} V \\ \vec{J} = \sigma \vec{E} + \vec{J_e} \\ \vec{D} = \epsilon_0 \epsilon_r \vec{E} \end{cases}$$

When we want to model a resistivity measurement, we assume the conductivity σ of the material as isotropic, so it is considered as a scalar quantity equal to $ne\mu$.
On the contrary when Hall-effect measurements are modeled, the material conductivity becomes anisotropic and it can be considered as a non-symmetric rank 2 tensor (Eq. (2.15)). If a magnetic field is applied orthogonally to the sample surface, i.e. in the $\vec{z}$ direction, the σ_{xx}, σ_{xy}, σ_{yx} σ_{yy} components of the tensor change, due to magnetoresistive effects associated with second-order terms in μB. The σ_{zz} component instead remains unchanged [74,76].

$$\begin{bmatrix} \frac{ne\mu}{1+(\mu B)^2} & \frac{-\mu B(ne\mu)}{1+(\mu B)^2} & 0 \\ \frac{\mu B(ne\mu)}{1+(\mu B)^2} & \frac{ne\mu}{1+(\mu B)^2} & 0 \\ 0 & 0 & ne\mu \end{bmatrix} \tag{2.15}$$

In Fig. 2.16 we report the models of two standard samples that we used to measure in the lab, designed in scale with COMSOL drawing tools. Fig. 2.16a refers to a square sample of thin Ge wafer (t $\sim$500 μm) measured through the four-point probes. Fig. 2.16a represents a square sample of thick HPGe wafer (t $\sim$2 mm), with square metal pads that in practice can be bonded to the printed board or touched with the four-point probes. An important boundary condition is imposed on the four contacts: being floating equipotential surfaces. This mimics the presence of a metal in contact with them.

Correction factors for standard geometries

Through this kind of simulations we evaluate geometrical correction factors for the non-pointlike size of contacts and their position not-precisely at the sample perimeter. To do this we perform two simulations: one by designing a real experimental configuration (as shown in Fig. 2.16) and one by designing an ideal measurement

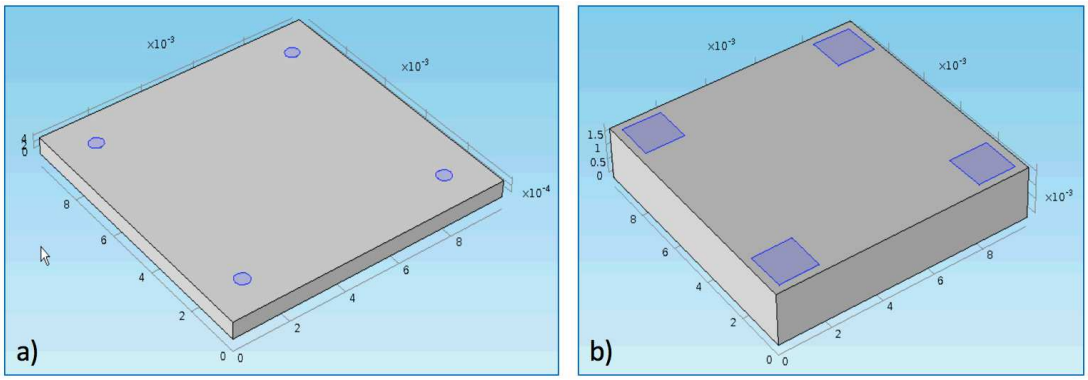

Figure 2.16. In scale models of samples we are used to measure in the lab, designed with COMSOL drawing tools. a) A square sample of thin Ge wafer (t ∼500 μm) measured through the four-point probes. b) A square sample of thick HPGe wafer (t ∼2 mm), with square metal pads.

configuration, that is pointlike contacts placed at the vertices of a square sample. Then, we compare the results and calculate a correction factor that simultaneously correct both the unideal aspects (contact size and position). This is due for both resistivity and Hall-effect measurements.
Considering the two experimental configurations that we usually adopt (showed in Fig. 2.16), we have calculated resistivity and Hall correction factors for both of them. Obtained value are reported in Table 2.1.

Table 2.1. Correction factor values for sheet resistance (F_R) and carrier concentration (F_n). They refer to geometries a) and b) of Fig. 2.16.

	Geom. a)	**Geom. b)**
F_R	1.005	1.01
F_n	0.90	0.84

Modeling validation

In order to validate our simulations, we decided to compare our results with the literature. Considered the simplest case, i.e. the calculus of the correction factor for a resistivity measurement, we took the paper by Chwang [64] for comparison and reproduced his sample (a 2D square sample with four triangular metal pads exactly at the vertexes, see Fig. 2.17a). In Fig. 2.17b the model we designed is reported together with a representation in colors of the electric potential generated by a simulation. We did resistivity measurement simulations with this configuration and with the ideal one. Then correction factors were extracted for several δ/L values,

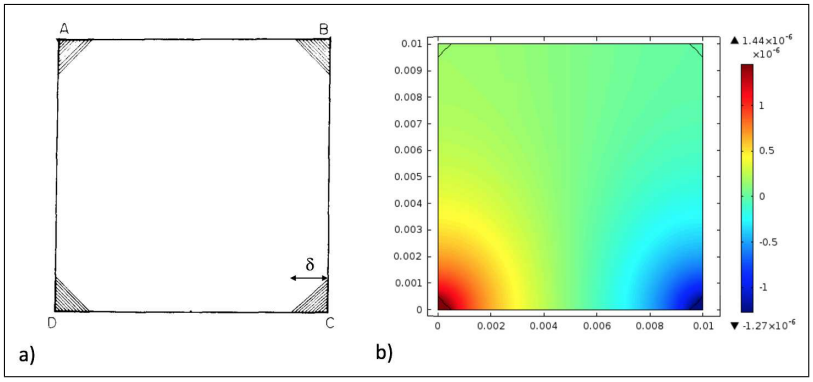

Figure 2.17. a) Sample used in paper by Chwang [64] to calculate resistivity correction factors. b) The same sample has been designed with COMSOL drawing tools; the electrical potential generated by a measurement simulation is represented in colors.

being δ the contact side and L the sample side. The curve representing the resistivity

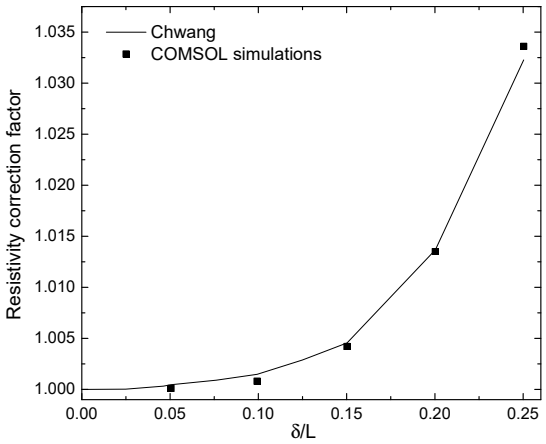

Figure 2.18. Comparison between resistivity correction factors calculated in the paper by Chwang [64] and those calculated with our simulations.

correction factor as function of δ/L was digitized from the paper by Chwang and compared with our results, in Fig. 2.18. Between our data and Chwang curve there are small discrepancies. They are likely due to the fact that Chwang modeled the resistivity measurement by approximating the sample to a network of resistances and then he solved numerically the physical problem via an iterative over-relaxation method, with the computing power that was available in 1974. Anyway, apart for small discrepancies, the two results are compatible so we consider our modeling method validated. For each new sample type or measurement configuration we use our model to calculate resistivity and Hall correction factors.

2.4.4 Joint analysis of sheet resistance and SIMS profile

Generally, Hall measurements are more delicate than resistivity ones and in some cases it may be very difficult to make them with enough accuracy. In fact, Hall voltages are usually small and in samples characterized by inhomogeneous doping, they can be smaller than offset voltages present with zero magnetic field. In such cases, by changing the sign of the applied magnetic field, the Hall voltage sign doesn't change because the zero-field offset has not been exceeded and the measurement must be cancelled. As a matter of fact, in many cases of not perfectly homogenous and continuous doping of our samples (samples with surface defects for instance), the sheet resistance value resulted to be reasonable, while the Hall measurement was affected by errors and presented strong discrepancies with respect to literature mobility values.
When only the sheet resistance (or resistivity) value is measurable, together with the dopant concentration profile (measured through SIMS), these two results can be analyzed to derive an indicative value for the dose of active carriers. The dopant concentration profile as function of depth can be imagined as the sum of many layers of thickness dx, concentration C_i and resistivity ρ_i, connected in parallel with each other. Then, being aware that R_s=ρ/t the overall sheet resistance can be defined through Eq. (2.16).

$$\frac{1}{R_s} = \int \frac{1}{\rho_i} x_i \, dx \tag{2.16}$$

The resistivity curve as function of concentration in Ge ($\rho(C)$) has been taken from the literature [77]. Through this curve, for each infinitesimal interval Δx of the SIMS profile, by knowing the concentration C_i we can derive the correspondent resistivity value from literature. In this way the concentration profile is converted into a resistivity profile. Then, through Eq. (2.16), this resistivity profile is integrated and the sheet resistance calculated. In principle, not all the dopant chemical concentration revealed by SIMS must be electrically active. Under the hypothesis that there could be a maximum concentration of active dopant, the calculus is done many times by setting increasing maximum thresholds. Practically, a table with different possible sheet resistances, corresponding to different maximum activation levels is numerically produced. By comparing the experimental value with that table an estimate of the maximum active concentration is obtained.
Here we report an example of such an analysis, done on a HPGe sample that was ion implanted with 1x10^{15} cm^{-2} boron atoms with a standard procedure, without any post-implantation annealing in order to avoid any bulk contamination. First,

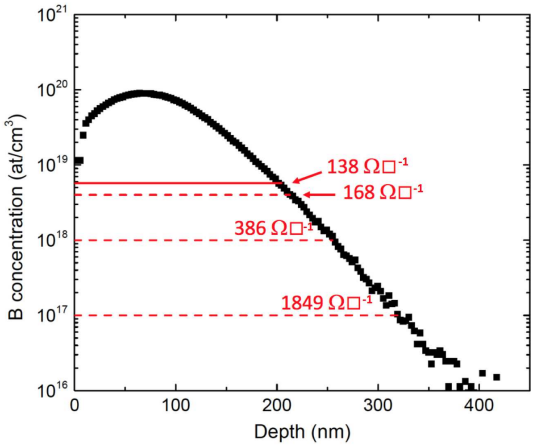

Figure 2.19. SIMS characterization of a B implanted layer (black profile). Red dashed lines are activation thresholds fixed for the calculus of the sheet resistance. The red continuous line represents the active concentration (5.8x10^{18} cm^{-3}) correspondent to the experimental sheet resistance.

the concentration profile of B atoms inside Ge was measured through SIMS and it is reported with black symbols in Fig. 2.19. Then, four-point probe electrical measurements were done obtaining a sheet resistance value of (138±2) Ω/sq. During the procedure described above, several thresholds for the maximum electrically active concentration have been fixed and the correspondent sheet resistance calculated. As it can be observed in Fig. 2.19, the calculated sheet resistance equals the experimental value for an active concentration of 5.8x10^{18} cm^{-3} (red continuous line). This method is efficient and, in some cases, it is the only one that can be used to determine the electrical activation of a doped layer. This happens when dopant atoms are not homogeneously distributed inside a layer and, consequently, Hall-effect measurements are not accurate at all.

In the course of the thesis, this method will be applied in Chapter 3 on phosphorus-doped Ge layers, in order to confirm the results of Hall-effect measurements. In Chapter 4 instead, as regarding the antimony-doped Ge layers from sputtered sources, four-point probe electrical measurements were not feasible, neither to find the sheet resistance nor the dopant activation, because of surface damages (in case of direct Sb source) or too low doping levels (in case of remote Sb source). For what concerns the Sb doping by laser thermal annealing, this method will be employed to evaluate the dopant activation, in parallel with Hall-effect measurements.

Chapter 3

Optimal process parameters for P spin-on-doping of Ge

The fabrication of homogeneously doped germanium layers characterized by total electrical activation is currently a hot topic in many fields, such as microelectronics, photovoltaics, optics and radiation detectors. In principle, *spin-on-doping* (also called SOD) is an inexpensive technique, easily applicable in a research lab. Starting from a sol-gel source containing a high concentration of dopant atoms of the desired species, the technique allows to introduce dopants inside the host matrix by thermal diffusion, without generating lattice defects. According to the literature, thin and thick doped layers (from 50 nm to a few microns) of both p- and n type can be obtained, characterized by a good lattice quality and full activation of the dopant [78]. A medium-temperature thermal treatment is necessary for diffusion (ranging from 500 °C to 850 °C depending on the doping type and required specifications), achievable with a standard furnace [79–81]. The trickiest aspect in the application of this technique is the thermal curing process of the sol-gel source, as demonstrated for treatments in silicon in Ref [82].
While these sources have been widely employed in Si doping, their application to Ge is less known, hence the optimization of a protocol for their deposition and curing is needed [83]. In this chapter, a systematic investigation of curing parameters has been performed in order to better understand the chemical and physical mechanisms causing detrimental effects and their correlation with P incorporation and activation. The possibility to define an optimized process window to reach very good doping performances will be shown.

3.1 Sample preparation

Before starting the description of the experimental procedure, some information should be given about the sol-gel process. This process involves the synthesis of a colloidal suspension (*sol*) and gelation of the sol to form a solid inorganic network (*gel*) holding the continuous liquid phase. The compounds that will be used in this thesis are silica-based. Generally, the gelation process takes place through two main reaction of hydrolysis and condensation. Hydrolysis occurs by the attack of the water oxygen to the silicon atom, thus splitting more complex molecules. Two hydrolyzed molecules containing Si atoms can link together through a condensation reaction, with the release of a small water or alcohol molecule. Condensation reactions can continue to build larger and larger silicon-containing molecules by the process of *polymerization* [84]. One then refers to polymer *reticulation* when polymer chains bond one to another with the formation of ionic or covalent cross-links, thus forming a net.
Spin-On Diffusants (SOD) are used in the semiconductor industry as diffusion sources. Usually, a silica-based *sol* is produced or bought, containing a certain concentration of dopant atoms. Then, the gelation process is done by spinning the *sol* on a semiconductor wafer in order to obtain a film. This kind of film can rapidly become a glass (in that case you have already obtained a so called *Spin-On Glass (SOG)*); otherwise it could need further hydrolysis and condensation reactions to become glassy and stable. P and Ga commercial Spin-On Diffusant solutions, that for this thesis were supplied by Filmtronics, belong to the second category so, after the film formation by spin-coating, they need a further reticulation step that will be called *curing*.

3.1.1 Spin-coating of the source film

A Ge wafer (100) p-doped ([0.04-0.4 Ωcm] resistivity) supplied by Umicore, was cut into 1x1 cm^2 samples and subsequently cleaned with hot 2-propanol, HF 10% and hot deionized (DI) water to remove cutting adhesive residues and native oxides. Each sample was warmed on a hot plate for a few minutes and then blown with nitrogen gas to completely remove any trace of humidity.
The surface was spin-coated with 40 μl/cm^2 of SOD solution supplied by Filmtronics (Fig. 3.1a), P-containing P507 solution for n-doping and Ga-containing Ga250 solution for some tests on p-doping. The spin coater, represented in Fig. 3.1b, has got a Teflon rotating support to which the sample stays anchored thanks to the

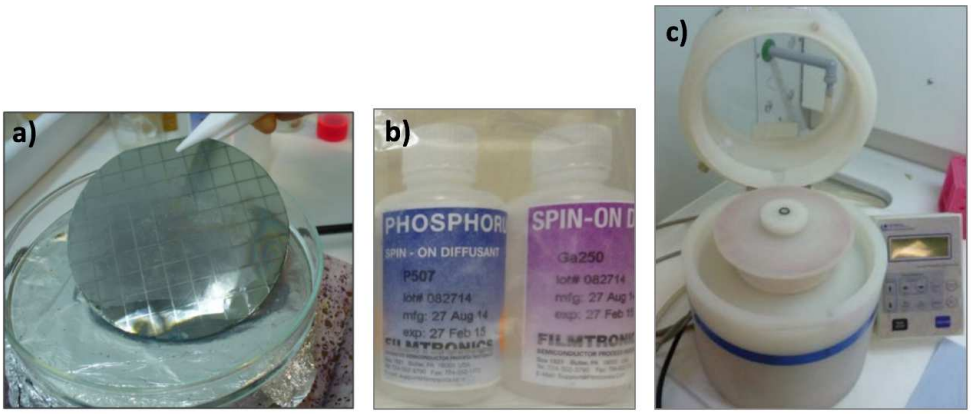

Figure 3.1. a) Ge wafer mechanically cut into 1x1 cm^2 samples. b) Filmtronics P507 (4% w/v P compound) and Ga250 (2% w/v Ga compound) sol-gel sources. c) Spin-coater apparatus.

suction of a vacuum pump. The spin-coater lid was equipped with lateral nitrogen flow, useful to blow the solution mist away from over the sample surface during rotation. Otherwise this mist could fall down into drops above the film. A downward pumping system eliminates the residues. The spinning cup must be cleaned with HF 10% after every film deposition, to remove SOD particles spilled out during the spinning. Figure 3.2 there is a schematic of the spin-coating procedure. Several spinning recipes were tried by changing spinning speed and time, obtaining

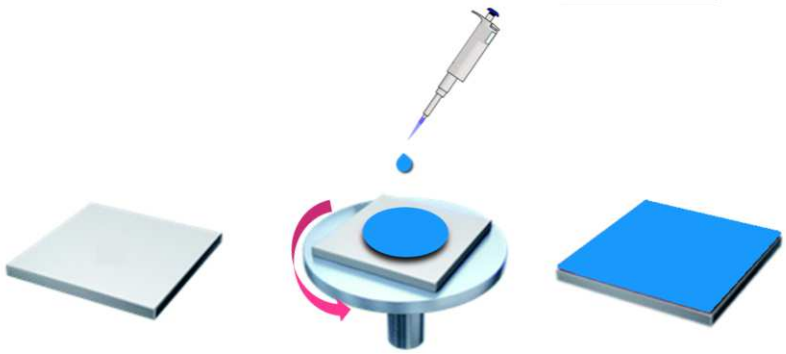

Figure 3.2. Schematic describing the spin-coating procedure.

different thicknesses. Table 3.1 reports the thickness of SOD films measured with a Tencor P-10 surface profiler at the center and at the edge of the samples, for different spinning recipes. By increasing the spinning time or speed, the sol-gel tends to accumulate at the sample edge, thus giving rise to a great difference in film thickness between the center and the edge of the sample. The best condition, i.e. a homogeneous thickness all over the surface and full coverage, was obtained

Table 3.1. Optimization of the spinning recipe. Edge and centre thickness of SOD films deposited through different spinning speeds and times are reported.

Speed (rpm)	Time (s)	Edge thickness (nm)	Center thickness (nm)
4500	15	236±3	220±3
4500	30	353±3	234±3
4500	60	247±3	150±3
6000	30	660±3	177±3
6000	60	404±3	183±3

with a rotational speed of 4500 rpm for 15 s followed by a deceleration stage. The optimization of film homogeneity and thickness during the spin coating step is very important for the final quality of the doped layer. In fact, the higher the thickness of the film, the more mechanical stress will be introduced during subsequent curing process and high temperature annealing, leading to the formation of cracks on Ge surface (reported in Paragraph 3.2.1). Besides, inhomogeneity in the film thickness across the sample surface may imply differences in the doping level after long time diffusion annealing.

3.1.2 Source film reticulation through curing

Once deposited, the film was cured on a hot plate at 130 °C for 15 min, inside a humidity-controlled glove box (Fig. 3.3), under nitrogen flux (that helps removing water vapour from the glove box). Since the relative humidity present inside the

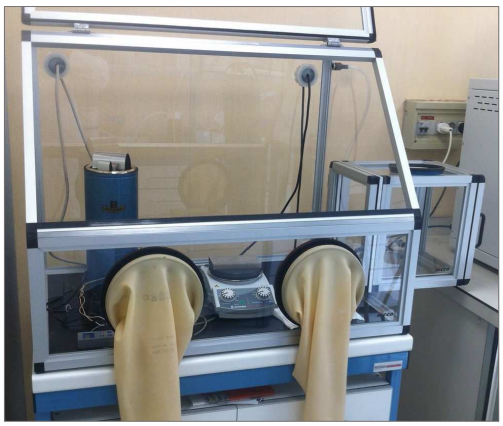

Figure 3.3. Picture of the glove box used to perform the curing of the sol-gel film in controlled-humidity atmosphere.

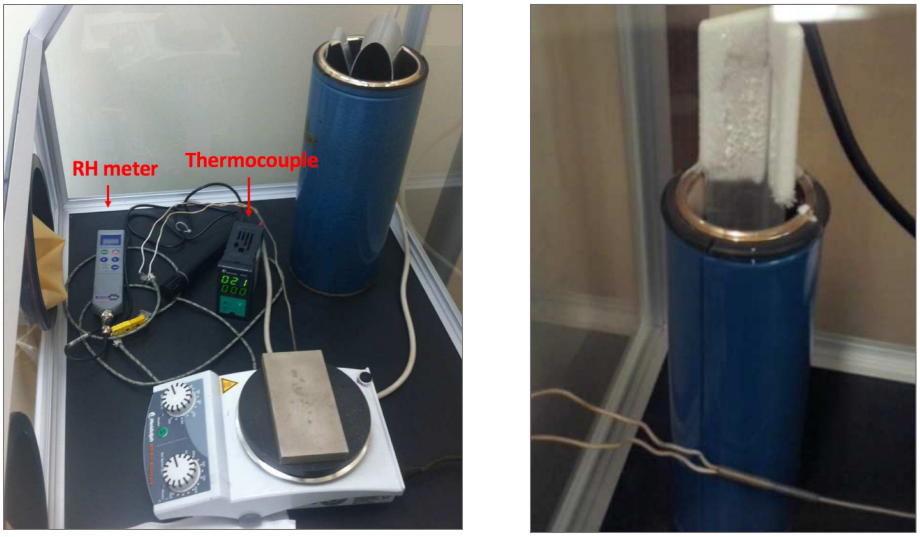

Figure 3.4. On the left, the apparatus inside the glove box is shown. It is possible to see the hot plate used for the curing of the SOD film, the thermocouple that measures the hot plate real temperature and the relative humidity meter. The picture on the right shows that when the dewar is full of liquid nitrogen, the humidity present inside the glove box condenses above the metal rod.

glove box is expected to be a crucial parameter for the process of reticulation of the sol-gel source, a first set of samples was cured under three different RH conditions: 5%, 30% and 50%. The highest and lowest values were obtained by respectively putting a pot with boiling water or a dewar containing liquid nitrogen plus a protruding metal rod, inside the glove box (see Fig. 3.4). A second set of samples was cured at 130 °C for different time intervals (15 min, 30 min, 1 h and 2 h), in order to analyze the degree of cross-linking reached by the sol-gel after every curing time. Finally, to understand also the role of curing temperature, one sample was heated up to 200 °C with 18 °C/min ramp, as suggested in Ref. [79]. After a slow cooling, each sample was capped with a piece of Si wafer to prevent the dopant out-diffusion from SOD source during high temperature annealing, and the whole was clamped between two quartz slides. Dopant diffusion was performed in a standard tubular furnace, equipped with a quartz tube and a transfer system (Fig. 3.5a). The latter allows to move the sample inside the quartz tube, from a cold lateral position to the middle of the furnace, where a homogeneous temperature environment is maintained. The transfer occurs by a permanent magnet guided system and allows to keep the furnace sealed. This allows to avoid external contamination (mainly oxygen) during the rapid sample transfer. Inside the quartz tube a constant nitrogen flow (∼400 sccm) was established after 5 vacuum/gas cleaning cycles, necessary to remove contaminants from the tube.

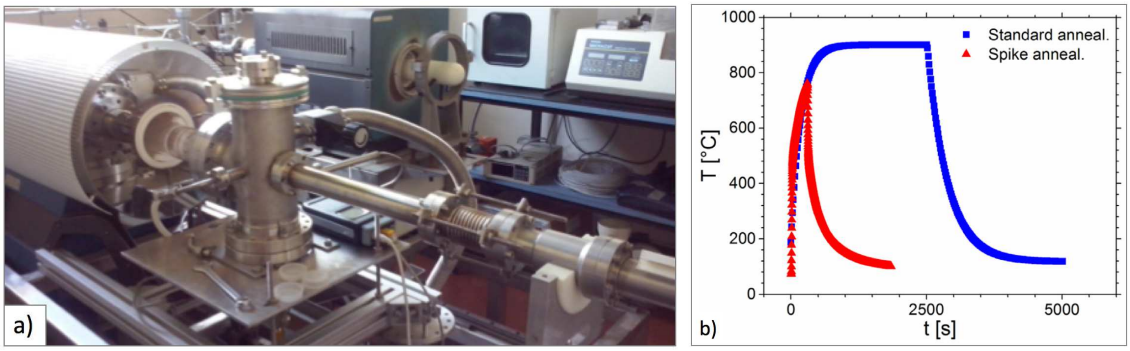

Figure 3.5. a) Photograph of the tube-chamber furnace. Detail of the system for a rapid sample insertion from the outside. b) Comparison between a spike annealing at 760 °C (red curve) and a standard treatment at 900 °C characterized by rapid insertion (blue curve). [85]

Spike thermal processes were performed, characterized by quite fast heating ramps (50-170 °C /min, depending on the furnace set value) and rapid extraction after the maximum temperature was reached. Before each treatment, the furnace was heated at a value higher than the desired one (for instance 900 °C to perform a spike annealing at the maximum temperature of 760 °C) and then the sample was rapidly inserted, by means of a sample boat. In this way, the heating ramp is determined just by the time employed by Ge to heat, once inserted in a 900 °C environment. Then, when the desired temperature was reached (e.g. 760 °C), the sample was rapidly extracted from the tube and was allowed to cool down to 180 °C still in vacuum. A thermocouple recording one temperature value per second was wired to the sample boat, in order to measure the temperature reached by the sample. After cooling, the sample was definitely extracted from the vacuum environment and the SOD film was immediately removed with HF 10%, leaving the doped Ge sample ready for the characterizations. Fig. 3.5b reports two annealing ramps, the blue one is typical of a standard annealing with fast insertion, high temperature plateau and rapid extraction, while the red one is that of a spike annealing (no plateau, the sample is extracted as soon as the desired T is reached).

3.2 Characterization and results

Scanning Electron Microscopy (Tescan, Vega3 XM model) and Atomic Force Microscopy (DME, DS25 model in non-contact mode) were used to characterize Ge surface after the whole doping process had been carried out, allowing the analysis of lattice defects and modifications. A study of chemical properties of the source film has been also carried out through Fourier Transform Infrared Spectroscopy (FTIR)

(Jasco, FTIR660 plus), in order to better understand the dynamic of sol-gel condensation reactions under different curing conditions. To complete the optimization of parameters needed for a proper source curing, other experiments were carried out to verify SOD potentiality as a P-doping source. First, Secondary Ion Mass Spectrometry (SIMS) was done on diffused samples, by using a Cameca IMS-4f instrument with an O_2^+ beam, to characterize P diffusion profiles. Then, Rutherford Backscattering Spectrometry (RBS) was performed on SOD films after diffusion annealing, to derive their composition and estimate P-availability after different curing conditions. RBS was done at the 2 MV AN2000 VandeGraaff accelerator located at Legnaro National Laboratories, by using a 2 MeV He^+ particle beam. Finally, four-point probe electrical measurements were done on diffused Ge samples to measure P electrical activation. A four-point probe Hall system (MMR Technologies H-50) was used, characterized by a D/L ratio of 0.05 where D is the probe diameter and L is the sample side length.

3.2.1 Effects of environmental moisture on Ge surface in-processing

The effect of the relative humidity (RH) present in the glove box atmosphere during the source curing process has been investigated using different techniques. A first inspection was done with Scanning Electron Microscope on the surface of Ge doped samples, once the source film had already been removed. It revealed a Ge surface morphology strongly dependent on the environing conditions, as can be clearly seen from images in Fig. 3.6. These images were taken at the same magnification on samples cured at 130 °C for 15 min and annealed at the same temperature and time (685°C, 2 h). The surface appears as decorated by pits, with the typical pyramid shape of etched $\langle 100 \rangle$ oriented crystalline material. The density of etching pits (EPD) increases with the RH% value. In fact, the sample produced at the highest RH% condition displays a strongly hazed appearance also by naked eye, showing a very high density of pits whose depths have been evaluated by AFM analyses. In Fig. 3.6 (bottom right panel) the AFM scan image of the RH50% sample is reported, with a representative depth profile of two pits encountered on a $25\times25\mu$m area, showing depths in the order of several tens of nm. The clear correlation between EPD and humidity conditions can be ascribed to the influence of the atmosphere moisture content on the sol-gel condensation process.
The etching pits observed on samples cured at high humidity condition may be due to water vapour etching of Ge surface at high temperature, as previously observed

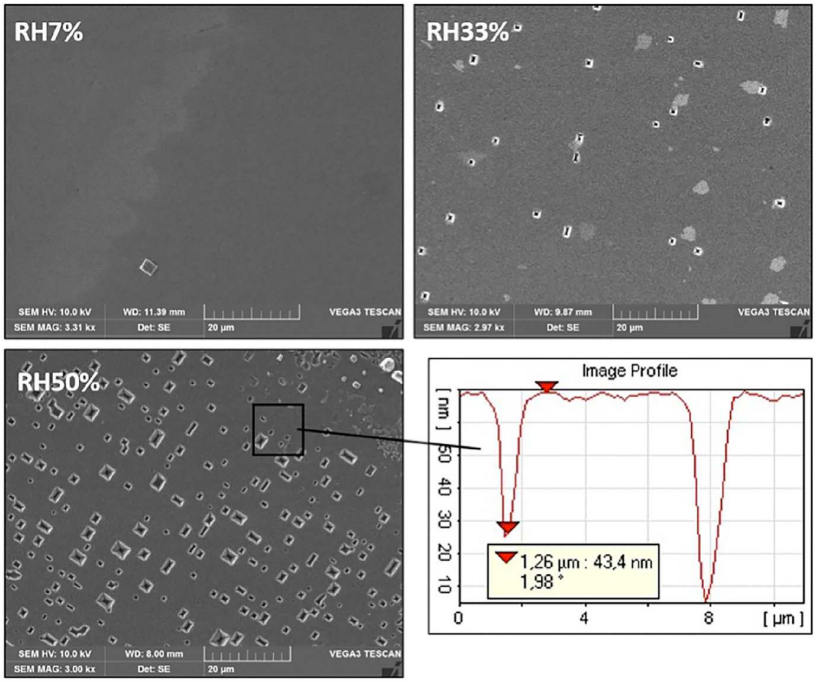

Figure 3.6. Etching pits on Ge surface after the same P diffusion treatment, but different source curing processes. SEM images (3000×) of samples produced at different humidity levels, as indicated by the labels. The right-bottom image is the depth profile of two adjacent pits as derived from an AFM scan (25×25µm) of the RH50% sample. [85]

by several authors [86,87]. The mechanism underlying the process can be described as follows: during curing, at the early stages of heating, water from continuing condensation is released from the SOD film and the network is compliant enough to allow easy permeation through porosities and escape from the surface. As the temperature increases above 400 °C, the network stiffens and shrinks, as a result of higher cross-linking degree and skeletal density. Residual water is still produced throughout the film thickness, as confirmed by literature [84], but the more compact, less porous structure hinders vapour release, thereby increasing water vapour pressure at a local level. At the Ge/film interface, the following oxidation reaction can take place:

$$Ge(s) + H_2O(g) \leftrightarrow GeO(g) + H_2(g). \tag{3.1}$$

The volatile germanium monoxide can evolve from the film, or be removed in the final etching step with diluted HF, after the diffusion process, leaving the characteristic etching pits. Hence, the lower condensation degree induced by the presence of high moisture levels during the curing step implies a higher concentration of pits, as observed in Fig. 3.6.

For what concerns the chemical composition of the P507 solution, it is expected from literature to contain a sol-gel precursor such as tetraalkoxysilanes of the type $Si(OR)_4$, though the substitution of one -OR with non-hydrolyzable functional groups, which could confer more elasticity to the starting sol-gel solution, is possible [88]. The P-containing compound added to the solution to achieve suitable P doping is proprietary, though literature data proved that the use of phosphoric or phosphonic acid and derivatives can be adopted without detrimental effects on the main structure of the glassy coating, meanwhile achieving the desired dopant composition [89, 90]. The sol-gel process is a quite complex ensemble of chemical equilibria, involving hydrolysis of the alkoxysilane in mild catalytic environment either alkaline or acidic within an alcoholic medium (reaction (3.2) below) and oligo/polymerization of the produced silanols through alcohol (3.3) or water (3.4) condensation, thus giving rise to a final solid network built up of Si-O-Si strong covalent bonds.

$$\equiv Si - OR + H_2O \longleftrightarrow \equiv Si - OH + ROH \tag{3.2}$$

$$\equiv Si - OR + \equiv Si - OH \longleftrightarrow \equiv Si - O - Si \equiv + ROH \tag{3.3}$$

$$\equiv Si - OH + \equiv Si - OH \longleftrightarrow \equiv Si - O - Si \equiv + H_2O \tag{3.4}$$

Most common reaction conditions make use of ethanol as solvent. The whole sol-gel reticulation process has been extensively studied and characterized from a long time. Several factors have been found to adversely affect both hydrolysis and condensation, whose outcome and rates are mutually connected [84,91,92]. In general, the above-indicated reactions occur simultaneously, though a specific set of parameters may be chosen to favor the full hydrolysis before condensation takes place. The reverse reactions are also possible: the reverse of reaction (3.2) may occur if the volatile alcohol species is prevented from evaporation. De-polymerization, leading to Si-O-Si bridges leakage, is the reverse of both (3.3) and (3.4) reactions and can be promoted indeed in the presence of excessive amount of humidity in the environment. In this case, the equilibrium described in reaction (3.4) can be altered and shifted towards the reactants, thus leading to a lower degree of cross-linking in the final network, with low molecular weight siloxane units, either chains or rings, and higher content of uncondensed Si-OH groups. Moreover, when the dried gel (xerogel) undergoes annealing in the furnace at high temperature, the condensation reaction can proceed, with water evolution up to 700 °C [84] and this could form GeO (as explained above in reaction (3.1)). Further indirect confirmation of this proposed mechanism for the formation of corrosion pits can be found by observing a

sample where Ga250 solution, instead of P507, was deposited. It is worth to report that the gelling time of the Ga250 precursor solution is remarkably lower than P507 and a highly viscous gel is formed in case of Ga250 after 6 months from the production date, while P507 is still in a liquid form after the same time. This results in a higher degree of cross-linking before the annealing step. In this case, during high temperature annealing, further release of water as a by-product of proceeding condensation is still possible but in a lower amount and less etching pits should form. SEM pictures reported in Fig. 3.7 support this assumption. The SOD coating from

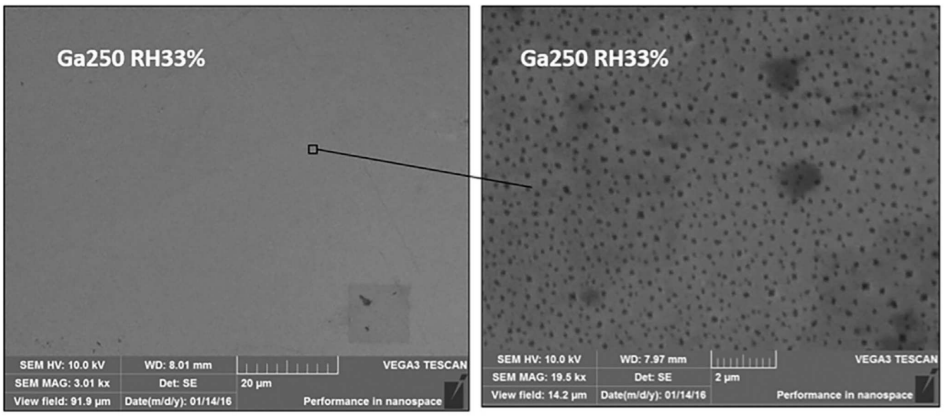

Figure 3.7. Etching pits on Ge surface after Ga diffusion treatment. SEM images (3000times and 20000×) of a sample cured in humidity conditions of 33%, after Ga diffusion at high temperature (720 °C, 18 min). [85]

Ga250 has been deposited at intermediate level of humidity (33%) and cured at 130 °C for 15 min, then annealed at 720 °C for18 min. At 3000× magnification, the sample apparently does not show any visible pit from surface corrosion. However, by increasing the magnification up to 20000×, a huge number of small, square shaped pits can be observed, thus demonstrating that also in the case of Ga250 the corrosion action of water vapour on Ge surface is present, though limited by the higher degree of condensation and network compaction obtained prior to annealing.
The presence of pits can induce severe inhomogeneity in the dopant distribution, either across the surface or in depth, thus hindering the formation of a regular and sharp p-n junction over the whole thickness and surface. We believe that humidity plays also a role in changing the expansion coefficient of the dried gel. In fact, samples cured at high humidity conditions undergo also cracking of the SOD film during the thermal annealing in furnace, as shown in the optical image in Fig. 3.8a. The same phenomenon may also occur under low humidity conditions if the film thickness is too high. In the last case, once removed the film, cracks of irregular shape were visible also on the underlying Ge surface (Fig. 3.8b).

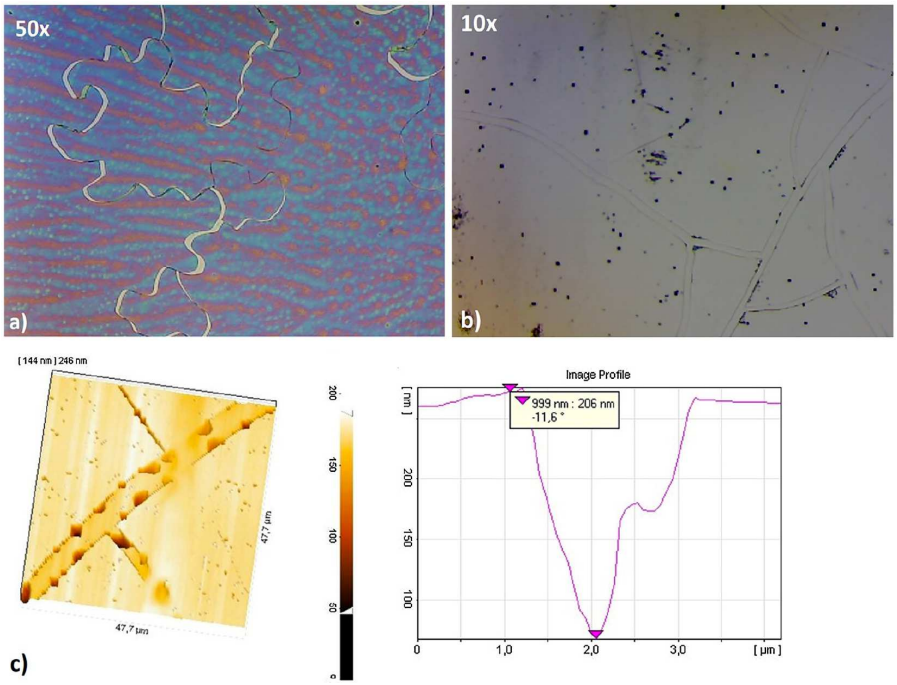

Figure 3.8. Optical microscope and AFM images of a sample coated with P507 solution, cured at high humidity conditions (>30%) and annealed in furnace. Not only the source film but also the underlying Ge surface are highly damaged. (a) Cracks in the cured film. (b) Cracks on Ge surface, visible after film removal. (c) AFM image of Ge surface: cracks full of etching pits about 200 nm deep. [85]

Ge cracks were analysed with AFM and they appeared as a corroded zone full of deep etching pits (Fig. 3.8c). The corrosion can be attributed to a combined action of moisture, which leaks out from SOD rifts and forms GeO, and HF chemical etching performed after annealing for film removal. SOD cracking is not detected in samples cured at low moisture levels (less than 30%). This implies that to prevent cracking there is no need to perform thermal diffusion in two steps, a slow ramp until 450 °C followed by a faster one to reach the peak temperature, as reported in the literature [81]. Indeed, it is sufficient to cure the gel at low humidity conditions, in particular below 10%, in order to avoid the formation of both cracks and etching pits during the subsequent annealing stage.

3.2.2 Curing time and temperature

Effect of curing time and temperature on the condensation degree

The presence of residual silanol groups in the xerogel should be minimized, in order to prevent excessive water release from condensation during the annealing/diffusion step at high temperature. With the aim of optimizing the curing

conditions, in order to achieve a dried gel bearing the lowest amount of unreacted silanols, an FTIR study has been performed. The samples were coated with P507 solution and cured at 130 °C for different times or at 200 °C. FTIR spectra of Fig. 3.9 have been collected in transmittance mode, by using a clean Ge substrate as a background and exploiting the moderate transmittance of Ge itself in the range 4000-550 cm^{-1}. After Y-axis conversion into absorbance, a normalization has been applied by dividing all the absorbance values in each spectrum by the largest absorbance value, corresponding to the wavelength of about 1080 cm^{-1} in the present case. The typical features of sol-gel derived silica xerogels are clearly evident at about 1200 and 1080 cm^{-1}, ascribed to asymmetric Si-O-Si stretching LO and TO modes respectively [93,94]. Other signals are visible at 800 cm^{-1} (TO symmetric stretching mode),

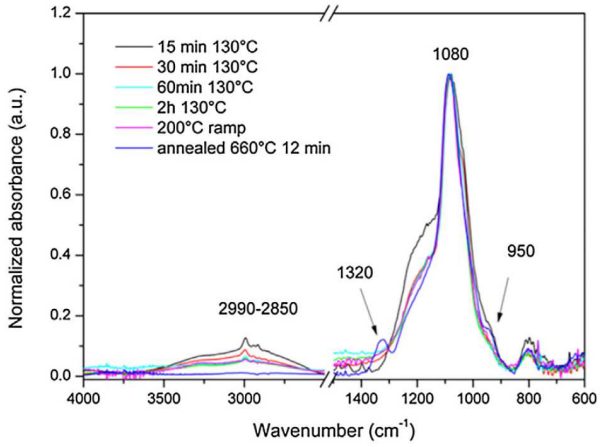

Figure 3.9. Normalized FTIR absorption spectra of P507 coatings, cured for different time and temperatures. The blue spectrum is obtained from a sample cured at 130 °C for 30 min, that has been also annealed in furnace at 660 °C for 12 min. [85]

2990-2850 cm^{-1} (C-H stretching modes of residual ethanol groups), 950 cm^{-1} Si-OH stretching modes overlapped with $Si\text{-}O^{-}$ dangling bonds, where non-bridging oxygen atoms are indicative of a less interconnected, weakly branched structure. More in detail, the intensity of the shoulder at 1200 cm^{-1} has been directly correlated with the porosity and humidity of the gel, as deeply investigated by several authors [94–97]. As the thermal treatment time increases, the shoulder contribution at 1200 cm^{-1} and at 950 cm^{-1} decreases accordingly, thus pointing to a progress in condensation that implies a reduced amount of silanols and Si-OR. It is worth to note that a treatment time as long as 30 min leads to an almost stable network structure with negligible changes even after prolonged treatment times, up to 2 h, or higher temperature (200 °C). The presence of alkyl residual groups from entrapped ethanol or

from unhydrolyzed Si-OR groups is still visible after heat treatment at 200 °C, as can be deduced from the weak C-H stretching signals. This is in agreement with literature data, stating that a complete removal of organics occurs for temperatures higher than 400 °C [84]. After annealing at 660 °C for 12 min of the sample cured 30 min at 130 °C, full condensation is achieved, as shown by the spectrum in Fig. 3.9. The completion of condensation and network compaction towards a densified silica structure is proven by the disappearance of peaks from C-H stretching around 2850-2990 cm^{-1} and the shoulder at 1200 cm^{-1}, ascribed to Si-OH and Si-OR groups. On the other hand, the shoulder positioned at about 950 cm^{-1} is still visible but in this sample its assignment is not unambiguous. In fact, this signal can be due to the presence of a remarkable amount of residual non-bridging oxygen atoms, as previously observed in literature [94], though it can be also assigned to the phosphate group (PO_4^{3-} symmetric stretching mode) [97]. Interestingly, the annealed SOD coating from P507 solution displays a new, clearly visible peak at about 1320 cm^{-1}, ascribed to the P=O stretching mode and in agreement with literature [98,99].

Effect of curing time and temperature on electrical properties of post-annealing P-doped Ge

Chemical P depth profiles have been measured through Secondary Ion Mass Spectrometry (SIMS). Samples that underwent the same spike annealing (up to 660 °C in 12 min) but different curing processes on the SOD film are shown in Fig. 3.10a. In the case of the curing process at 130 °C for 15 min, which led to an incomplete condensation of SOD as shown from FTIR analysis, the corresponding diffusion profile (Fig. 3.10a green curve) has reached a lower doping level than best cases and is not box-like implying inhomogeneity in dopant distribution. Thus, in this case the 15 min cured film has turned out to be a bad doping source. On the other hand, samples whose xerogel achieved an advanced state of condensation, i.e. heating at 130 °C for 30 or 60 min or up to 200 °C, present an optimal box-like diffusion profile characterized by high doping level (4-5 $\times$ 10^{19} cm^{-3}) and good homogeneity (Fig. 3.10a blue, black and red curves). While IR spectra showed negligible differences in the main features as curing time is increased from 30 min up to 2 h, the sample cured at 130 °C for 2 h and spike annealed is characterized by a low and inhomogeneous diffusion profile (Fig. 3.10a light blue curve). This evidence could be related to the release of phosphorous during the curing stage, prior to annealing. The compound added as a dopant source to the sol-gel precursor solution is not known, as mentioned before. However, taking into account the long gelling time of the precursor solution and its homogeneity after spinning, with no evident

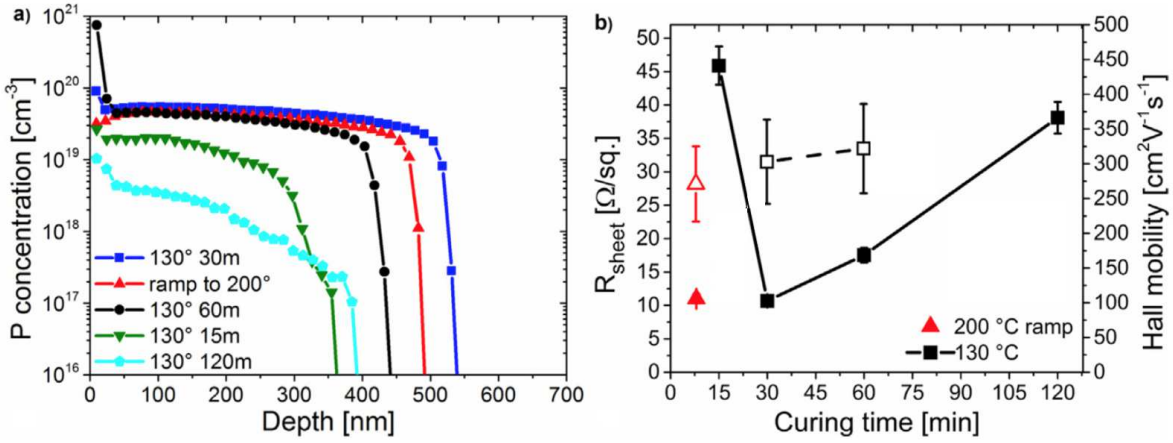

Figure 3.10. Post-diffusion characterization of samples coated with P507 and cured at different conditions. a) SIMS chemical concentration profiles of P diffused in Ge. 15 and 120 min curing times present the worse diffusion profile. b) Sheet resistance (left scale, full symbols) and mobility (right scale, empty symbols) as functions of curing time. [85]

phase separation, the use of phosphate esters as dopant sources can be envisaged [100]. In the literature, silicophosphate glasses have been synthesized starting from different precursors, such as orthophosphoric acid, phosphoric anhydride, phosphate esters and phosphite esters [89, 100]. Nevertheless, irrespectively of the phosphorus-containing precursor, the loss of P during thermal treatment has been observed and extensively studied by using different techniques [97, 101]. Therefore, the drop of P content detected in the sample treated for 2 h at 130 °C is not surprising and is expected to lead to non-homogenous or insufficient doping of the Ge substrate. The same argumentation can explain the poor doping capacity of the film cured for only 15 min: because of the incomplete polymerization achieved during the curing stage, the film undergoes a strong P-compound evaporation during the high temperature diffusion treatment in furnace.

Aiming at a further confirmation of these hypotheses, a post-annealing Rutherford Backscattering Spectrometry (RBS) experiment was carried out on three P507 glassy films, annealed at 660 °C for 12 min but cured at 130 °C for different times: 15, 30 and 120 min. In Table 3.2 the atomic percentage composition of SOD films is reported together with the total dose, which is the density of atoms, in the layer of interest, per unit area.

By comparing the results, a difference in P concentration is observed: films cured for short and long times (15 and 120 min) are characterized by less P atoms than the one cured for 30 min. This confirms the idea that too long and too short curing times can induce P compound evaporation, reducing the amount of available

Table 3.2. RBS analysis of SOD films annealed at 660 °C for 12 min but previously cured at 130 °C for different times. The total atom dose and percentage atomic compositions are reported.

Curing time (min)	Total dose (cm^{-2})	%Si	%O	%P	%Ge
15	$(1.40\pm0.05)\times10^{18}$	20±1	68±2	7±2	4.7±0.5
30	$(1.20\pm0.05)\times10^{18}$	21±1	64±2	11±2	4.3±0.5
120	$(1.30\pm0.05)\times10^{18}$	18±1	68±2	6±2	5.0±0.5

dopant in the SOD source. RBS analysis shows also the presence of about 4.5% Ge concentration in all films, meaning that during high temperature annealing some Ge atoms out-diffuse from the surface and enter the SOD film. The total amount of lost atoms corresponds to a Ge layer of about 10 nm. Ioannou et al. demonstrated that an effective capping layer made of SiO_2 or Si_3N_4 completely prevents Ge substrate loss during low temperature annealings, while the absence of any capping would produce a remarkable Ge loss of about 600 nm for a treatment at 660 °C for 12 min (extrapolated datum) [9, 102]. Therefore the SOD source film can be considered as a capping layer of fairly good quality. This fact should be carefully considered when applying these methods to the production of shallow junctions.

Four-point probe electrical measurements were performed on the same samples to verify the electrical activation of diffused phosphorus atoms under different curing conditions of the xerogel source. Measurements have been carried out in air, at room temperature, by directly touching Ge surface with point probes without any metallic pads. In Fig. 3.10b the values of sheet resistance and mobility corresponding to each curing process tested are reported. As regarding the 130 °C curing, the lowest R_{sheet} values of 10.7 and 17.5 Ω/sq correspond to processes that last, respectively, 30 and 60 min. The sample cured up to 200 °C with a ramp of 18 °C/min shows an optimum R_{sheet} as well (11 Ω/sq). These three samples are also characterized by compatible mobilities, with an average value of about 300 cm^2/Vs. Contrariwise, curing processes at 130 °C, for either 15 or 120 min, lead to higher sheet resistance values indicative of low active carrier density. Besides, in these last two samples Hall-effect measurements were inaccurate with large difference of Hall voltage when current flows along the two diagonals of the square sample. This is interpreted as a further confirmation of doping inhomogeneity, resulting from inappropriate SOD preparation conditions.

These data are in agreement with SIMS profiles. In particular, a good matching between Hall and SIMS dose within the error bars is found in samples cured at 130 °C for 30 min and up to 200 °C (see Table 3.3).

Table 3.3. Comparison between SIMS chemical dose and Hall active dose for homogeneously doped samples (those with low sheet resistance).

Curing T (°C)	Curing time (min)	SIMS dose (cm^{-2})	Hall dose (cm^{-2})
130	30	2.2×10^{15}	1.9×10^{15}
130	60	1.5×10^{15}	1.1×10^{15}
200 ramp	8	1.7×10^{15}	2.1×10^{15}

3.2.3 P spin-on doping at different temperatures

In the previous paragraph it was shown that parameters such as curing humidity and curing time affect the surface morphology, the degree of reticulation reached by the source film and the amount of dopant available for diffusion. Once optimized these parameters and found the best curing procedure, it was necessary to study phosphorus diffusion by performing spike-annealing treatments at different temperatures. Referring to applications such as photovoltaic or radiation detectors, the goal is to obtain a homogeneous doped layer of thickness about tens or hundreds nanometers, with a high doping level 10^{19} cm^{-3} and totally electrically active.
Hence, four Ge p-type substrates were covered with a P507 film and cured at the best conditions: three of them at 130 °C 30 min and one with the ramp to 200 °C. All of them at 10% of relative humidity. Then, they were spike-annealed at 607 °C, 663 °C, 666 °C (the one cured up to 200 °C) and 760 °C, for about 12 minutes between insertion and extraction. After the film removal, diffusion profiles and electrical properties have been measured.
In Fig. 3.11a P diffusion profiles measured through SIMS are reported. All samples show a box-like concentration profile, as it was expected for carrier concentrations higher than the intrinsic one, in agreement with Brotzmann's model (paragraph 1.2.4). This also means that the layers are all homogeneously doped. It should be noted that the maximum concentration and the depth of these profiles increase with increasing the annealing temperature, thus passing from 600 °C to about 660 °C. At 760 °C, the depth increases further while the maximum concentration keeps constant and moves from the surface to the central part of the profile. In this sample (black curve in Fig. 3.11a), the low concentration at the surface is due to P out-diffusion from Ge following to an emptying of the source. In order to verify the electrical activation of P atoms diffused inside Ge samples, four-point probe electrical measurements were done. In Fig. 3.11b a plot of sheet resistance and mobility as

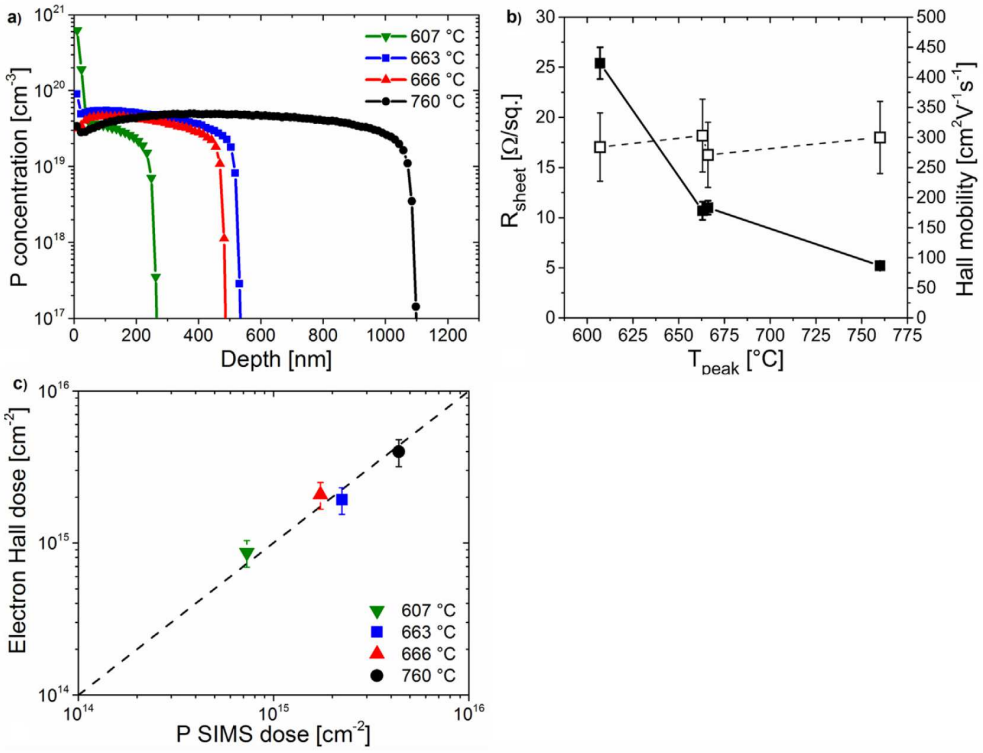

Figure 3.11. Post-diffusion characterization of samples coated with P507 and spike-annealed at different temperatures. a) SIMS chemical concentration profiles of P diffused in Ge. b) Sheet resistance (left axis, full symbols) and mobility (right axis, empty symbols) of P-doped layers as functions of spike annealing temperature. c) A comparison between the Hall and SIMS doses: P atoms result totally electrically active for all the tested annealing temperatures. [85]

functions of spike annealing temperature is reported. The sheet resistance decreases with increasing the layer thickness: for instance, sample 760 °C doping profile has a depth that is about twice thicker than that of sample 663 °C (Fig. 3.11a) and a sheet resistance that is about a half. This means that the doped layers, even if treated with different thermal annealings, keep a similar resistivity. Fig. 3.11c reports a comparison between the Hall dose and the SIMS one: all points stay on the equality line within the error bars. This means that all samples show a complete electrical activation of P atoms. The annealing temperature does not seem to affect the degree of activation. The same result emerges from the joint analysis of sheet resistances and SIMS profiles (method described in paragraph 2.4.4): for all temperatures, the sheet resistance experimental values are compatible with those calculated by starting from a completely active diffusion profile.

These data perfectly support the conclusion that under proper preparation conditions of the source film, fully active doped layers can be obtained on relatively large

areas, by spin-on-doping technique.

3.2.4 Analysis of diffusion activation energy

By starting from diffusion profiles plotted in Fig. 3.11, diffusion lengths were evaluated as the profile depth at half maximum. Then, a very simple model has been conceived to describe the dependence of dopant diffusion length L on the thermal budget applied during the annealing treatment. First, a standard Arrhenius relation is assumed between the diffusion coefficient and temperature (Eq. 3.5), being E_{act}^{P} the activation energy of P diffusion. Then, the dependence on time is introduced with Eq. (3.6).

$$D = D_0\, exp\left(-\frac{E_{act}^{P}}{k_B T}\right) \tag{3.5}$$

$$L^2 = D \cdot t \tag{3.6}$$

Equations (3.5) and (3.6) are merged into Eq. (3.7) that describes the square of the diffusion length as a function of temperature and time.

$$L^2 = D_0\, exp\left(-\frac{E_{act}^{P}}{k_B T}\right) t \tag{3.7}$$

If the temperature T varies during the process, i.e. it is a function of time (as it happens in our spike treatments) Eq. 3.7 can be directly generalized as follows:

$$L^2 = D_0 \int exp\left(-\frac{E_{act}^{P}}{k_B T(t)}\right) dt. \tag{3.8}$$

The last integral is defined as the *thermal budget* (TB) of the annealing treatment. By applying the natural logarithm to the equation, we achieve a linear relation:

$$ln(L^2) = ln(D_0) + ln(TB). \tag{3.9}$$

All thermal budgets (so integrals like that of Eq. 3.8) were calculated using a set of different values for the activation energy E_{act}^{P}, in the range (2.1-2.7 eV). Diffusion length is deduced by the experimental profiles as the length at which the concentration reduces by a factor 2 with respect to the maximum concentration. Then, *ln(L^2)* was plotted as function of *ln(TB)*, doing a plot for each value of activation energy. All groups of data were fitted through a linear function with slope fixed to 1. In Fig. 3.12a, we compared the mean square deviation (MSD) of data from each fitting. The best fit was obtained for an activation energy E_{act} = (2.4$\pm$0.1) eV, with a MSD of

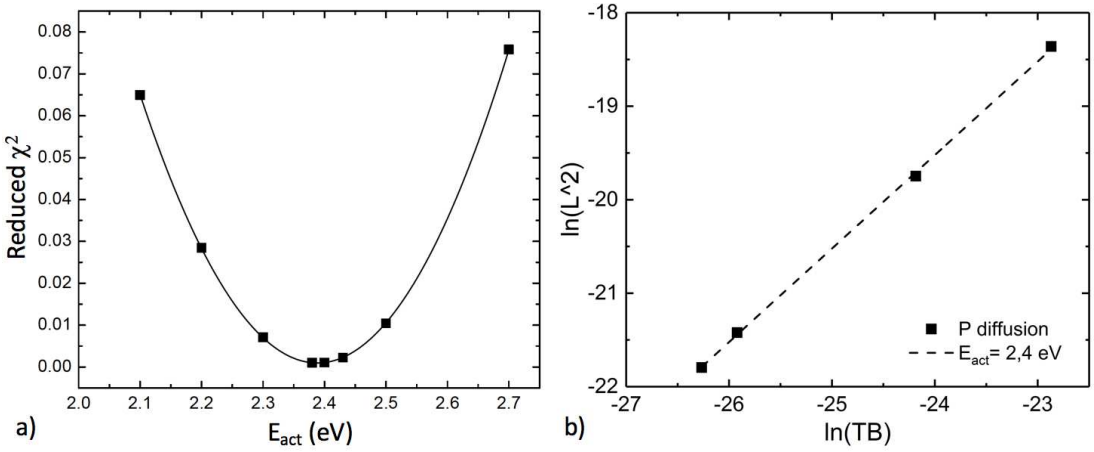

Figure 3.12. P diffusion analysis. a) mean square deviation (MSD) of data from each fitting are reported as function of the correspondent activation energy. b) All data and the best fit, obtained for E_{act} = 2.4 eV.

0.001. From the resulting intercept we obtained D_0 = 113.7 cm^{2}s^{-1}.
In Fig. 3.12b all data and the best fit are reported. By comparing the obtained value of activation energy for P diffusion (2.4 eV) with that obtained by Brotzmann (2.85 eV, see paragraph 1.2.4), we should take into account that Brotzmann's value is the activation energy of the intrinsic diffusion coefficient. The diffusivity of our sample is connected to the intrinsic diffusivity by formula 1.18 therefore, in order to be quantitatively compared with our result, the activation energy of 2.85 should be corrected for the temperature dependence of n and n_{in}. Another reason why the comparison can be just qualitative is that our samples were annealed with spike treatments, thus their average temperature should be considered lower than the maximum temperature of the spike. In conclusion, we can say that the result we obtained for the activation energy of P diffusion is in acceptable agreement with the literature.

3.3 Conclusions

A detailed procedure for the successful application of SOD sources to Ge has been reported. Homogeneously doped n-type layers showing a full electrical activation of the dopant have been obtained. Despite the simplicity of this method, some working parameters have proved to be crucial for achieving a continuous, homogeneous and highly doped junction, such as the thickness of the source film, the relative humidity and the duration of the curing process. SOD spinning recipe has been optimized to obtain a film of homogeneous thickness (∼230 nm), in order to avoid

mechanical stresses and inhomogeneous doping.
The role of the environmental relative humidity (RH) present during the SOD curing stage has been understood: if it is higher than 10%, it can reverse the condensation reaction in the sol-gel process leading to an incomplete polymerization. Besides, the incorporated water vapour can be released during high temperature annealing and act as an etchant, thus forming a high density of etching pits on Ge surface. Once operating at low RH conditions, the duration of SOD curing process turned out to be a key parameter that needs to be optimized, looking for a compromise between two concurrent phenomena: polymer condensation and dopant-compound evaporation. These two phenomena were monitored through FTIR and RBS analyses. If the curing time is too short, then the sol-gel condensation reaction does not arrive to completion and a stable incorporation of dopant atoms in polymer chains cannot be achieved; then, when condensation is rapidly proceeding during the subsequent high temperature annealing, dopant-compound evaporation is enhanced. Otherwise, if the curing time is too long, polymer chains condensation is completely carried out but simultaneously dopant-compound evaporation is advancing. The relation between the curing time and the amount of dopant in SOD available for diffusion was also verified through SIMS profiling and Van der Pauw electrical measurements. We found out that an intermediate curing time ranging from 30 min to 1 h, at 130 °C, is suitable to obtain a highly doped and fully active layer.
Ge loss from the surface corresponding to a 10 nm thick layer and due to diffusion into the overlying SOD film, was highlighted by RBS analysis. This phenomenon, could be problematic when dealing with shallow junction formation by spin-on-doping.
By operating at the optimized conditions, several temperatures for dopant diffusion treatments were tested and the obtained layers characterized. The annealing temperature did not seem to affect the homogeneity and degree of activation of doped layers. An analysis of diffusion profiles has been performed, in order to calculate the activation energy of P extrinsic diffusion. A value of 2.4 eV in reasonable agreement with the literature has been obtained.
After a proper tuning of process parameters, spin-on-doping has turned out to be a simple and cost-effective technique that allows fabricating large doped areas on Ge. In particular, the realized junction displays thickness and doping levels in principle suitable for minority carrier blocking action in high purity germanium gamma ray detectors. In the appendix, a p-n junction created in HPGe with the technique of P spin-on diffusion is characterized.

Chapter 4

Sb doping from sputtered sources

The production of a highly doped shallow layer in germanium, without introducing lattice defects and thus allowing a total electrical activation of the dopant, is really a complex challenge. This is even more when dealing with high purity Ge, because the doping process should be carried out without introducing impurities in the bulk. The first doping technique that we have optimized on Ge to achieve a full electrical activation, i.e. phosphorus spin-on-doping, retains the unknown of the degree of purity of the P source. Indeed we buy a commercial P-containing sol-gel precursor, whose components are not known. Among all contaminants, copper should be avoided as much as possible, because it is commonly found in traces in all environments and it diffuses very rapidly in Ge, also at low temperature.
For these reasons, with the purpose of identifying a suitable doping process for the formation of the n contact on HPGe, in parallel to spin-on-doping we developed other techniques starting from sources with a known degree of purity. This kind of sources consisted in antimony thin films, of variable thickness from 1 to 100 nm, produced by sputtering from a high-pureness Sb target ($\leq$0.01 ppm of Cu content). To make an example, the Cu content of a 20 nm Sb film deposited on a small sample of 1 cm^2 area and 2 mm thickness, could contaminate the bulk to a concentration of about 3x10^9 cm^{-3}. Instead, if the 20 nm Sb film was deposited on a standard cylindrical detector of radius 3 cm and height 7 cm, the bulk contamination would be about 1x10^8 cm^{-3}. This calculation was done by assuming the Sb film to be metallic and by using the Sb density reported in the literature, thus it has just a qualitative meaning.
For the doping, three approaches were adopted:

- Sb diffusion in furnace, from a thin film sputtered on Ge surface;
- Sb diffusion in furnace, from a thin film sputtered on a remote Si surface;

- Sb diffusion via laser thermal annealing on a ultra-thin film sputtered on Ge.

Laser thermal annealing (LTA) is a doping technique that uses laser irradiation to melt a very thin layer of semiconductor, thus inducing dopant diffusivity in liquid. It was described in paragraph 1.2.5.
To characterize the samples, the surface morphology was specifically investigated by electron (SEM-EDS) and atomic (AFM) microscopy. Diffusion profiles were characterized by Secondary Ion Mass Spectrometry (SIMS). For the third applied technique, laser thermal annealing of sputtered Sb, the electrical activation was estimated through four-point probe electrical measurements.

4.1 Experimental

A p-type (100) Ge wafer (resistivity [0.04-0.4] Ω·cm) and a p-type high purity germanium wafer (impurity density $< 2\text{x}10^{10}$ cm^{-3}), both supplied by Umicore, were cut into 1x2 cm^2 and 1x1 cm^2 area samples. Each sample was cleaned with hot 2-propanol, hot deionized (DI) water and HF 10% to remove dicing adhesive residue and native oxides. Cleaned substrates were put in the sputtering equipment consisted of a stainless steel vacuum chamber evacuated by a turbomolecular pump to a base pressure lower than $1\text{x}10^{-4}$ Pa. The glow discharge sustaining device was a 2 inches cylindrical magnetron sputtering source connected to a radio frequency power generator (600 W, 13.56 MHz), through a matching box. The deposition parameters used to form all Sb films were: direct RF power 30 W; target-to-substrate distance 14 cm; working gas Ar (99.9999% purity); Ar flow 20 sccm. A mass flow controller regulated the working gas flow and the chamber was continuously pumped during the deposition in order to reduce atmosphere contamination by wall outgassing. Pure Sb target (99.999% pureness, with an assessed Cu concentration of 0.01 ppm) supplied by ACI Alloys was used. Sb deposition rate, as determined by RBS, was 13.3 nm min^{-1} (i.e. $3.76\text{x}10^{16}$ at cm^{-2} min^{-1} with a Sb density of $3.27\text{x}10^{22}$ at cm^{-3}). The duration of each deposition run was varied in order to achieve different film thickness in the range (1-100 nm).

4.1.1 Sb diffusion from sputtered sources in furnace

Fig. 4.1 illustrates the configuration adopted for the Sb diffusion treatments with a direct source. An Sb thin film, 100 nm thick, was sputtered above Ge surface, then the sample was capped with a piece of Si wafer to limit Sb sublimation from the

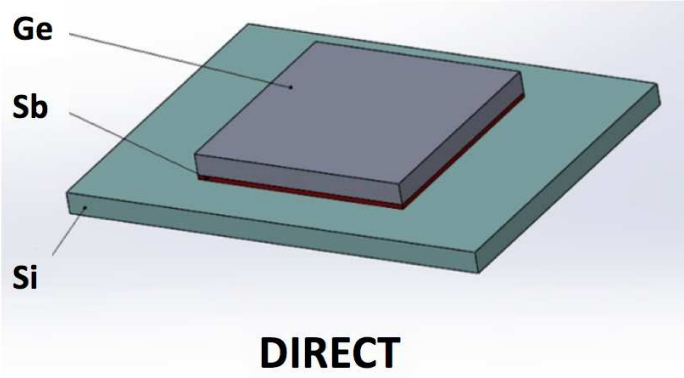

Figure 4.1. In the direct-source method, an Sb thin film is directly sputtered on Ge surface. During the thermal annealing a piece of Si wafer is used as a capping in order to avoid Sb out-diffusion from the source.

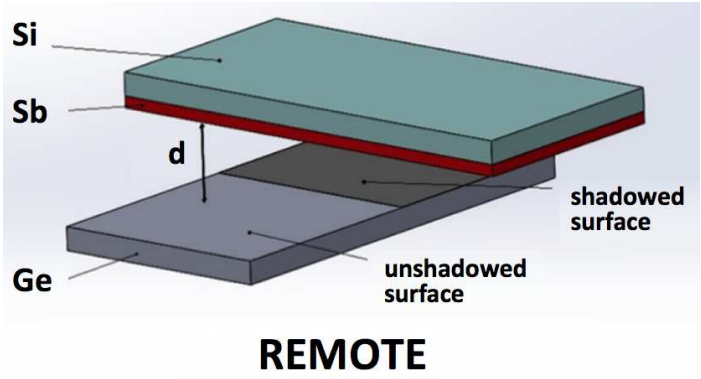

Figure 4.2. In the remote-source method, an Sb thin film is sputtered on a piece of Si wafer. During thermal annealing, the Sb/Si remote source is put over Ge and kept at a fixed distance d, with the Sb side turned down.

film and promote its diffusion inside Ge, during the high temperature annealing. The whole was clamped between two quartz slides and inserted into a standard tube chamber furnace for the annealing. Fig. 4.2 instead describes the method used for the diffusion from a remote source. An Sb thin film, 100 nm thick, was sputtered above a clean piece of Si wafer to form the remote source. Then, a Ge sample of rectangular shape (1x2 cm^2 area) was put inside the sample boat and the Sb-coated silicon was placed over Ge, with the Sb thin film turned down toward germanium. The two were kept at a fixed distance *d* with the help of two spacers, since this is a remote deposition. As indicated in the schematic, the Ge surface exactly below the Sb source was named *shadowed surface*. Sb diffusion was performed in a standard tubular furnace equipped with a quartz tube, under constant nitrogen flow (about 400 sccm). The latter was established after five vacuum/gas cleaning cycles, aimed at removing contaminants from the furnace as was done for SOD annealing. Thermal treatments characterized by quite fast heating ramps (∼50 °C/min depending

on the furnace set value) were performed according to the following procedure. The furnace was previously heated at a value higher than the desired one (for instance 670 °C to perform a treatment at 610 °C) and then the sample was rapidly inserted, by means of a sample boat. After generally 16 minutes, the sample reached the desired temperature but it was left inside some other minutes. When 30 minutes had passed since the sample was inserted, it was rapidly extracted from the tube and left to cool down to room temperature. A thermocouple, recording one temperature value per second, was wired to the sample boat in order to measure heating and cooling ramps. Several treatments were done, at temperatures close to and higher than the Sb melting temperature: 570 °C, 615 °C, 630 °C, 700 °C, 740 °C, 790 °C.

4.1.2 Sb diffusion from sputtered source by LTA

LTA is a forefront doping technique, very attractive because it allows to reach doping levels over the solid solubility. An introduction to this technique can be found in paragraph 1.2.5.
A circular Sb ultra-thin film of 2 nm thickness and 5 mm diameter was sputtered, with a deposition time of 9 s, in the center of the surface of an HPGe sample (1x1 cm^2 area), with the aid of a Kapton mask (see Fig. 4.3). All laser treatments have

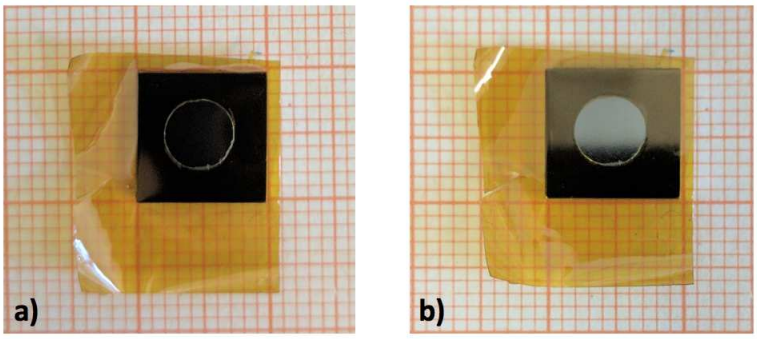

Figure 4.3. HPGe square sample prepared for LTA. a) Kapton mask created to leave only a circular surface portion exposed. b) Circular Sb ultra-thin film done by sputtering.

been performed at INFN-LNL (National Institute of Nuclear Physics - Legnaro National Laboratories) using a pulsed Nd:YAG solid state laser belonging to the SPES Target Ion Source Group. The laser emits in the infrared (1064 nm), but due to low Ge absorption at that wavelength, a third harmonic generator is usually adopted in order to bring the laser wavelength in the UV range (355 nm). The pulse duration is 7 ns and the repetition rate 10 Hz (sufficiently low not to overlap the time effects of subsequent pulses).

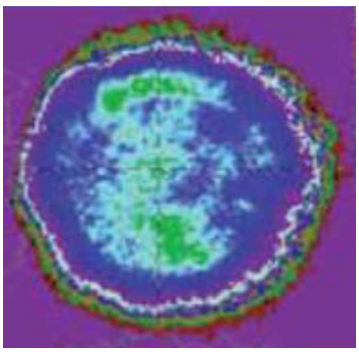

Figure 4.4. Near field spatial energy profile of the laser beam. It is Gaussian, with a flat high-intensity central zone.

The laser spot is circular with a diameter of 7 mm, the spatial energy profile of the laser is nearly Gaussian with a flat central zone and low-intensity tails, as can be seen in Fig. 4.4 provided by the producer and reporting the near field spatial energy profile. The setup for laser annealing is quite simple and it is shown in Fig. 4.5. First, the sample was fixed on a microscope slide and then the slide was mounted on a movable holder.

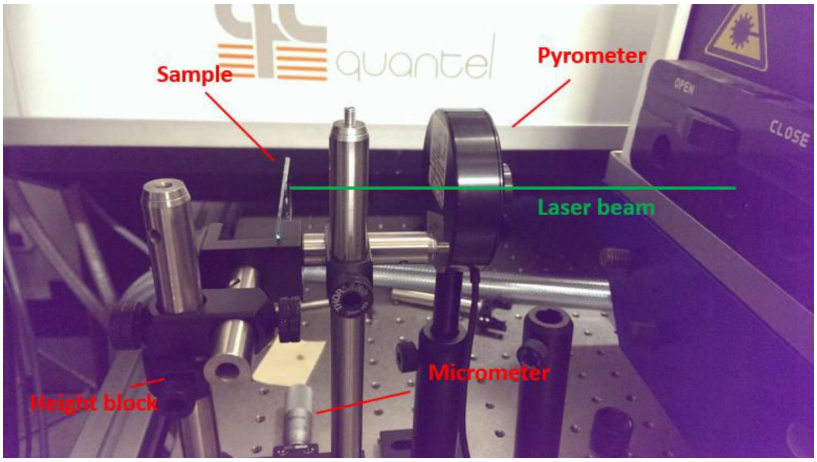

Figure 4.5. Setup for laser thermal annealing. The sample is fixed on a microscope slide movable with the aid of a micrometer. Before doing each treatment, the laser power stability is controlled through a pyrometer.

The height and tilt of the slide can be manually regulated in order to position the sample perpendicularly to the beam. A micrometer allowed to finely move the sample in order to fit many laser spots on the same Ge strip. A circular diaphragm of 6.5 mm was put between the laser source and the sample, in order to cut the external non-uniform part of the spot. Since the laser needs to warm up in order to reach a stable output, a pyrometer was used to monitor the incident power. Once the beam

stabilized, we measured the incident power P_L and then removed the pyrometer. At that point, the annealing treatment could be done by using just 1 pulse.
An important parameter is the energy density that is deposited on the sample during a single pulse treatment. It was calculated through Eq. (4.1), where P_L = *1000 mW* was measured through the pyrometer and the laser frequency is known *f = 10 Hz*.

$$E_L = \frac{P_L}{f \cdot A_{spot}} = 300\ mJ\,cm^{-2} \tag{4.1}$$

4.2 Results and discussion

4.2.1 Sb diffusion in furnace from direct source

For what concerns samples with Sb source directly sputtered on the surface, different annealing treatments were done in furnace at the temperatures of 570 °C, 610 °C and 630 °C. As first analysis, we performed the characterization of pre- and post-annealed surfaces, through SEM and AFM imaging. In Fig. 4.6a there is a SEM image of the as-deposited Sb thin film. It looks homogeneous and it is characterized by a low roughness ($<$ 5 nm), as measured by AFM on a 50x50 μm^2 area. On the contrary, SEM images on post-annealed surfaces (Fig. 4.6b to d) revealed a substantial change of the surface morphology, consisting in the appearance of grain-like structures with lateral sizes in the order of micrometers. These structures were distributed on the whole sample surface and they were also found on the surface of the capping Si. Some interesting differences were observed between the sample treated at 570 °C and those treated at 610 °C and 630 °C. The first difference was in the shape of the structures, which was characterized by sharp edges in the former sample (several structures are hexagonally-shaped) and by more irregular shapes and rounded edges in the latter two. Moreover, in the latter samples the presence of holes on the Ge surface was clearly visible (look at the inset in Fig. 4.6c). AFM measurements showed that the depth of these holes ranges from 50 to 200 nm.
The average size of the structures together with their average distance decreases with increasing the annealing temperature, thus implying that nucleation process is promoted at the expense of the growth one, i.e. many nucleation sites for the growth of small grains. Grain composition was analyzed through Energy Dispersive Spectrometry (EDS), showing that they predominantly consist of Sb but also of Ge, whereas on the sample surface in between the grains the Sb amount drastically decreases below the detection threshold. The average Sb/Ge atomic ratio

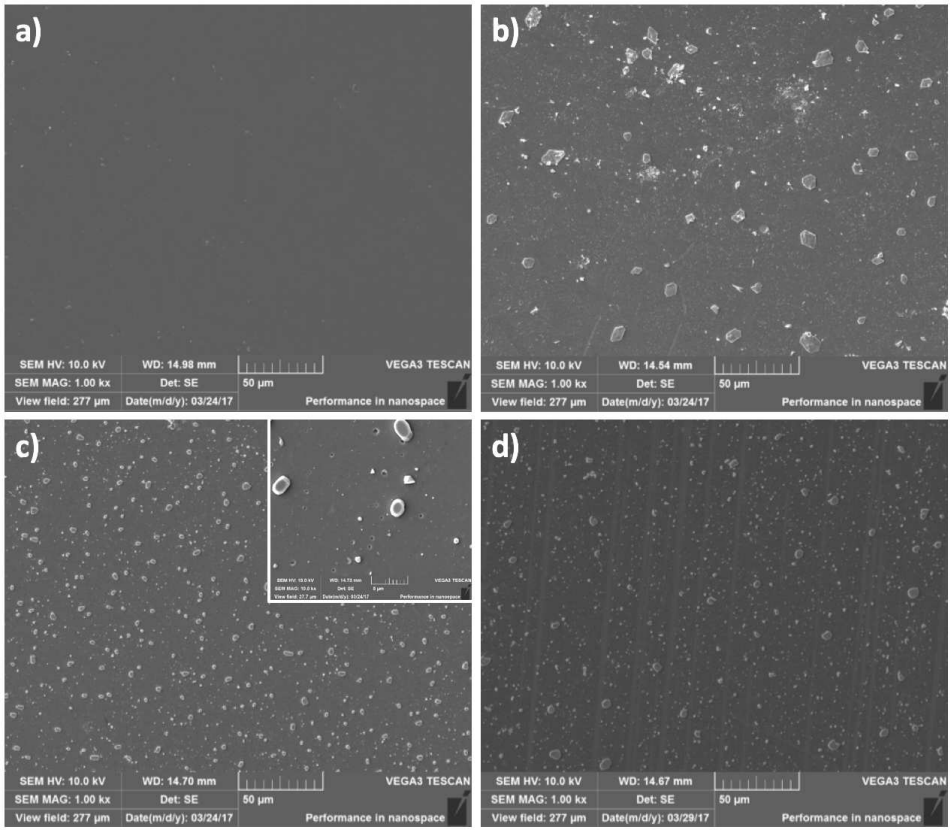

Figure 4.6. SEM images of Ge surface in direct source samples: a) pre-annealing Sb thin film; b) annealed at 570 °C; c) annealed at 610 °C; d) annealed at 630 °C. Inset in Fig. c: magnified view to highlight holes on the Ge surface.

in the grains decreases from 95:5 (sample annealed at 570 °C) to 86:14 (sample annealed at 610 °C). The latter atomic ratio is very close to that of eutectic Ge:Sb (15:85). These findings seemed to indicate the existence of a transition temperature, above which a phase transition takes place and a new $GeSb_x$ phase with eutectic composition appears. When an annealing treatment is carried out below this temperature, a rearrangement of the Sb atoms gives rise to the formation of the big structures observed in Fig. 4.6b and Ge atoms are only marginally involved in this evolution. On the other hand, above the transition temperature a stronger interaction between Sb and Ge atoms produces the formation of this new compound, which involves the migration of Ge atoms to micrometrical grains and unfortunately promotes the formation of holes in the Ge substrate. As a matter of fact, any attempt to measure sheet resistance and Hall effect by electrical four-point probe method was unsuccessfully. This obviously demonstrates that a non-continuous doped layer is produced. Through Secondary Ion Mas Spectrometry (SIMS), Sb diffusion profiles

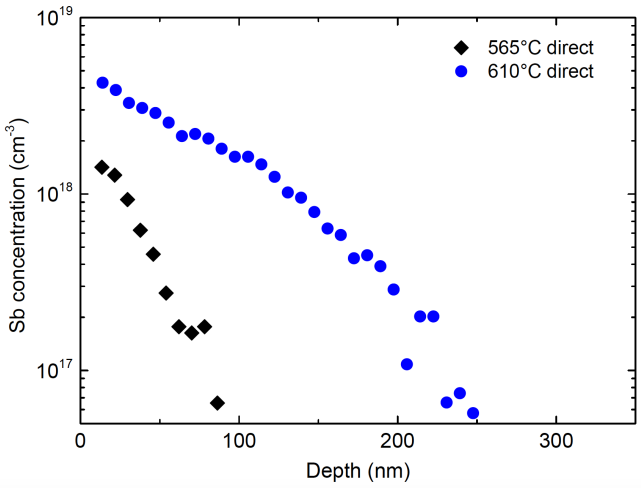

Figure 4.7. Sb diffusion profiles measured through SIMS in samples annealed at 565 °C and 610 °C.

were measured inside samples annealed at 565 °C and 610 °C and are shown in Fig. 4.7. SIMS is a quite local measurement (on about 100x100 micron spot) and these profiles demonstrate that some diffusion doping occurs.The maximum concentration increases with increasing the annealing temperature, as expected. However, they are not high (4.5x10^{18} cm^{-3} and 1.5x10^{18} cm^{-3}) and this, coupled with the presence of holes on the surface that would interrupt the junction short-circuiting the bulk, makes this doping technique not much promising.

4.2.2 Sb diffusion in furnace from remote source

The previous findings show that a direct deposition of the Sb source on Ge surface leads, during the high-temperature annealing, to significant changes in the homogeneity of the Sb film and induces severe damage in the morphology of Ge surface. As shown before, many holes hundreds of nanometers deep are formed on the Ge surface thus prejudicing the continuity of the diffused layer. For these reasons, a different configuration was adopted for Sb deposition and diffusion: Sb film was sputtered on a Si substrate, which was used as an Sb source in the following thermal annealing. The same annealing treatment at 610 °C was done on several samples, while testing different distances between the Ge surface and the Sb remote source: 0.2 mm (sample A), 1.5 mm (sample B) and 8.5 mm (sample C). SEM inspection of Ge surfaces showed very similar features in samples A and B, annealed at smaller distances from the source. So in Fig. 4.8 we just report a comparison between surface morphologies of samples B and C. All samples showed a strongly inhomogeneous

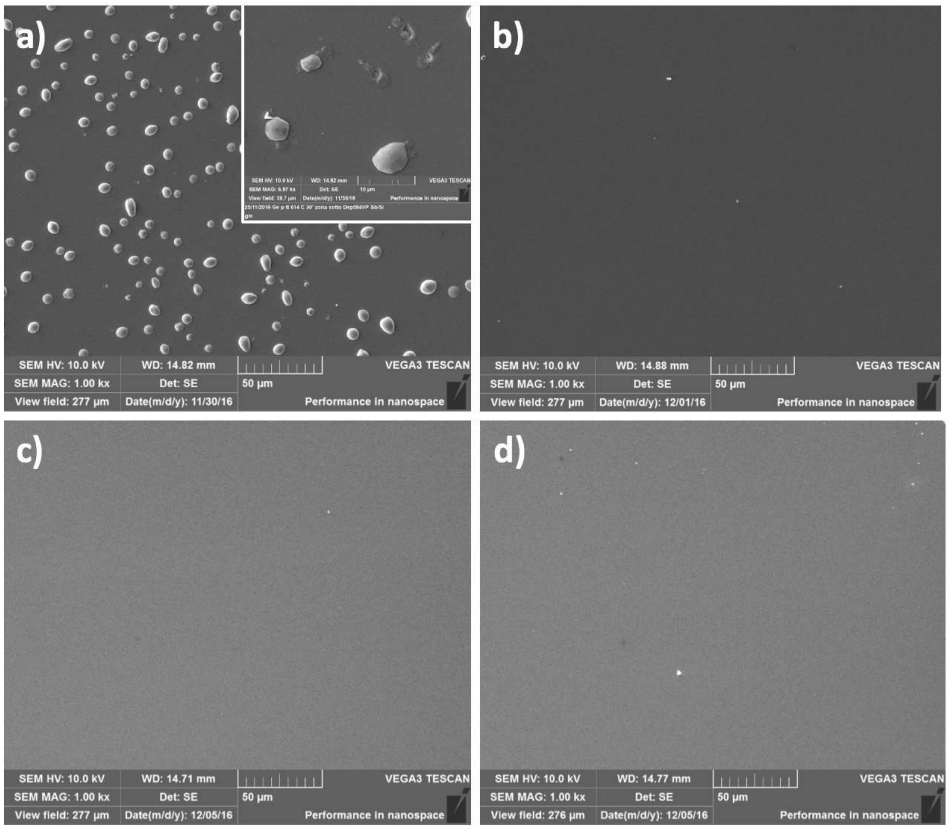

Figure 4.8. SEM images of Ge surface in remote source samples: a) sample B (1.5 mm distance) shadowed surface; b) sample B unshadowed surface; c) sample C (8.5 mm distance) shadowed surface; d) sample C unshadowed surface.

morphology, with features depending on the position: the surface immediately under the Sb/Si source (*shadowed* surface) was characterized by the presence of many grains and holes, as it is shown in Fig. 4.8a. On the other hand, these defects didn't appear on the surface further away from the source (*unshadowed*), which remained very smooth and homogeneous as can be seen in Fig. 4.8b. Through AFM the roughness in this unshadowed region resulted to be comparable to that of the bare Ge substrate. The striking thing was that when the distance between the Sb/Si source and Ge surface was further increased (sample C), both grains and holes disappeared even in the shadowed region and the whole sample surface appeared smooth and homogeneous (Fig. 4.8c and d). Choosing the largest distance between source and sample, 8.5 mm, to get the best surface quality, some diffusion treatments were performed at different temperatures: thermal annealings up to 615 °C, 700 °C, 740 °C and 790 °C, with an insertion time of 30 minutes. Through Secondary Ion Mas Spectrometry (SIMS), Sb diffusion profiles were measured in unshadowed clean surfaces

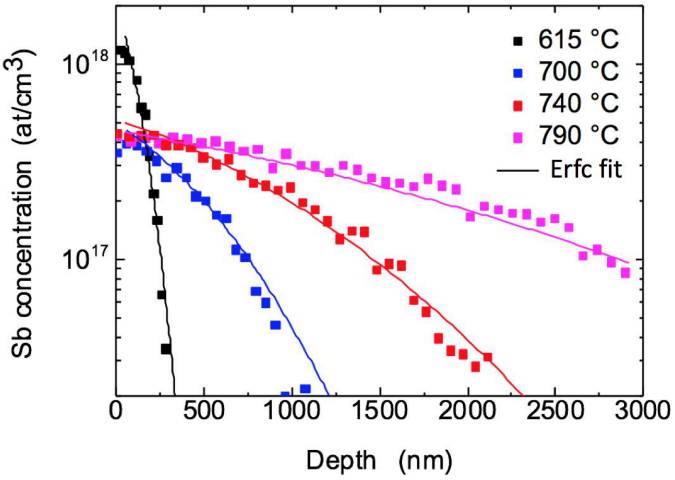

Figure 4.9. Sb diffusion profiles measured in unshadowed surfaces for samples annealed with different thermal budgets.

of all samples. They are shown in Fig. 4.9.
SIMS performed at different positions (not shown) presents a quite homogeneous doping profile. This indicate that Sb diffusion through the N_2 atmosphere is quite high and distributes Sb over a large and homogeneous area. According to Chapman Enskong theory, Sb diffusion coefficient in N_2 is about 3 cm^2/s [103]. Thus, only few seconds are needed to Sb to be spread over the sample distances. In closer geometries, a partially closed cavity is formed between Si and Ge and this probably increases a lot the Sb concentration over Ge surface, inducing phase transitions and defects, as in the previous direct case.

Analysis of the diffusion regime

Starting from these concentration profiles, we did an analysis to determine the diffusion regime (intrinsic or extrinsic) and consequently compared the obtained diffusion coefficients of Sb in solid Ge with the literature. We considered the remote source as a constant gas source of Sb, hence we used the diffusion model for an inexhaustible source, also described in Chapter 1. Concentration profiles have been fitted through:

$$C = C_0\, erfc\left(\frac{x}{2\sqrt{D_{eff}\, t}}\right) \tag{4.2}$$

where C_0 is the concentration at the surface, D_{eff} is an effective diffusion coefficient, x is the depth coordinate and t the annealing time. Through the fitting procedure

we calculated D_{eff} and the diffusion lengths $\sqrt{D_{eff}\,t}$. The latter are reported in Table 4.1. Since the Sb concentration we are dealing with are less than the intrinsic

Table 4.1. Sb diffusion lengths L_D; intrinsic carrier density of Ge n_{in} (calculated by Ref. [29]) and the $\langle (n/n_{in})^2 f \rangle$ factor calculated through Eq. (4.4) *and* (4.5).

Sample	$\mathbf{L}_D$	$\langle \mathbf{(n/n}_{in}\mathbf{)}^2\,\mathbf{f} \rangle$	$\mathbf{n}_{in}$
615 °C 30 min	75.2 nm	1.40	2.32x10^{18} cm^{-3}
700 °C 30 min	483.4 nm	1.15	3.84x10^{18} cm^{-3}
740 °C 30 min	791.6 nm	1.07	4.73x10^{18} cm^{-3}
789 °C 30 min	1657 nm	1.14	5.96x10^{18} cm^{-3}

concentration at each temperature, we consider $D_{eff} = D_{in}$, where D_{in} is the diffusion coefficient for an intrinsic semiconductor. According to the literature [24, 29], the diffusion coefficient of Sb in Ge depends on the carrier concentration (n) and the doping Sb concentration measured through SIMS (C) by means of the following equations.

$$D = D_{in}\left(\frac{n}{n_{in}}\right)^2 f \tag{4.3}$$

$$n = \frac{C}{2} + \sqrt{\left(\frac{C}{2}\right)^2 + n_{in}^2} \tag{4.4}$$

$$f = \frac{2n}{\sqrt{C^2 + 4n_{in}^2}} \tag{4.5}$$

The square trend in equation (4.3) is due to the fact that Sb diffuses by the mediation of double charged vacancies defects, while the *f* factor takes into account the effect of the drift of charged species, in the junction field [24]. The average factor $\langle (n/n_{in})^2 f \rangle$ was evaluated for each profile and reported in Table 4.1. As it can be noted, the factor is sensibly different from 1 only in the case of the lower temperature annealing. This is due to the fact that, at higher temperature, the Sb concentration is lower than n_i and therefore intrinsic regime is present. Therefore, mathematically, in this case Eq. (4.4) results in n=n_i and Eq. (4.5) in f=1. This physically means that thermal excitation dominates the carrier population, thus both the n-doped zone and the p bulk zone are intrinsic. No real junction is formed at those temperatures. The intrinsic diffusion coefficient is estimated as the ratio of D_{eff} and $\langle (n/n_{in})^2 f \rangle$ and reported in Fig. 4.10, together with the phenomenological value of intrinsic *D* as determined by Brotzmann et al. [29].

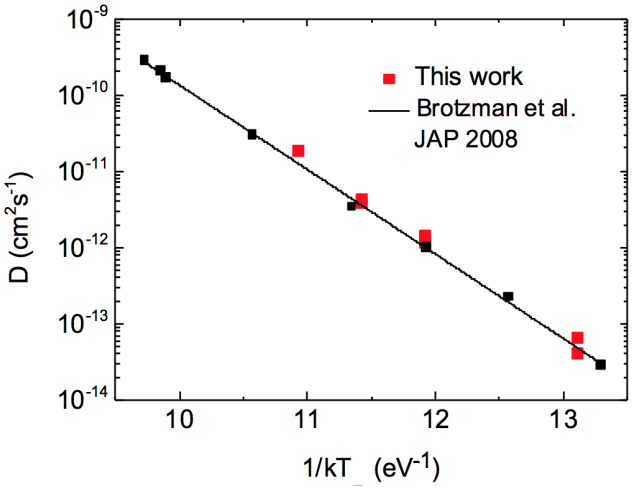

Figure 4.10. Sb intrinsic diffusivity from a remote sputtered source, compared with the literature Sb intrinsic diffusivity [29].

As it can be noted, a very good agreement is obtained for all data. This demonstrates that the use of a remote sputtered source induce a local Sb diffusion compatible with well assessed equilibrium diffusion models. Unfortunately, the relatively low content of Sb does not allow for the formation of a good contact between the metal tip and the doped layer, thus it was not possible to perform a direct evaluation of Sb electrical activation. On the other hand, the agreement between our diffusivity and that from the literature indirectly attests the elevated Sb activation.

Analysis of effective diffusion activation energy

The above analysis demonstrates the good agreement between diffusion literature data and our data, by taking properly into account the extrinsic diffusivity phenomenon. Here we also apply, to Sb annealing data, the same kind of analysis we did for P spike annealing data (see paragraph 3.2.4), through which an effective activation energy was extracted including both intrinsic and extrinsic effects in a single activation energy. This kind of analysis will be useful in chapter 5, where data of both P and Sb annealings will be used in terms of thermal budget, to compare diffusion processes with the bulk contamination effect.
Diffusion lengths L_D for the different annealing temperatures were calculated by fitting the profiles in previous paragraph and are reported in Table 4.1. Thermal budgets where calculated for each annealing by using different effective diffusion activation energies in the range (2 - 3.3eV). Then, $ln(L^2)$ were plotted as function of $ln(TB)$, doing a plot for each value of activation energy. All groups of data were fit-

ted through a linear function with slope fixed to 1.
In Fig. 4.11a we compared the the mean square deviation (MSD) of data from each fitting. The best fit was obtained for the value E_{act} = (2.7±0.1) eV, with a MSD of 0.04. From the resulting intercept we obtained D_0 = 148.6 cm^2s^{-1}. In Fig. 4.11b all diffusion data and the best fit are reported.

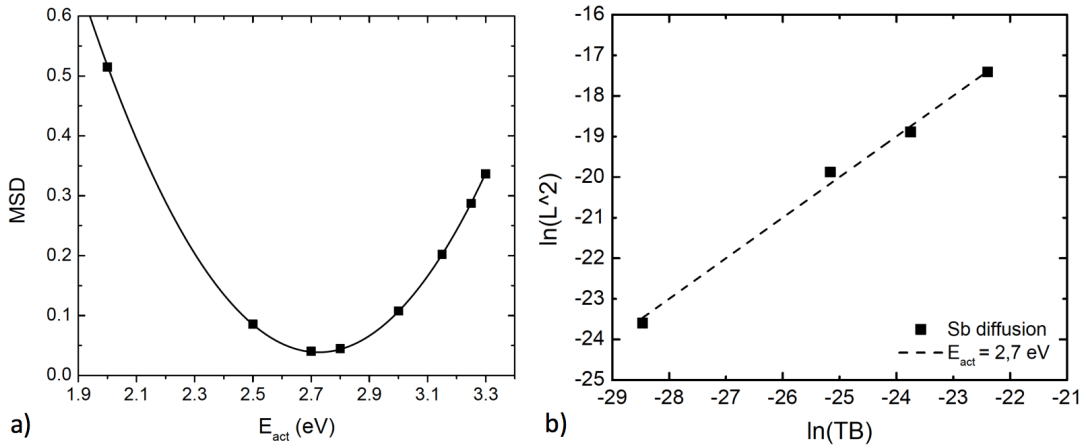

Figure 4.11. Sb diffusion analysis. a) Mean square deviations (MSD) of data from each fitting are reported as function of the correspondent activation energy. b) All diffusion data and the best fit, obtained for E_{act} = 2.7 eV.

4.2.3 Sb diffusion via laser thermal annealing

Sb diffusion via laser thermal annealing (LTA) is a preliminary but promising study we have started, in order to check if out-equilibrium processes can aid for the formation of junctions without any contamination. Contamination tests will be presented in paragraph 5.2.3, while a first small gamma detector will be tested and discussed in chapter 6.
Here some first characterizations of the doping process are presented, which have been recently performed.
After having done a 1 pulse laser annealing treatment on the circular Sb film deposited on a HPGe sample (Fig. 4.3), the first characterization we did was a SIMS measurement of Sb diffusion profile inside HPGe. In Fig. 4.12 the result is shown. Considering data collected in the first 15 nm of material not accurate, we performed a linear extrapolation at the surface. The diffusion profile has got an estimated maximum concentration at the surface of 2.5x10^{21} cm^{-3} and a penetration depth of about (35±5) nm. Hence, laser annealing has allowed to reach a dopant concentration

at the surface two order of magnitude higher than the solid solubility of Sb in Ge ($1.2x10^{19}$ cm^{-3}).

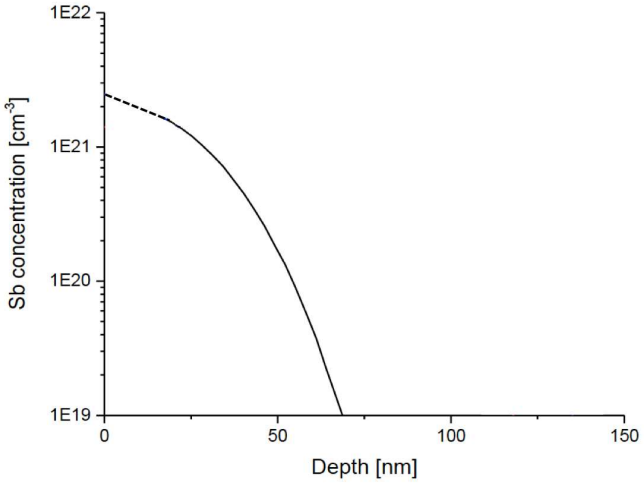

Figure 4.12. SIMS characterization of Sb diffusion profile inside HPGe after direct sputtering and laser thermal annealing.

Characterization of the electrical activation

Surely it is fundamental to verify the electrical activation of the dopant, that would be obtained only if Sb atoms are placed in substitutional position in the Ge lattice. However, in case of this sample it was very difficult to perform and interpret four-point probe electrical measurements. This because, at room temperature, the underlying HPGe substrate is intrinsic (with both carrier types due to thermal energy) and so there is not a depletion region toward the n-type carriers of the bulk. Moreover, the sample geometry is not standard, because the highly-doped circular layer is placed just in the center of the front surface and surrounded by intrinsic surface, see the scheme 4.13. Hence, both the geometry and the type of junction are not appropriate for four-point probe measurement and the result will be just preliminary. In fact this particular geometry was conceived just to carry out a diode characterization, reported in chapter 6.
In Fig. 4.13 there is a schematic of the sample structure with the four-point-probe system positioned above for the electrical measurement. The schematic is completely in scale except for the thickness of the Sb-doped layer, which in reality is orders of magnitude smaller with respect to the substrate ($\sim$ 60 nm maximum thickness, versus 2 mm). We used a small set of point probes, spaced 2.7 mm from each other. Both resistivity and Hall-effect measurements were performed, but only at

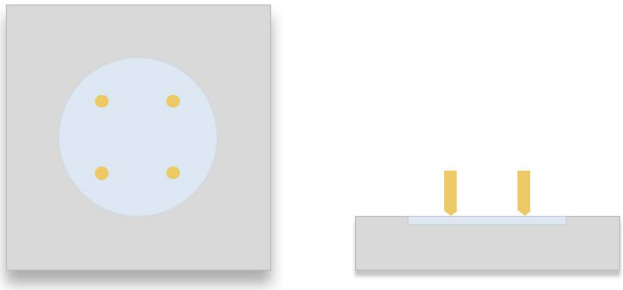

Figure 4.13. Schematic of the sample structure with the four-point-probe system placed above for measurements. It is fully in scale except for the thickness of the Sb-doped layer.

room temperature, because 2 mm thick samples can not actually be mounted on the cold stage using contemporary the 2.7 mm point probe. Experimental values are reported in Table 4.2.

Table 4.2. Experimental values measured through four-point probe electrical measurements.

$\mathbf{R}_{sheet}$ **(Ω/sq.)**	**Carrier dose (cm^{-2})**	**Mobility (cm^2/Vs)**
23	- 2.12x10^{15}	127

The contribution of the HPGe substrate is likely negligible, because even if a depletion region is not formed toward n carriers, they are in a very low intrinsic concentration (10^{13} cm^{-3}) and this makes the substrate very resistive.
Apart for the substrate contribution, a measurement error that we can correct is that due to point placement on the circular doped layer. As it was shown in Fig. 2.7 of chapter 2, the Van der Pauw method for electrical measurement on a circular sample requires to put the four probes in a square array exactly at the perimeter of the circle. Since our set of probes was smaller than the Sb-doped circle, the results reported in Table 4.2 are affected by errors.
Geometrical correction factors for both resistivity and Hall-effect measurements were calculated for this specific geometry, by following the simulation procedure already described in paragraph 2.4.3. We designed the experimental geometry with *COMSOL Multiphysics* design tools and then we simulated resistivity and Hall electrical measurements. In Fig. 4.14 the electric potential generated inside the Sb-doped layer during the two different measurements is shown.
The same simulations were done also for an ideal geometry, i.e. probes at the perimeter of the circle. Finally, by comparing the resulting voltages at the measuring probes, between the experimental and the ideal case, correction factors were calculated. For the sheet resistance measurement, F_R = *1.055±0.005* was obtained;

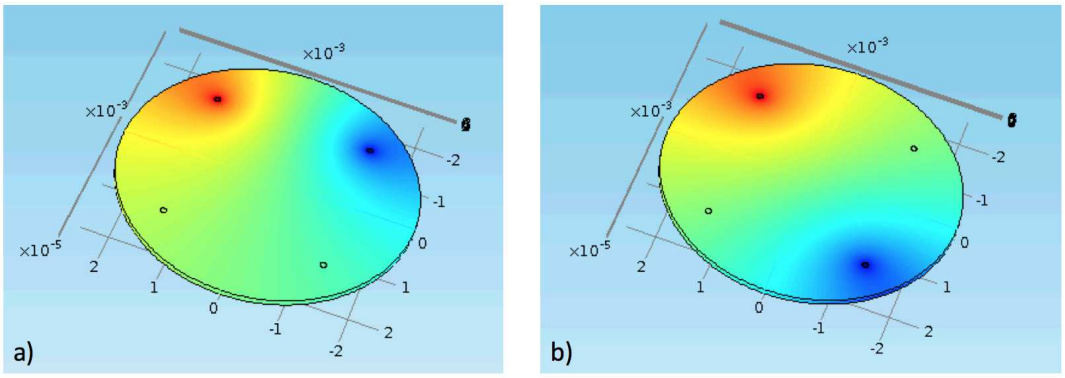

Figure 4.14. Electrical measurements simulations done with COMSOL Multiphysics to calculate geometrical correction factors. a) Electrical potential generated during a resistivity measurement. b) Electric potential generated during a Hall measurement.

regarding the Hall measurement, the correction factor to be applied to the carrier dose is F_n = *0.66±0.04*. The uncertainty ranges have been evaluated by simulating a deviation of the square array of probes from an exact centered position inside the circle.
The correction formulas are the following:

$$R_{real} = R_{exp} \cdot F_R \tag{4.6}$$

$$n_s^{real} = n_s^{exp} \cdot F_n \tag{4.7}$$

$$\mu_{real} = \mu_{exp} \frac{1}{F_n \cdot F_R} \tag{4.8}$$

and corrected values are reported in Table 4.3. At this point, to make an estimation

Table 4.3. Results of electrical measurements, corrected for the particular experimental geometry.

R_{sheet} (Ω/sq.)	Carrier dose (cm^{-2})	Mobility (cm^2/Vs)
24.3	- 1.4x10^{15}	182

of the electrical activation, the dose of active carriers reported in Table 4.3 should be compared with the total chemical dose of Sb atoms present inside the circular layer. This last datum can be calculated simply by integrating the SIMS profile of Fig. 4.12, obtaining a value of 6.5x10^{15} cm^{-2}. With the premise that this result is preliminary, due to a non-standard measurement geometry, we can estimate an electrical activation about 20%. This would correspond to a carrier concentration of ∼4.0x10^{20}, that is well over the Sb solid solubility in Ge. A different result was achieved through the joint analysis of sheet resistance and SIMS profile (method described in paragraph

2.4.4): the sheet resistance experimental value would be obtained by considering the diffusion profile as active at 50%. This would imply a concentration of active carriers equal to 9.3x10^{20} cm^{-3}.
In order to get a more accurate result regarding Sb-doping electrical activation, in the future it will be necessary to produce a standard geometry, i.e. a square Sb-doped layer on a thin resistive substrate and possibly perform electrical measurements at low temperature, thus totally excluding any substrate contribution.

4.3 Conclusions

Sb diffusion from sputtered sources has been studied with several approaches and very interesting properties have emerged, along with some drawback. The first technique we adopted to perform the doping, i.e. Sb diffusion in furnace from a thin film directly sputtered on Ge surface, led to the formation of a doped layer $\sim$ 80 nm thick, with a maximum concentration at the surface of 4x10^{18} cm^{-3}, in case of a thermal annealing at 610 °C for 30 minutes. Unfortunately, this technique causes serious damages to the Ge surface, appearing in the form of micrometrical grains and deep holes in the surface that interrupt the junction just created. We suppose that during the annealing the first to form are Sb grains. Then, a strong interaction between Sb and Ge atoms produces the formation of a $GeSb_x$ phase, which involves the migration of Ge atoms to Sb grains and induces the formation of holes in the Ge substrate.
The issues encountered with this technique have led us to design a second approach to carry out Sb diffusion in furnace: the use of a sputtered remote source. Through the help of SEM imaging, we could optimize the distance between the Sb source film and the Ge surface, in order to ensure the diffusion of Sb from a sublimated phase down into Ge, without inducing the formation of $GeSb_x$ micrograins on Ge surface. In this way we were able to obtain an optimum surface quality and good diffusion profiles. Several annealing treatments at increasing temperature were done, obtaining profiles of similar maximum concentration ($\sim$ 4x10^{17} cm^{-3}) and increasing thickness (from 150 nm a 3.3 μm). Exception is the sample annealed at 615 °C, thus below the Sb melting point that is 630 °C, because it presents a higher maximum concentration of $\sim$ 1.2x10^{18} cm^{-3}. By fitting these profiles through a complementary error function, we calculated the diffusion coefficients and a good agreement was found with Sb intrinsic diffusivity found in the literature. A further analysis of diffusion profiles has been performed, in order to extract an effective activation energy including both intrinsic and extrinsic effects.

Therefore, with remote doping technique we have an optimum control of surface quality and we can form continuous and homogeneous Sb-doped layers, but characterized by a low doping level. The concentration is lower than the dopant concentration usually used in HPGe contact (10^{19} cm^{-3}), however it could be meaningful to test it for application because by passing from 10^{19} to 10^{18} a small reduction of just 0.06 eV in the minority hole barrier is induced. The possibility to form a low resistance majority carriers electrical contact should be evaluated, but it could be still possible at such concentration thanks to the usual large area of detector contacts. Thus, this technique will be carried forward in next chapter for the study of thermally-induced impurities.
As a third approach to accomplish Sb diffusion from a sputtered source we used laser thermal annealing on an Sb ultra-thin film, directly sputtered on HPGe. The SIMS analysis gave an optimum result, in fact the energy density provided by a laser pulse has been enough to promote rapid and copious diffusion of Sb atoms from the ultra-thin film down into the molten layer of Ge. The diffusion profile is characterized by a maximum concentration of 2.5x10^{21} cm^{-3} and a thickness of 35$\pm$5 nm. Four-point probe electrical measurements were done to quantify the electrical activation of the dopant, but the sample structure was not standard and we could just make a preliminary estimation. An active dose between 20% and 50% of the total chemical dose of Sb atoms was found, corresponding to an active carrier concentration in the range (4.0-9.3)x10^{20} cm^{-3}, well over the Sb solid solubility in Ge. This value is surely enough for the application in gamma detectors. Therefore, after a measurement of bulk contamination reported in chapter 5, the junction obtained with Sb laser annealing will be tested as a diode and as a gamma detector in chapter 6.

Chapter 5

Characterization of thermally-induced doping defects in bulk HPGe

In the '60s, during early research on germanium, growth processes were improved to achieve the highest purity that in 1970 was already between 10^{10} and 10^{11} cm^{-3} [44]. Nowadays germanium crystals with impurity density less than 10^{10} cm^{-3} are available. However, purity is still a challenge for the improvement in the performance of applications such as radiation detectors and also for the study of impurity diffusion mechanisms. Despite growth purity, thermal processes often needed to make p-n junctions help the diffusion of impurities and defect states throughout the material and the entry of external contaminants that are thermally activated. All of this species such as dislocations, shallow impurities (Cu, Ga, B, Li, etc.) and deep-level contaminants (Cu, Fe, Zn, etc.) could increase the doping level of high purity germanium and also act as generation/recombination centers for free charge carriers, thus affecting the operation of any device [104]. Among the aforementioned, copper is one of the fastest diffusants in Ge at low temperature.
In the perspective of finding more suited doping techniques for the formation of the n-type contact in HPGe detectors, we are developing phosphorus diffusion from Spin-On-Doping (SOD) source, antimony diffusion from a remote source and antimony doping via Laser Thermal Annealing (LTA). All of them require high temperature annealing treatments, hence, to keep high the bulk purity thus saving detector operation, the problem of defects diffusion should be faced. In this chapter we characterize, through electrical measurements, doping defects thermally-activated during high temperature annealing in standard furnace. We demonstrate that, after a thermal treatment, a relation of Arrhenius type exists between the concentrations of electrically active defects inside HPGe and the annealing temperature, with a further dependence on the annealing time. With a simple model, we evaluate the activation

energy of the contamination mechanism of these active defects. We evaluate also the activation energies of P and Sb diffusion in HPGe. Such data are useful to identify a possible process window for doping without contaminating the material.
Data about impurity concentrations were collected through two different experimental setups, described in paragraph 2.4.1. First, we performed electrical measurements through setup No.1, which was not equipped with a magnetic field so it allowed to measure the sheet resistance of HPGe samples with decreasing temperature, in the range [120-300] K. Carrier concentration data were then calculated starting from sheet resistance values and using the curves of Ge mobility as function of temperature known in the literature [114, 115]. Meantime, the four-point probe system for electrical measurements described in paragraph 2.4.1, was completed with the installation of a refrigerator stage and a temperature control system. Therefore, data about bulk carrier concentration and carrier sign have been directly measured through Hall-effect at low temperature on selected samples, in the temperature range [90-220] K.

5.1 Experimental

5.1.1 Sample preparation

Two (100) HPGe wafers of p- and n-type, 2 mm thick (with a growth impurity concentration in the range [0.4 - 2]$\times 10^{10}$ cm^{-3} and a dislocation density < 2000 counts/cm^2) supplied by Umicore, were manually polished in order to smooth surfaces and then were cut into 10x10 mm^2 samples. Each sample was cleaned with hot 2-propanol, hot deionized water and HF 10% to remove dicing adhesive residue and native oxides. After, a more aggressive etching bath was done in HNO_3(65%):HF(40%) 3:1 solution for 5 minutes, in order to remove the residual mechanical damage from surfaces.
Two samples, one coming from the n-type wafer and the other from the p-type one, have been used as "reference samples". We measured them as cut, without any extra doping, in order to check if the bulk impurity concentration derived from our measurement did coincide with that guaranteed by the seller. Some samples were doped by spin-on-doping of phosphorus and gallium, using the technique described in chapter 3.1. One was doped by antimony diffusion in furnace from a remote source and one was doped with antimony as well, but through laser thermal annealing technique (as described in chapter 4). One other was implanted with boron ions, using standard implantation parameters: 22.6 keV energy and 1×10^{15} cm^{-2} dose.

In order to investigate any possible protective action against the diffusion of contaminants from the outside, one sample was sputtered with SiO_2 all around before performing a standard spike annealing treatment. Finally, some samples were put as-cut inside the furnace and spike annealed with different thermal budgets. In this way we could verify if electrically active impurities were introduced inside Ge by doping sources or if they were independent on the type of surface treatment. One last sample was annealed inside a different furnace (that will be called F2) in order to verify if the impurity level was dependent on the employed furnace. A list of all the analyzed samples is reported in Table 5.3, in next paragraph.
For what concerns the phenomenon of semiconductor contamination, it is normally enhanced by the application of a thermal budget. Anyway, avoiding high temperature annealing is sometimes infeasible, since many doping treatments require high temperatures. Therefore, having a standard tubular furnace at our disposal, the shortest thermal treatment we could do was a 10 minutes spike annealing characterized by rapid insertion and extraction of the sample, under 500 sccm constant N_2 flux. For each sample the T(t) curve including heating and cooling ramps was registered through a digital thermocouple and used for the calculation of thermal budgets. After doping processes, all highly-doped surface layers were removed through a bath in HNO_3/HF 3:1 solution for 20 s, leaving only four square doped areas at the sample corners, in order to improve the electrical contact during the successive four-wire electrical measurement. The removal of part of surface highly-doped layers is necessary to be able to measure the bulk impurity concentration. In fact, if doped layers were not removed, during the electrical measurement the current would pass through both the bulk and the surface layer, thus complicating the result. The same etching treatment was done also on some of the samples that hadn't received any doping process, removing 10 μm from the front surface.

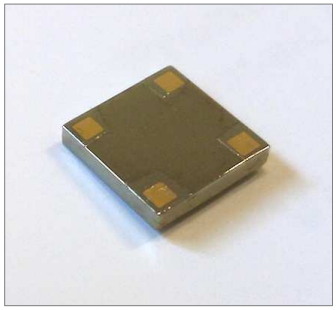

Figure 5.1. Example of an HPGe sample, of 1 cm^2 area and $\sim$2 mm thickness, ready for bulk electrical measurements. At the corners there are four square CrAu pads, done by sputtering. It is possible to see the central groove (10 μm deep), due to surface chemical etching for the removal of the doped layer.

5.1.2 Contact formation for electrical measurements

All samples were then contacted with sputtered CrAu square pads at corners, of 1.5 mm side (see Fig. 5.1). Chromium simply acts as an adhesive layer. If not used, sputtered Au would be damaged and scratched at the first touch. Then, all electrical measurements have been done by using thin Cu wires bonded to CrAu pads through malleable indium. We came to the choice of CrAu, while searching for a metal that could generate an ohmic contact with both p- and n-HPGe. According to the literature this is not possible, due to metal-induced gap states that are intrinsically formed at the metal/Ge interface, and which pin the Fermi level near to the valence band [105]. This implies that the electrical contact formed by metals on p-type Ge is always ohmic and that formed on n-type Ge always rectifying (characterized by a non-linear I/V function). Anyway, the width of the Schottky barrier is inversely proportional to the doping level. Therefore, if the Schottky barrier at the M/n-Ge interface is narrowed through high doping ($>10^{19}$ cm^{-3}), charge carriers can easily cross the barrier via quantum tunneling effect and an ohmic behaviour can be obtained also on n-Ge [106]. In the microelectronic research field, nickel germanide interphases (NiGe and Ni_5Ge_3) are created on highly-doped Ge, to obtain ohmic contacts characterized by the lowest value of contact resistance [106–110]. In the case of this thesis, and also by thinking to future HPGe segmented detectors, we don't need such a low contact resistance because we deal with contacts of large area (compared with those used in microelectronics). Indeed, the larger the metal contact area, the lower the contact resistance. Hence, we decided simply to sputter CrAu and see if the Schottky barrier formed with n-HPGe was too much highly resistive or not.

In Fig. 5.2a, we report two-wire I/V characteristic related to the most critical cases: as-cut p and n HPGe samples measured at low temperature (in this case 150 K). At this temperature intrinsic thermal carriers are cooled and in both samples there is an extrinsic impurity density of 10^{10} cm^{-3}. For the p-type sample, the I/V characteristic is linear and the two-wire resistance (calculated as the inverse of the slope) is 1.78x10^5 Ω, really a high value because it also includes contact resistances. For the n-type sample, the I/V characteristic deviates from linearity but it is not the result of two completely rectifying junctions. By fitting the central part of the curve in the range [-3;+3] μA (that corresponds to the range of working currents during 4-wire measurements) and inverting the slope, a value of 2.73x10^6 Ω for the resistance is obtained. The non-completely ohmic behaviour could be due to interface defects between CrAu and n-HPGe, created during the sputtering. Despite of this,

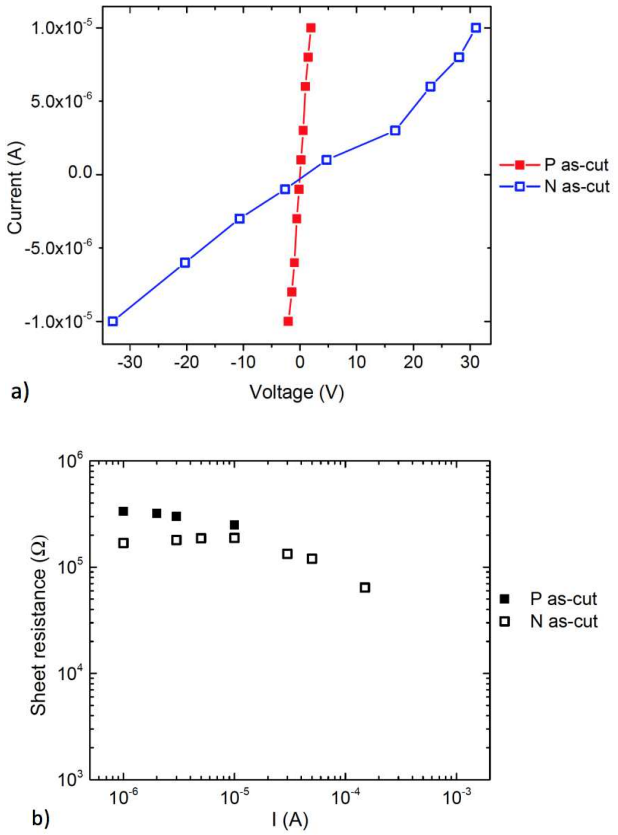

Figure 5.2. a) I/V characteristic of two-wire contact made with CrAu on p- and n-HPGe, measured at 150 K. b) Four-wire sheet resistance as function of the applied current, measured on the same samples at 150 K. These curves are used to identify the appropriate working current.

the quasi-ohmicity allows to perform 4-wire electrical measurements (technique that removes contact resistances) also in the most critical case that is n-HPGe at low temperature.

The reliability of 4-wire electrical measurements lies also on the choice of the current value to be delivered. Indeed, measured sample parameters like the sheet resistance must not depend on the value of current being used [60]. Thus, before starting the definitive measure, it is necessary to span a wide set of current values and see if a plateau for the sheet resistance can be identified. We did it for each measured sample and at each measurement temperature, in order to chose the right measurement current, but here in Fig. 5.2b we report the most critical case that is p- and n-HPGe at low temperature (150 K). In both cases a plateau can be seen at low current. For the n-HPGe sample the sheet resistance remains quite constant over the range [1-10] μA, while for p-HPGe the range is narrower [1-2] μA. For higher current values, an effect of sample heating occurs causing a lowering of the resistance. In order to

avoid a similar heating effect also at few μA, we have optimized the current delivery time (finally set at 50 ms) and the switch-off time between one measurement and the following (set at 1000 ms).

5.1.3 Setups for electrical measurements at low temperature

Van der Pauw sheet resistance measurements with decreasing temperature were done through setup No.1, described in paragraph 2.4.1. This setup doesn't allow to do Hall measurements, therefore we performed only the sheet resistance measurements at several temperature values in the range [120-300] K, by using the Van der Pauw method.
At a later time, more complete electrical measurements including the Hall effect were done on a set of selected samples, in order to evaluate the carrier type. To do them we used the setup No.2 described in paragraph 2.4.1, once completed with the installation of a temperature control system. In this case, to contact the sample we didn't use the four-point probes, but a Kapton harness to which the sample has to be bonded. To do the bonding, we proceeded in the following way. First, with the help

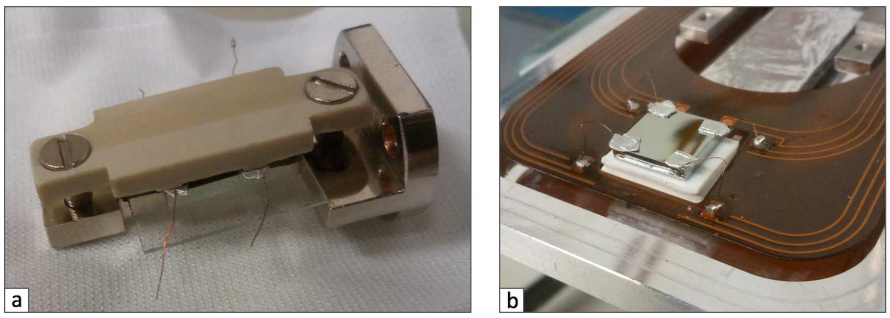

Figure 5.3. a) The PEEK bridge in this case has been used to press four wires on the sample CrAu pads, through the help of malleable indium. b) The sample is positioned above the ceramic part of the refrigerator circuit, inside the vacuum chamber. It is soldered to the Kapton harness.

of a PEEK (PolyEther Ether Ketone) bridge, four Cu wires were connected to CrAu pads through malleable indium (see Fig. 5.3a); then, the sample was positioned on the ceramic stage inside the vacuum chamber, with a drop of thermal-conductive grease. Finally the four wires were soldered to the harness contact points (see Fig. 5.3b). With this apparatus, the sign of active impurities together with their concentration and mobility were directly measured at low temperature, in the range [90-220] K.

5.2 Results and discussion

5.2.1 Experimental data

Figure 5.4 reports the results of four-wire electrical measurements with decreasing temperature, performed with setup No.1. As it was already said, with this setup we measured the sheet resistance of each sample, as function of the temperature. The

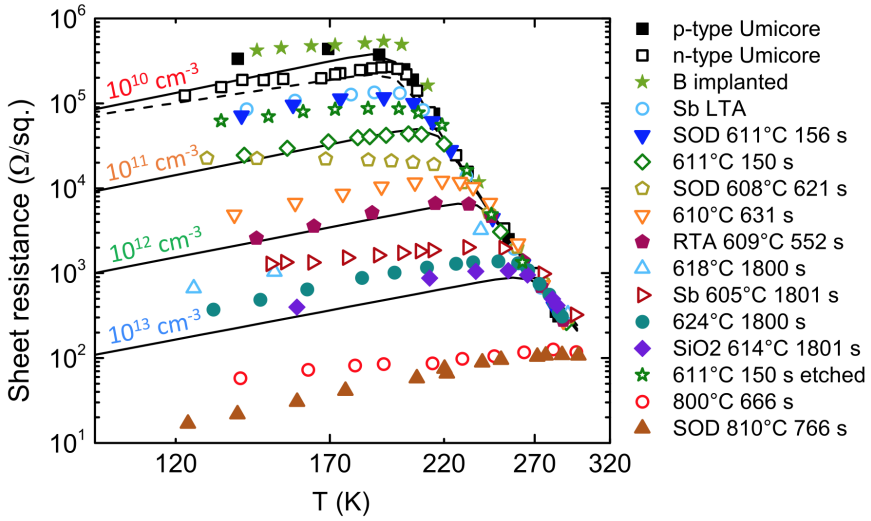

Figure 5.4. Sheet resistance data as function of temperature, for all samples. Full symbols refer to p-HPGe starting substrates, empty symbols to n-HPGe.

measurements were done with a current of 1μA, value chosen after having tested a range of currents looking for a plateau of sheet resistances. Then, a geometrical correction factor of 1% for both effects of contact size and spacing (F_R=1.01 calculated in paragraph 2.4.3) has been applied to data. Error bars are not visible because too small, however, more complex measurements that are those at low temperature on n-type samples (N Umicore and Sb LTA) are characterized by a maximum relative error of the 10%; while, regarding all the other samples, the errors are always below the 5%. Relative errors have been calculated starting from the standard deviation associated to each average sheet resistance value.

Looking at Fig. 5.4 and starting from room temperature (300 K), the sheet resistance rapidly increases until a maximum value is reached that is very different from sample to sample (from 10^2 to 5x10^5 Ω/sq.). Then, for all samples the sheet resistance reverses its trend and, by continuously lowering the temperature, it slowly decreases.

Another very important result comes out from Hall-effect measurements at low tem-

perature [90-220] K, done on a set of selected samples with setup No.2. This result is reported in Table 5.3, last column. At low temperature, thus when thermal carriers are frozen, all samples that had received a thermal annealing process showed positive carrier sign, even if their bulk was of n-type before any treatment. The only ones that showed n-type carriers were the reference n-type HPGe directly measured as-cut and the sample that received Sb doping by laser thermal annealing.
This result shows that during high-temperature annealing in standard furnace, a strong activation of acceptor levels occurs inside bulk HPGe, while laser thermal annealing technique seems not to involve this kind of problem.

5.2.2 Resistance theoretical curves

In order to better understand the experimental data and to extract quantitative information, the expected theoretical trend of sheet resistance as function of temperature was calculated, by considering different carrier densities. Starting with a square Ge sample of p-type doping, 1 cm^2 area and thickness t, the theoretical sheet resistance was calculated employing Eq. 5.1.

$$R_{sheet} = \frac{1}{t(pe\mu_h)} \tag{5.1}$$

Extrinsic carrier densities are expressed in Eq. 5.2, while the dependence of the intrinsic carrier density on temperature is reported in Eq. 5.3 [111].

$$p = \left(\frac{N_a}{2}\right) + \left(\left(\frac{N_a^2}{4}\right) + n_i^2\right)^{\frac{1}{2}}; \qquad n = \frac{n_i^2}{p} \tag{5.2}$$

$$n_i = 2\left(\frac{2\pi}{h^2}\right)^{\frac{3}{2}} m_e^{\frac{3}{4}}\, m_h^{\frac{3}{4}}\, (k_B T)^{\frac{3}{2}}\, exp\left(-\frac{E_g}{2k_B T}\right) \tag{5.3}$$

With the same reasoning, we calculated a theoretical sheet resistance curve also for n-type carriers of density 1x10^{10} cm^{-3}, because it will be compared with the n-HPGe reference sample. For this calculation, Eq. 5.1, 5.2 and 5.3 were used but in their form for an n-type semiconductor. To calculate sheet resistance curves, we also needed the mobility varying with temperature for different carrier concentrations (see Eq. 5.1). This was extrapolated from literature data, particularly from Ref. [112,113] for p-type and from Ref. [114,115] for n-type. Literature mobility curves were digitized through a software and digitized curves are shown in Fig. 5.5a and 5.5b.
Then, each of these curves was fitted in the temperature range [120-300] K, in order

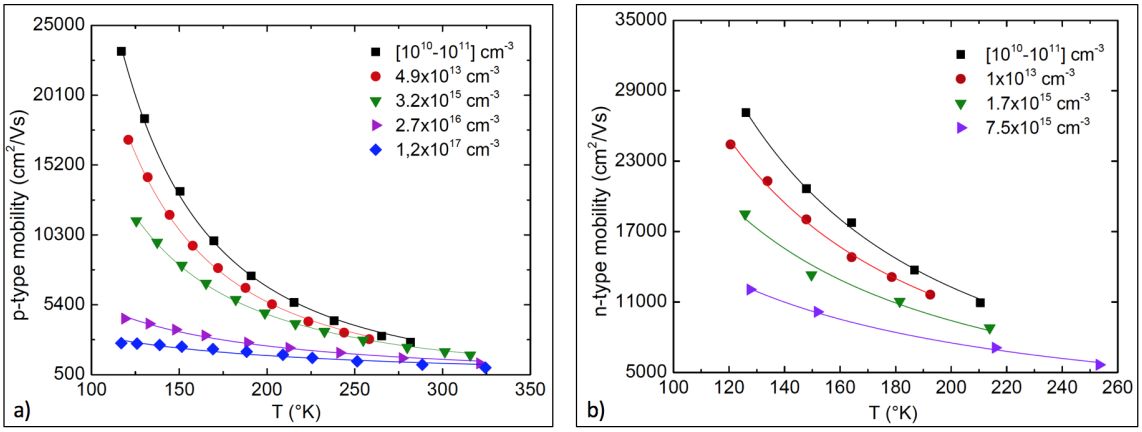

Figure 5.5. Plots of mobility as function of temperature for various carrier concentrations: a) p-type mobilities, digitized from Ref. [112, 113]; b) n-type mobilities, digitized from Ref. [114, 115]. Continuous lines are the fitting lines.

to find the best function describing it. The following power function, with fitting parameters A and B, was used:

$$\mu(T, C) = A(C) \cdot T^{B(C)} \tag{5.4}$$

where C is the dopant concentration. Fit results are reported in Tables 5.1 for p-type Ge, and 5.2 for n-type Ge. A and B parameters vary with the carrier concentration and give access to the mobility at any temperature, but only for discrete value of doping concentration (each curve correspond to a single concentration value). In order to overcome this problem, the discrete values for A and B obtained with the fitting procedure, were linearly interpolated within each dopant concentration interval. Then, we used the interpolated value to compute the mobility through Eq. 5.4, at any dopant concentration and temperature required by our analysis.

Table 5.1. Results of fitting procedure applied to curves of Fig. 5.5a, for p-type samples.

Carrier conc. (cm^{-3})	**Prefactor (A)**	**Power (B)**
$[10^{10}$-$10^{11}]$	7.95×10^{8}	-2.220
4.9×10^{13}	7.65×10^{8}	-2.231
3.2×10^{15}	1.14×10^{8}	-1.904
2.7×10^{16}	1.17×10^{6}	-1.159
1.2×10^{17}	1.81×10^{5}	-0.866

In Fig. 5.6 all theoretical sheet resistance curves as function of temperature are shown. Continuous lines for p-doping and the dashed line for n-doping. As can

Table 5.2. Results of fitting procedure applied to curves of Fig. 5.5b, for n-type samples.

Carrier conc. (cm^{-3})	Prefactor (A)	Power (B)
[10^{10}-10^{11}]	1.18×10^{8}	-1.731
1×10^{13}	5.00×10^{7}	-1.589
1.7×10^{15}	1.19×10^{7}	-1.345
7.5×10^{15}	2.11×10^{6}	-1.064

be observed, functions corresponding to the same doping type (p) have all the same shape, but they present a different height in the plot depending on the carrier density. Each function is characterized by two slopes. Starting from room temperature (300 K), the first trend is typical of the intrinsic regime: the semiconductor is intrinsic ($n_i >> N_a$, being N_a the extrinsic acceptor density) and thermally-activated charge carriers, which are 2×10^{13} cm^{-3} in Ge at 300 K, take part to conduction.

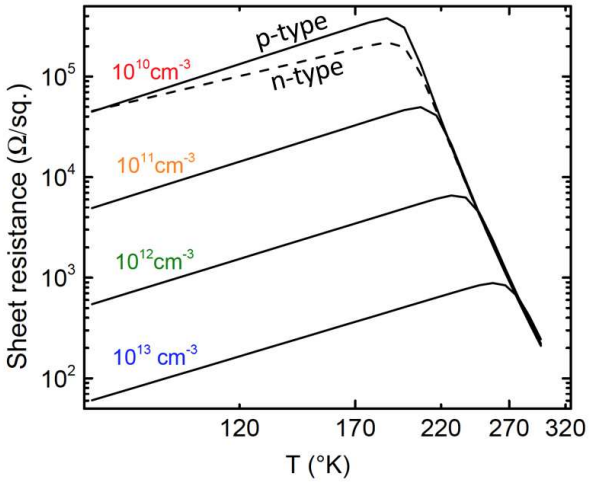

Figure 5.6. Theoretical sheet resistance curves, function of temperature. Continuous lines are for p-doping, the dashed one for n-doping.

By decreasing temperature, their density starts to decrease and the semiconductor becomes more resistive giving rise to the first trend. This part of the curve is the same straight line for all samples, as it is independent on doping levels. At a certain temperature value, the density of charge carriers originated from impurity ionization exceeds that of thermally activated carriers and a trend reversal occurs. This temperature value is different for each sample because the lower the impurity concentration, the lower is the temperature at which $N_a > n_i$ holds. By continuing to lower the temperature we enter the saturation regime: the density of ionized accep-

tors remains constant, but carrier mobility increases with decreasing temperature due to less lattice vibrations. This implies a sheet resistance drop, which has got a different slope depending on the impurity type (p- or n-) [111].

5.2.3 Contaminant concentration analyses

Looking back at plot 5.4, we observe that sheet resistance varies with temperature as expected. In fact the shape of experimental curves is the same as theoretical lines. Interestingly, experimental curves lie on different heights in the plot, meaning that our samples are characterized by different impurity concentrations.
From reported data, it is possible to derive carrier density curves as function of temperature, in order to identify the impurity level of each sample. This can be done by inverting Eq. 5.1 to calculate the density of active carrier starting from the resistance experimental data. The functions of mobility depending on temperature previously obtained with the fitting procedure were used. Resulting curves, representing the density of electrically active charge carriers as function of $1/k_BT$, are shown in Fig. 5.7. The intrinsic and saturation regimes are clearly distinguishable and the carrier density in the saturation regime corresponds to the density of ionized bulk impurities. Hence, for each curve we took the average concentration value N in the first 20 K of the saturation regime (first 20 K of each plateau, starting from the left), as the density of active ionized impurities. N values for all sample are reported in the fifth column of Table 5.3.

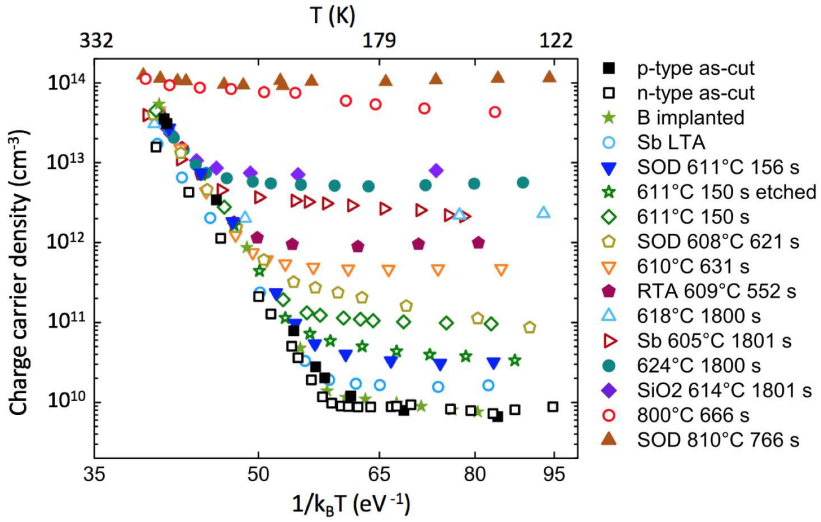

Figure 5.7. Charge-carrier density curves, function of $(k_BT)^{-1}$ obtained from sheet resistance data. Full symbols refer to p-type starting substrates, empty symbols to n-type.

Clearly, we are interested in the concentration of doping impurities (or contaminants) activated during our fabrication processes, quantity that will be called N_c. To calculate it, the following formula was used:

$$N_c = |_{(+-)}N - {}_{(+-)}N_{growth}| \tag{5.5}$$

where both N and N_{growth} are taken with their sign (+ for holes and - for electrons). Let us consider this example: in the most frequent case an n-type sample (-N_{growth}) is contaminated and becomes of p-type (+N). The amount of contamination is: N-(-N_{growth}) that is N+N_{growth}. Thus N_c>N holds and this is reasonable because contaminants had to compensate for the n-doping before than perform the p-doping.
Growth impurity densities N_{growth} are obtained from the impurity level of reference samples (first two N values in Table 5.3), equal to 8.7x10^9 cm^{-3} for n-type and 8.9x10^9 cm^{-3} for p-type. The concentration of thermally-induced active defects N_c is reported in Table 5.3, for each sample. In the table, there are also the results of Hall-effect electrical measurements done at low temperature [90-220] K with setup No.2. The columns N_{Hall} and *"Final carriers"* respectively report the density of active carriers (in this case directly measured) and their sign. The values of N_{Hall} should be compared with column *N* reporting the total density of ionized impurities. The compatibility is quite good, but there is a tendency for Hall concentrations (setup No.2) to be higher than those derived from sheet resistance measurements (setup No.1). Since sheet resistance data measured with the two different setups are completely compatible, as it can be seen in Fig. 5.8a, we can affirm that discrepancies arises when the magnetic field is applied during Hall measurements with setup No.2.
As a matter of fact, Hall measurements give access directly to mobility measurements while, in order to analyze the resistivity data collected with the first setup, we used the literature mobility values. In Fig. 5.8b, a comparison is shown between measured Hall mobilities and literature mobilities previously used for the analysis. Regarding Hall measurements, a geometrical correction factor F_n=0.84 (calculated in paragraph 2.4.3) for both effects of contact size and spacing under applied magnetic field, has been already applied to data before plotting. Error bars express an error of the 20%, calculated starting from the standard deviation associated to each average Hall datum. Measured Hall mobilities are lower than those of literature. It could be due to the fact the Hall factor could be different from 1. However, Hall factor values are known only for carrier concentrations higher that 10^{14} cm^{-3} [63]. Hence, we can't know if our Hall mobilities are affected by this second order effect or by other measuring artifices. For what concerns our measurement method, a further source of systematic error could be given by contact geometry. Indeed, through COMSOL

Table 5.3. List of all characterized samples and their most important parameters.

Starting carriers	Annealing treatment	Surface treatment	Surface Etching	N (cm^{-3})	N_{Hall} (cm^{-3})	N_c (cm^{-3})	Final carriers
n	-	-	y	-[8.7±1.5]x10^9	-[1.3±0.2]x10^{10}	-	n
p	-	-	n	+[8.9±3.3]x10^9	+[6.0±0.2]x10^9	-	p
p	-	B impl.	y	[9.5±2.1]x10^9	-	-	-
p	611 °C 156 s	P diff.	y	[3.4±0.6]x10^{10}	-	[2.5±0.9]x10^{10}	-
n	608 °C 621 s	P diff.	y	[2.0±1.0]x10^{11}	-	[2.1±1.0]x10^{11}	-
p	810 °C 766 s	Ga diff.	y	[1.1±0.1]x10^{14}	-	[1.1±0.1]x10^{14}	-
n	605 °C 1801 s	Sb diff.	y	[3.0±0.9]x10^{12}	-	[3.0±0.9]x10^{12}	-
p	614 °C 1801 s	SiO_2 sputt.	n	[7.8±1.0]x10^{12}	-	[7.8±1.0]x10^{12}	-
n	611 °C 150 s	-	n	[1.1±0.2]x10^{11}	-	[1.2±0.2]x10^{11}	-
n	611 °C 150 s	-	y	[4.8±1.6]x10^{10}	-	[5.7±1.8]x10^{10}	-
p	(F2) 609 °C 552 s	-	n	[9.9±1.5]x10^{11}	+[1.8±0.2]x10^{12}	[9.8±1.5]x10^{11}	p
n	610 °C 631 s	-	n	[5.0±0.8]x10^{11}	+[9.0±1.0]x10^{11}	[5.1±0.8]x10^{11}	p
n	618 °C 1800 s	-	y	[2.2±0.3]x10^{12}	+[7.9±0.9]x10^{12}	[2.2±0.3]x10^{12}	p
p	624 °C 1800 s	-	y	[5.7±1.1]x10^{12}	-	[5.7±1.1]x10^{12}	-
n	800 °C 666 s	-	y	[6.9±2.2]x10^{13}	+[1.8±0.2]x10^{14}	[6.9±2.2]x10^{13}	p
n	LTA	Sb sputt.	n	[1.7±0.2]x10^{10}	-[1.3±0.5]x10^{10}	-	n

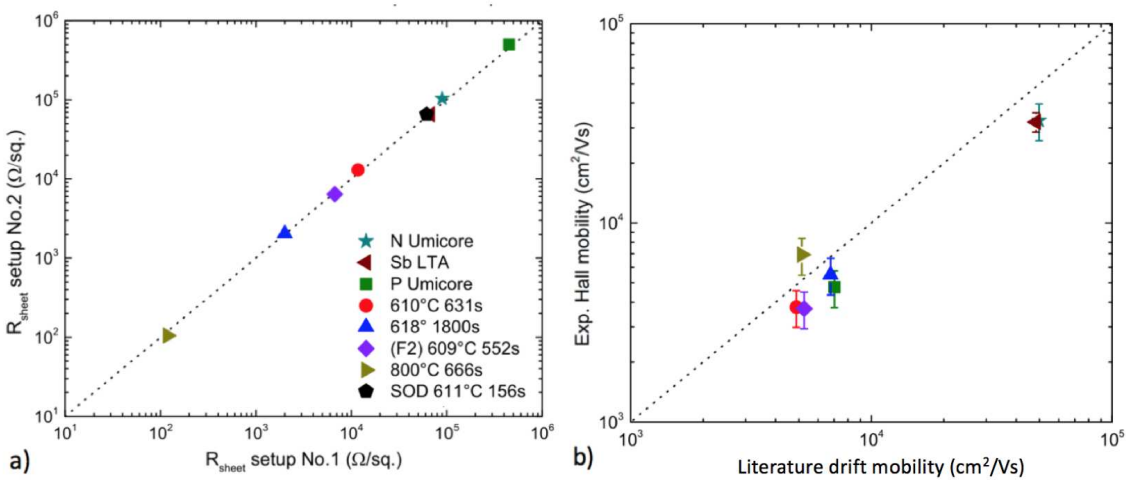

Figure 5.8. a) Comparison between sheet resistance measurements done with setup No.1 and No.2. All data lie on the equality line. b) Comparison between experimental Hall mobilities and literature mobilities. There is a fairly systematic discrepancy. The legend is valid for both plot.

simulations we calculated the geometrical correction factor for square CrAu pads, of 1.5 mm side. But, when we apply malleable indium in order to fix wires, it randomly spreads sometimes also out of the square pads. Therefore, indium could contact HPGe on a larger area than that considered in simulations. Errors introduced by irregular contact geometries affect much more Hall-effect measurements than sheet resistances. So this is a possible source of unknown error on our Hall measurements. Because of these uncertainties on N_{Hall} and beacause of the fact that it is a more complete data set, we decided to use concentration data derived from sheet resistance measurements to perform the analysis of acceptor impurities.
Now, let us look at the N_c column in detail. As expected, B ion implantation is a clean process, since it doesn't introduce any further contaminant into HPGe. A really remarkable result is obtained with laser thermal annealing of Sb: its impurity level N is $<2\text{x}10^{10}$ cm^{-3}, thus within the growth range guaranteed by the seller. This means that this doping technique doesn't introduce shallow levels inside HPGe. This is confirmed by the measurement of the Hall carrier density and of carrier type, that has not changed to p as it happened for the other processes.
Regarding the SiO_2 coating, it hasn't provided any protective action since the underlying bulk is contaminated even more than a naked sample that had received the same annealing treatment. Samples coated with SOD sources are characterized by the same (or even less) impurity density as other as-cut samples that received a similar annealing treatment. This means that the SOD film doesn't introduce further impurities inside Ge. The same for the sample doped with Sb from a remote source.

It is interesting to look at the sample treated inside a different furnace (F2), because it turns out to have a slightly higher impurity density than others annealed in furnace F1 with the same temperature ramp. This could suggest that active doping species under study are not intrinsically present inside HPGe or formed during the process and then activated during the annealing, but probably they are impurities coming from the external environment and diffusing inside HPGe during the thermal treatment. Anyway, the most evident behavior emerging from the observation of Table 5.3 is that the concentration of doping defects increases by moving to higher thermal budgets.

5.2.4 Phenomenological model of contamination process

The contamination of the HPGe crystal may occur probably because of the diffusion of external contaminants, or because of the formation of intrinsic defects under annealing (dislocation multiplication, point defects clustering, etc.). In any case an equilibrium concentration for doping contaminants is reached for long annealing time at a given temperature.
The aim of this section is to try to have a systematic model that allows to explain the contamination process under furnace annealing. The model, in a first step allows to order all data according to the pure thermal effect. Then, the intention is to try to understand if there is also some other effect that may influence the contamination. In a second step, the phenomenological calibration of such model will furnish a useful framework to asses the possibility of finding doping process windows while keeping the contamination under acceptable limit.
The simple empirical model can be written starting from the description of the dependence of impurity density on temperature and time. First, a standard Arrhenius relation is assumed between the equilibrium impurity/defect concentration, achieved with long annealing treatments n_{eq}, and temperature (Eq. 5.6). Also the dependence on the annealing time should be considered. Eq. 5.7 describes the rate r through which the equilibrium concentration is achieved. A non-equilibrium dynamic is assumed according to which, the rate with which dopant contaminants grow is proportional to their "distance" from the equilibrium.

$$n_{eq} = n_0 \, exp\left(-\frac{E_{act}}{k_B T}\right) \tag{5.6}$$

$$\frac{dn}{dt} = r(n_{eq} - n) \tag{5.7}$$

Spike annealing treatments that we usually do are brief (8-12 min) and therefore we make the reasonable assumption that the system is always far from the equilibrium[1]. Thus, this relation holds $n_{eq} >> n$ and from Eq. 5.6 and 5.7 we obtain Eq. 5.8. In Eq. 5.8 we have also inserted the dependence of the annealing temperature on time, since the sample undergoes temperature ramps during the annealing. The whole can be integrated over time (Eq. 5.9).

$$\frac{dn}{dt} = r\, n_0\, exp\left(-\frac{E_{act}}{k_B T(t)}\right) \tag{5.8}$$

$$n = r\, n_0 \int exp\left(-\frac{E_{act}}{k_B T(t)}\right) dt \tag{5.9}$$

Given an ideal annealing process done at constant temperature T for a time t and characterized by a perfectly square ramp, its thermal budget (*TB*) that is a quantity with dimensions of time, is quantitatively defined as the product between the annealing time and the Arrhenius exponential, Eq. 5.10. For a real annealing process, in which temperature varies with time T(t) and heating and cooling ramps are crucial, the thermal budget concept can be generalized as the integral of the Arrhenius exponential over time, Eq. 5.11.

$$TB = t \cdot exp\left(-\frac{E_{act}}{k_B T}\right) \tag{5.10}$$

$$TB = \int exp\left(-\frac{E_{act}}{k_B T(t)}\right) dt \tag{5.11}$$

Therefore, going back to our model, the integral in Eq. 5.9 is nothing more than the thermal budget of each annealing process and, by applying the natural logarithm to all the equation, a linear relation between *ln(n)* and *ln(TB)* is obtained, Eq. 5.12.

$$ln(n) = ln(r \cdot n_0) + ln(TB) \tag{5.12}$$

This last equation can be used to fit our experimental data, particularly those done in the same furnace, looking for the activation energy of the contamination process. For each sample, its contaminant density is known and it corresponds to N_c in Table 5.3. On the contrary, the value of the thermal budget is not known. Each annealing temperature ramp was measured through a thermocouple, so we know *T(t)* in Eq. 5.11, but we still miss the activation energy, a parameter that we want to discover

[1]Typical annealing times to test solubility in solids are many hours up to days. It depends from system to system and the hypothesis to be tested is: How well does the model work.

through the fit procedure. So we tested a set of likely values for E_{act} (1- 3 eV) and for each one of these values, we calculated the Arrhenius function *f(t)* that is argument of the thermal budget integral:

$$f(t) = exp\left(-\frac{E_{act}}{k_B T(t)}\right) \tag{5.13}$$

In Fig. 5.9 the plot of *f(t)*, for E_{act} = *2.1 eV*, is shown for all samples. Then, thermal

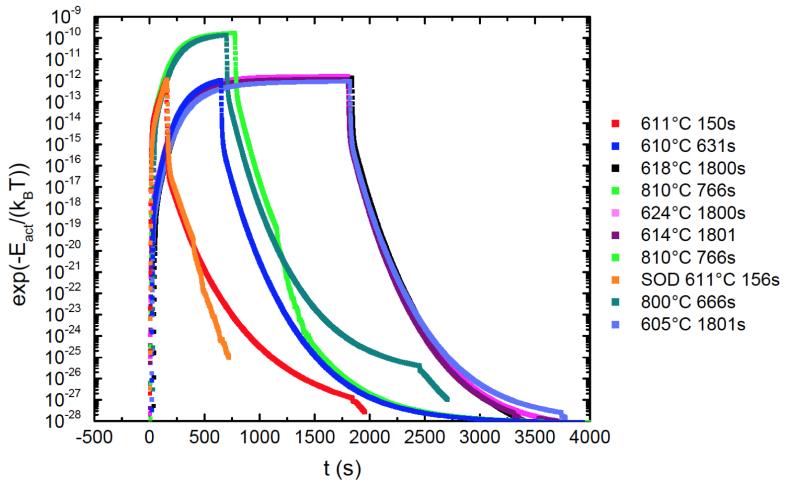

Figure 5.9. Plot of Arrhenius functions f(t) of all samples, calculated for an activation energy of 2.1 eV. The area under each function is the thermal budget of the peculiar annealing treatment.

budgets are easily calculated as the integral of these curves. For each value of E_{act}, once calculated the thermal budgets for all samples, it is possible to create a plot *ln(n)* vs. *ln(TB)*, where each point refers to a single sample. Points should lie on a straight line with a slope equal to 1, according to the linear relation in Eq. 5.12.
In Fig. 5.10a we have reported groups of points corresponding to different values of activation energy. Then, each group of data was fitted with a linear function, by keeping fixed the slope to 1 so that Eq. 5.12 is valid. In Fig. 5.10b we compared the mean square deviation (MSD) of data from each fitting. The best fit was obtained for an activation energy E_{act} = (2.1±0.1) eV, with a reduced MSD of 0.336. From the resulting intercept we obtained $r \cdot n_0$ = 2.1x10^{21} cm^{-3}s^{-1}.
In Fig 5.11 we report the best fit as in Fig. 5.10, in a magnified scale. As can be noted, the model with only 2 free parameters allows to order the data in a quite defined trend. It is worth to note that data comes from very different annealing procedures: temperatures from 600 to 800 °C, times from 2 to 30 minutes and different temperature-ramp shapes. On the other hand, it can be noted that any single data

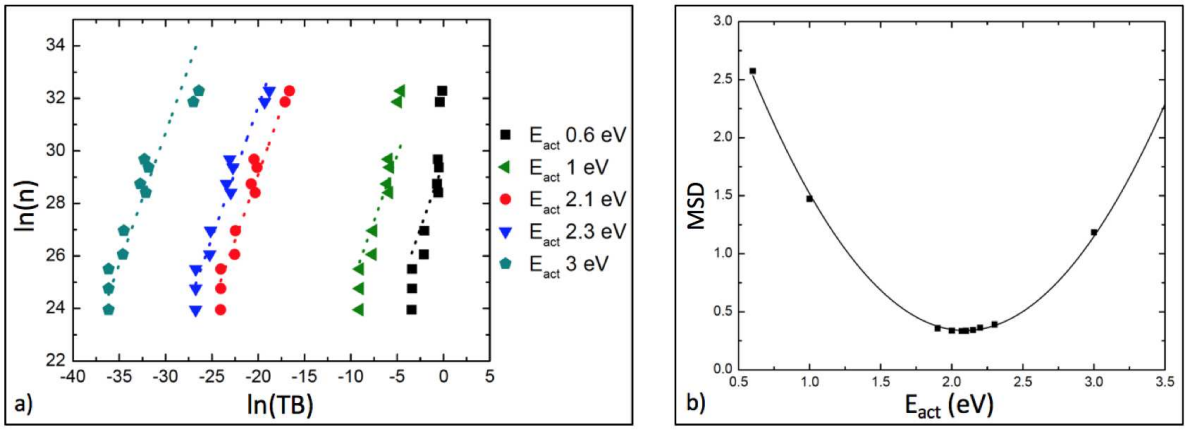

Figure 5.10. a) Data are reported several times, using different values of activation energy in the calculation of thermal budgets. Dashed lines represent linear fits with slope fixed to 1. b) For each tested value of activation energy, the mean square deviation (MSD) of data from each fitting is reported.

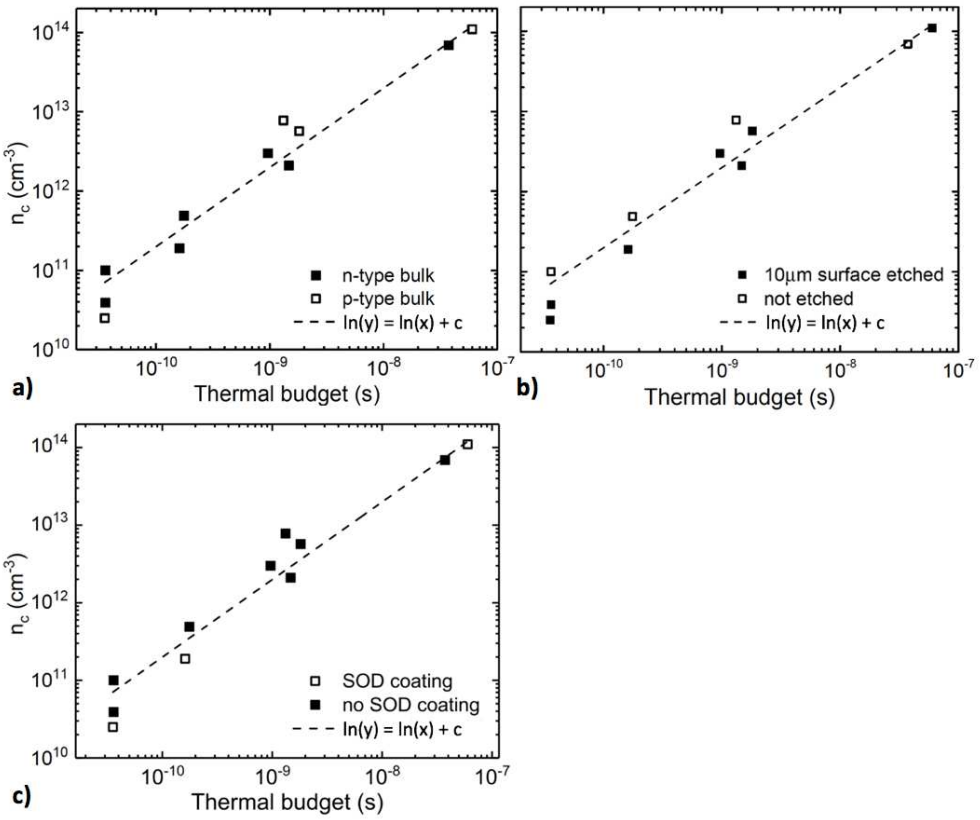

Figure 5.11. The best linear fit of the data is shown. a) Comparison between samples with starting n-type bulk and starting p-type bulk. b) Comparison between samples whose surface was chemically etched (∼10 µm) and entire samples. c) Comparison between SOD coated samples and all the others.

has a significant scattering from the model.
In order to understand if there are some particular features in the sample preparation that influence such scattering, in Fig. 5.11 we report data and the best fit, but in each graph different categories of samples are compared: p or n starting bulk (Fig. 5.11a), surface etched or not (Fig. 5.11b), SOD coated or not (Fig. 5.11c). In Fig. 5.11a, both starting bulk types seem to be homogeneously distributed around the fitting line. This suggests that the contamination process is independent on the substrate type. This is not really surprising since at the annealing temperature of the processes thermal carriers are greater than $1x10^{18}$ cm^{-3} much greater than doping carriers. This means that all samples are equivalent for what concerns carriers during heating. Hence, the evolution of defects (their growth or diffusion) is influenced in the same way by both carrier types.
In Fig. 5.11b, a comparison between surface etched and non-surface etched samples is shown. In this case there is a clear correlation between the impurity density and surface removal, namely etched samples present a lower impurity level. If impurities concentrate in the first micrometers of material, this confirms that they come from the external environment and diffuse inside Ge during high temperature annealing. Thus most likely they are extrinsic, in-diffusing contaminants. This excludes all those species that, already present inside bulk HPGe, could be electrically activated during the annealing by forming complexes with other impurities or defects [104].
In Fig. 5.11c, samples that were annealed with the SOD source above are highlighted. This is in principle a fundamental step since we would like to answer the question if SOD is responsible for contamination. As a matter of fact, samples with SOD have a lower contamination density and this can be attributed not to a protective effect of SOD but most probably to the fact that they are all surface etched. Thus, there is not a direct correlation between the presence of the SOD source during the annealing and the contamination process. Particularly, it is important to observe that the SOD film doesn't introduce further contaminants.
By considering the p nature of the shallow dopant we are dealing with and also its provenance from the external environment, we confirm the many times cited idea that the contaminant could be copper. Cu is one of the most common surface contaminants and also one of the fastest diffusing impurity in Ge. Substitutional Cu atoms give rise to three acceptor levels in Ge and this is compatible with the p nature of active impurities we see. In paragraph 1.2.3 the diffusion mechanism of Cu in Ge was described, according to Ref. [28]. The two activation energies needed for Cu atoms to diffuse inside Ge and to reach the substitutional solubility are re-

spectively 0.084 eV and 1.56 eV. In order to contaminate the material, Cu has to be both solubilized and diffused into the Ge matrix. Therefore, we could expect that the activation energy of the contamination process should be at least the sum of the two energy costs, i.e. 1.64 eV. Our experimental data analysis reports an higher activation energy for contamination that is 2.1 eV. This is not in perfect agreement with our estimate, but we always have to consider that, beside diffusion and bulk solubility, the surface can furnish a further barrier for the contaminant to enter the bulk. Another possibility, is that the availability of Cu may vary with temperature. An higher activation energy means a stronger increase of the process with temperature, this means that there should be more Cu available the higher is the temperature. Under this hypothesis, it would be more realistic that the Cu source is the furnace itself and that the higher is the temperature the higher amount of Cu will be released by contaminated parts of the furnace. On the contrary, if we think that the Cu source is an accidental surface contamination, the Cu availability should decrease by Cu desorption by increasing temperature. Due to the very small amount of Cu that should be available to contaminate HPGe, it is not easy to further check such possibilities.

5.2.5 Process window for standard doping annealing

In our perspective to apply new techniques for the formation of the n-type contact on HPGe, it is interesting to understand if it is possible to make the doping process dominate on the contamination one. For this purpose we calculated the activation energies of P diffusion from spin-on-doping source (2.4 eV) and Sb diffusion from a remote source (2.7 eV), respectively in paragraphs 3.2.4 and 4.2.2. Once the activation energies are known, it is possible to identify, if it exists, an optimal range for doping thermal budgets, which allows dopant diffusion inside HPGe without contaminating. To find out this optimal thermal window, we set some critical thresholds. As regarding the density of doping contaminants n_c, in Eq. 5.14 we impose a maximum threshold n_c^{thr} = *2x10*^{10} *cm*$^{-3}$, in order to preserve the purity that is necessary to deplete the detector volume. Then, by applying the natural logarithm to the inequality of Eq. 5.14, one obtains Eq. 5.15.

$$n_c = n_0\, t\, exp\left(-\frac{E_{act}}{k_B T}\right) \leq n_c^{thr} \tag{5.14}$$

$$ln(t) \leq ln\left(\frac{n_c^{thr}}{n_0}\right) + \frac{E_{act}}{k_B T} \tag{5.15}$$

Eq. 5.15 defines a line in the t vs. $1/(k_B T)$ space that separates non-contaminating thermal budgets from contaminating ones (continuous line in Fig. 5.12). A sim-

ilar reasoning can be done to impose a minimum P and Sb diffusion threshold into HPGe (Eq. 5.16). Particularly, we imposed the threshold $L_{thr} = 200\ nm$ for dopant diffusion length, in order to ensure the formation of a continuous and homogeneously-doped contact layer. Then, by applying the natural logarithm to the inequality of Eq. 5.16, one obtains Eq. 5.17.

$$L^2 = L_0\, t\, exp\left(-\frac{E_{act}}{k_B T}\right) \leq L_{thr}^2 \tag{5.16}$$

$$ln(t) \leq ln\left(\frac{L_{thr}^2}{L_0}\right) + \frac{E_{act}}{k_B T} \tag{5.17}$$

Eq. 5.17 defines a line in the t vs. $1/(k_B T)$ space that separates sufficient thermal budgets from insufficient ones to obtain a 200 nm thick doped layer. In Fig. 5.12 the dashed line corresponds to P diffusion threshold, while the dotted one corresponds to Sb diffusion threshold. As can be observed, within the time and temperature

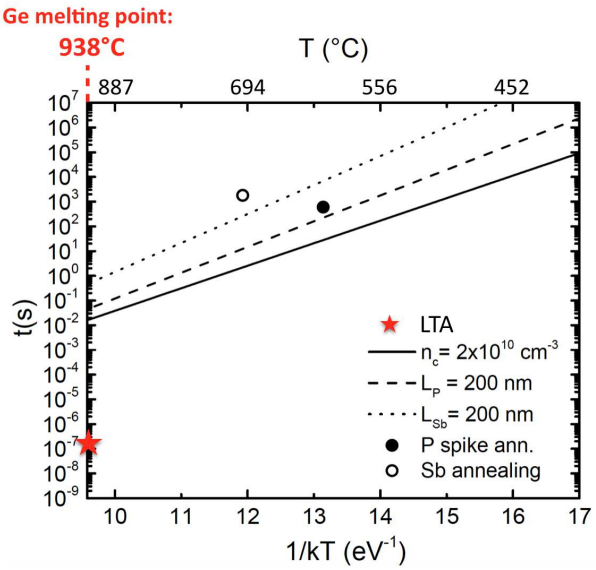

Figure 5.12. Plot reporting the annealing time as function of $(k_B T)^{-1}$. The three lines represent the thresholds for the diffusion of P, Sb and contaminants (dashed, dotted and continuous lines respectively). Full and empty points indicate the thermal budget of typical spike treatments for P and Sb doping. The red star indicates the thermal budget provided by a laser annealing treatment.

range reachable with a standard tube furnace, it is not possible to find an optimal thermal window. In fact, a thick P- or Sb- doped layer cannot be obtained without contaminating the bulk HPGe, since lines don't cross. Anyway, by working with shorter times thus moving more and more towards a state out-of-equilibrium, the physics of diffusion could change a bit allowing to achieve good dopant diffusion while keeping the impurity density below the established threshold. Thus, a

more rapid annealing technique that operates in the range of microseconds, such as flash lamp annealing (FLA) [116], could be more appropriate for these purposes. The situation would change completely by moving to Ge melting temperature (938 °C), which can be done through laser thermal annealing technique. In melt Ge, dopants diffuse order of magnitude faster than in solid, therefore the lines in Fig. 5.12 would not be true anymore. Besides, this technique acts just on the first hundreds of nanometers of material, leaving completely unheated the bulk. In this way, the process of bulk contamination should be almost null. We have had a first evidence of this by characterizing the n-type HPGe sample that had received LTA of sputtered Sb.

5.3 Conclusions

In this chapter we have presented the results of the characterization of some electrically active defects found inside HPGe, after high temperature annealing treatments in standard furnace. Through electrical measurements at low temperature, we measured the density of these doping defects and their sign. Their density turned out to be higher when high thermal budgets were applied and the shallow levels introduced are of acceptor type. The phenomenon has been studied in samples that had received different annealing treatments, different surface doping processes and also different surface treatments. Considered the evidence that active defects have an higher concentration in the first 10 micron of the surface, we supposed to be dealing with copper atoms coming from the external environment.
It is worth to note that both SOD and Sb doping can be exploited by keeping a level of contamination less than 10^{12} cm^{-3}. While this level is not suitable for gamma ray detectors that work at low temperature, it is clearly good for all other room temperature applications: since thermal carriers in Ge at 300 K are 2x10^{13} cm^{-3}, any doping below such value can not modify the carrier concentration of devices. On the other hand, bulk contaminant behaviour as recombination traps should be evaluated.
After having conceived a simple empirical model for the dependence of impurity density on the applied thermal budget, it was possible to fit data and an activation energy of 2.1$\pm$0.1 eV for the diffusion process was found. Through fitting of diffusion data, also data regarding P and Sb diffusion have been fitted finding activation energies of 2.4$\pm$0.1 and 2.7$\pm$0.1 eV respectively. With the knowledge of the activation energies, it was possible to set thresholds for minimum P and Sb diffusion and maximum bulk contamination, in order to find a possible thermal window for non-contaminating doping processes. However, in the range of temperatures

and times reachable with a standard tube furnace such a window of allowed thermal budgets doesn't exist. It is evident from our results that this optimal window should be sought for shorter times, entering a regime of strong out-of-equilibrium diffusion. Flash lamp annealing (FLA) and laser thermal annealing (LTA) could be suitable techniques to reach those conditions. A first evidence of LTA effectiveness has already been demonstrated in this thesis; it turns out to be the most promising and concrete perspective in order to renew and improve doping processes in HPGe materials.

Chapter 6

Preliminary diode prototype in HPGe

In chapters 3 and 4 we proposed various n-type doping techniques optimized for germanium, such as P diffusion in furnace from spin-on source, Sb diffusion in furnace from direct or remote sputtered sources and Sb out-of-equilibrium diffusion from a directly sputtered source by laser thermal annealing. Among all these techniques, in this chapter we have taken into account the one that proved to be more promising, that is laser thermal annealing on sputtered Sb, because it is characterized by a high level of electrical activation and, mostly, because it introduces a quasi-null amount of contaminant.
Our intent is to use this technique for manufacturing small scale diode prototype in HPGe. In previous chapters we tested the homogeneity and the electrical activation of doped layers through four-wire electrical measurement, but we do not have much information about the quality of the p-n junctions that are formed at the interface with bulk p-HPGe, for instance we don't know if a good rectifying behaviour is obtainable. For this reason we developed our prototype on a p-type HPGe in order to have the Sb doped contact responsible for the rectifying behaviour of the diode.
As a first prototype we used a very simple geometry and manufacturing, not optimized for the internal field and charge collection. Our intent was to be able to identify the reason of an eventual failure only in the doping process, and not in other part of the fabrication.
Therefore, starting from a square sample of a p-HPGe wafer, of 1 cm^2 area and 2 mm thickness, we have created a small diode, whose p^+ contact was made with a standard boron ion-implantation process, while the n^+ rectifying contact was done through laser thermal annealing of sputtered Sb. The n^+/p-HPGe/p^+ structure thus formed has been characterized by measuring its I/V characteristic at the temperature of $\sim$ 90 K to evaluate the rectifying behaviour.
Finally, this diode prototype has been placed under three calibrated radioactive

sources: ^{241}Am, ^{133}Ba and ^{152}Eu, in order to do a preliminary operation test as a gamma detector.

6.1 Experimental

6.1.1 Sample preparation

We started from one of the samples obtained from the p-type HPGe wafer, 2 mm thick, with growth impurity concentration in the range [0.4-2]x10^{10} cm^{-3}. The sample is a small square of 10x10 mm^2 area and 1.8 mm thickness; from the starting wafer $\sim$0.2 mm of material are lost because of the manual polishing.
For the fabrication of the diode prototype, we started from the creation of the p^+ contact. In a detector with p-type HPGe bulk, the role of the p^+ contact is to form an energy barrier against electron injection from the metal into the semiconductor. One one side of the square sample, the p^+ contact was created by a standard boron ion-implantation process, in a thickness of $\sim$150 nm. The n^+ rectifying contact was done on the other side, by laser thermal annealing on a directly sputtered Sb film. This doping technique was explained in detail in paragraph 4.1.2, here it is briefly summarized. With the help of a Kapton mask, a circular ultra-thin film of Sb ($\varnothing$=5

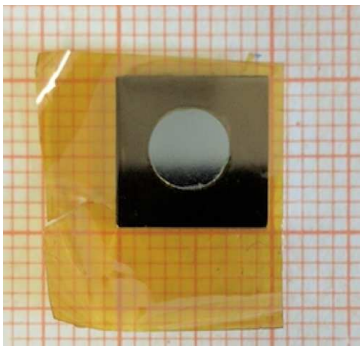

Figure 6.1. Sb/p-HPGe/B diode prototype photographed after Sb sputtering, before laser annealing.

mm and 2 nm thickness) was sputtered in the center of the sample surface, starting from a high-pureness target (99.999% with Cu content $\leq$0.01 ppm), see Fig. 6.1. As reported in Chapter 4, once determined the sputtering rate through RBS (13.3 nm min^{-1}), the 2 nm thickness film was obtained with a deposition time of 9 s. For the out-equilibrium diffusion a pulsed Nd:YAG solid state laser was used, characterized by 7 ns pulse duration and 10 Hz repetition rate. The laser light was in the UV range (355 nm) and the energy density deposited on the sample during the annealing treatment (which consisted in 1 pulse) was 300 mJ cm^{-2}. The laser spot was a

bit larger than the deposited Sb layer (6.2 mm diameter). The centering of the laser spot was made with an accuracy better than 0.5 mm, therefore the whole sputtered layer resulted to undergo the laser treatment.
Because of the particular front surface geometry, that is a square intrinsic surface with a small highly-doped central spot, it was not possible to build the electrode structure usually used for planar detector diodes (a central main electrode and a guard ring around, isolated by a trench). Hence, no metal pads were deposited on the sample front or rear surface. During measurements, the metal contact has been achieved on both sides by pressing the sample with foils of malleable indium.
A guard ring structure was performed to build trial diodes with phosphorous SOD process (see the appendix).
In this case instead, the small doped area does not allow to implement that scheme and the passivation of the intrinsic surface was a fundamental step. It was carried out by dipping the sample in the HNO_3(65%):HF(40%) 3:1 solution for 20 s and quenching the etching reaction with methanol. The acid dipping causes the erosion of about 2 microns that would be enough to remove both the Sb and B doped regions. In order to protect these zones, Kapton adesive tape pads were applied to the doped regions: a circular pad of 5 mm was applied on the front Sb contact while the whole back B surface was covered during passivation. Therefore, all the 1.8 mm thick lateral sides and a "square corona" on the front face undergo the passivation process.
After that, the diode prototype was ready for the electrical characterization.

6.1.2 Measurement setup for diode and detector characterizations

The same apparatus was used to test the operation of this prototype, first as a diode and then as a gamma detector. For both the measurements, the sample was mounted in a commercial standard cryostat (Fig. 6.2a) inside an Al chamber under vacuum. The sample is cooled to $\sim$90 K. The LN2 tank (not shown) is located above the Al chamber and cold is transmitted by a Cu finger put in contact with the indium foil that is above the sample. In fact, a 1.0 mm thick indium foil was inserted between each side of the diode and electrodes, in order to improve the electrical contact.
In order to test the diode operation, through a Keithley sourcemeter the sample was reversely and directly biased and the I/V characteristic was measured. Dealing with a small diode, just 2 mm thick, it was sufficient to apply a low voltage $<$40 V to completely deplete the junction. For the determination of the detector properties, the diode must be reversely biased to be completely depleted. Standard calibration

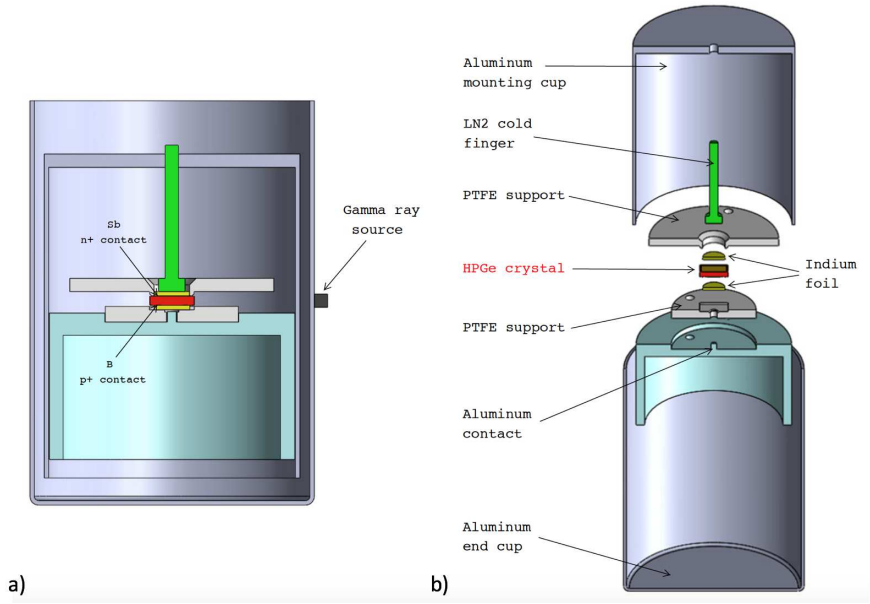

Figure 6.2. Layout scheme of the cryostat and supports of the HPGe crystal. Inside the Al chamber, the HPGe diode is supported by PTFE (Teflon) pieces, to ensure electrical isolation. When needed, the calibrated gamma source is put on the side of the detector.

gamma sources of ^{241}Am (59.54 keV), ^{152}Eu and ^{133}Ba were placed as close as possible to the lateral side of the detector, just outside the Al chamber (as shown in the right scheme). In this way, the absorbing material thickness between source and detector is minimized (just 1 mm Al for the mounting cap and 1 mm Al for the end cap). NIM electronics was used for the detector measurements.
All the detector properties were measured by using the ^{241}Am source, while the other two sources were used for the energy calibration.

6.2 Results

Firstly, we measured the chemical concentration profile of Sb atoms and B atoms through Secondary Ion Mass Spectrometry (SIMS), naturally on test samples different from the final prototype in order to preserve it. After that, using other two test samples, the electrical activation of the two contacts was characterized through four-point probe measurements (all results were reported in paragraph 4.2.3 for antimony, and paragraph 2.4.4 for boron). Regarding the Sb layer, we estimated an active concentration in the range (4.0-9.3)x10^{20} cm^{-3}, while in case of B the active concentration resulted about 5.8x10^{18} cm^{-3}.

6.2.1 I/V diode characterization

Once characterized all the properties of the two highly-doped contact layers, an investigation of the n^+-pHPGe junction was necessary. A good junction should be easily rectified and characterized by a very low reverse current and no leakage.
For this kind of characterization also a replica of this prototype was tested, in order to evaluate the reproducibility of the junction.
Figure 6.3 shows the I/V characteristic of the diode prototype, measured at 90 K (the operation temperature of gamma detectors, at which intrinsic carriers are cooled). Since a gamma detector should be characterized by a reverse current lower than 0.5-1 nA (the best being few tens of pA), in order to be sensitive to γ-ray signals, we were particularly interested in the measurement of the reverse current in our diode prototype. The red point is a current value measured in forward bias and, as expected, it is very high. Black symbols, instead, correspond to the reverse current and it is really low. Therefore we are dealing with a typical diode characteristic, due to the successful formation of a n^+-p junction. The reverse current is very low (below 5 pA) until 10 V, then it slowly increases still keeping low values until 20 V (less than 30 pA) and afterwards it continues to increase reaching 1 nA at about 35 V.

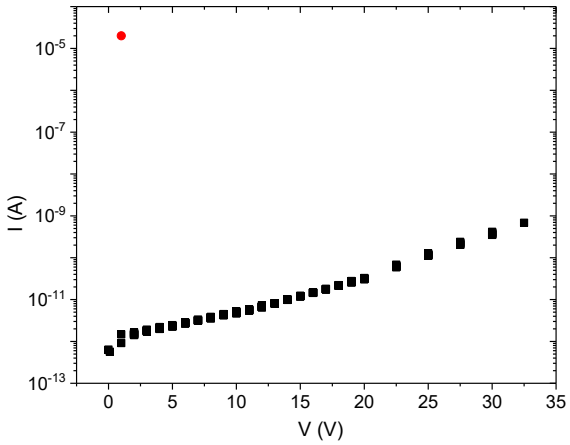

Figure 6.3. I/V characteristic of the Sb-doped diode prototype.

Now, several considerations must be done. First, we calculated the depletion voltage required to remove all free charge carriers from the HPGe side of the flat junction (which is ∼1.8 mm thick), by using the following formula already cited in chapter 1.

$$V_d = \frac{eNd^2}{2\varepsilon} \tag{6.1}$$

In chapter 5, for the laser annealing process an impurity density N equal to 1.7x10^{10} cm^{-3} was measured. This number is in the range of possible growth impurity concentration, as given by the producer specifications (less than 2x10^{10} cm^{-3}). It is worth to note that 1.7x10^{10} cm^{-3} was obtained after 4 laser processes at the 4 corner, therefore, a possible contamination due to laser (if any) may be increased by a factor of 4 with respect to a sample with a single laser process (as this prototype). The n-type reference sample, coming from the same starting wafer, was measured to have a contamination content of $\sim$1x10^{10} cm^{-3}.
These reasonings let us conclude that the n-type impurity density of the present sample may be reasonably in the following range: (1<N<1.7)x10^{10} cm^{-3}. These levels correspond to voltages within (20-34)V in order to fully deplete a perfectly planar structure. A contamination measurement exactly on the tested diode would improve the knowledge of such parameter and is planned for the near future. In this range, the reverse current is between 10 pA and 1 nA.
Anyway, the result is optimum if we consider the fact that there isn't any guard ring, so we are blocking the surface leakage just with the chemical passivation. Moreover, the particular shape of passivated surface and of the n contact, together with the presence of sharp edges, suggests that the electrical field along the surface could vary discontinuously by increasing the voltage. This could explain the increase of the current until 1 nA. In order to improve these aspects, a second prototype with a guard ring and a more smooth shape will be produced. Results also mean that the Sb-contact provides an effective energy barrier against hole injection from the metal into the semiconductor, since the leakage is not high also at full depletion.
In order to verify the reproducibility of the junction behaviour, the same characterization was done on a replica of this prototype. In Fig. 6.4 the I/V characteristics from 0 and 20 V of both samples are reported, for comparison. During a first measurement, the replica showed a higher reverse current (1 nA at 20 V, blue curve). After, it underwent a second procedure of intrinsic surface passivation and then it was measured again. In this case, a low reverse current almost identical to that of the first diode prototype was seen ($\sim$10 pA at 20 V, black curve). For completeness, in Fig. 6.5 the I/V characteristic of the replica up to 40 V is plotted. In the expected depletion range (20-34 V), the reverse current is between 10 pA and 1 nA, exactly as the first prototype.
These result is very important because it confirms the fundamental role of intrinsic surface passivation and, mostly, it proves the reproducibility of the Sb/p-HPGe/B junction.

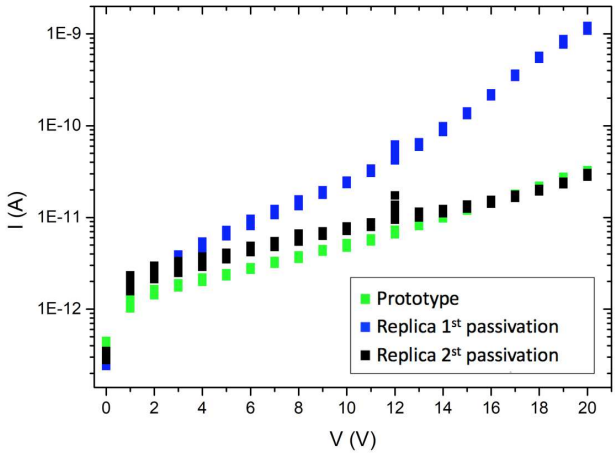

Figure 6.4. The I/V characteristic of the diode prototype is reported again, in green. While the blue and the black curves are the characteristics of the replica, from 0 to 20 V, respectively after the 1^{st} and the 2^{nd} passivation.

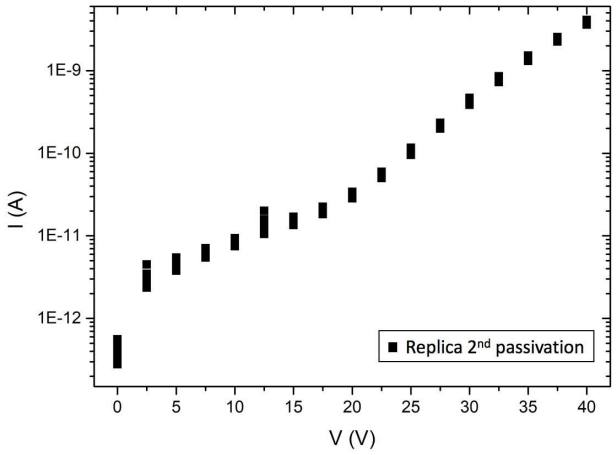

Figure 6.5. Complete I/V characteristic of the replica from 0 to 40 V.

6.2.2 Detector operation test

The operation and the properties of our diode prototype as a radiation detector were investigated using three calibrated gamma sources: ^{241}Am, ^{133}Ba and ^{152}Eu. When we put the sample, reversely biased at low voltage values, under the ^{241}Am source and we saw the characteristic gamma peak, we realized that the small diode prototype did operate as a gamma detector.
After the first measurement, we carried out a study on the variation of the photopeak integral and energy resolution as function of the applied voltage, in the range 0-20 V. Results are shown in Fig. 6.6. The integral was calculated after background subtraction and normalization to the acquisition live time. As can be seen, the in-

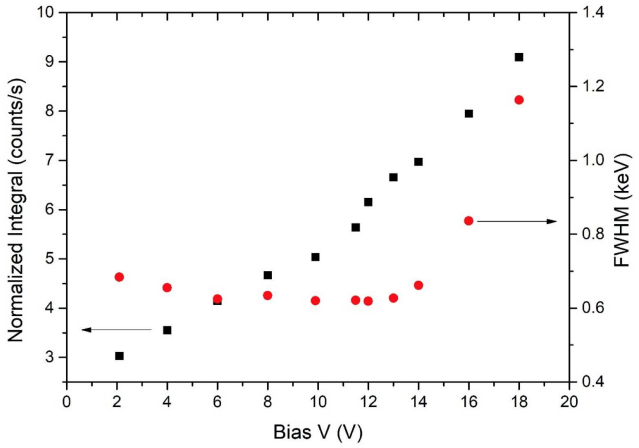

Figure 6.6. ^{241}*Am photopeak integral and energy resolution as a function of the applied bias voltage.*

tegral is steadily increasing with the bias voltage, sign that the depleted volume is still increasing. Also the energy resolution shows a dependence on the applied voltage, ranging from 0.62 (at 12 V) to 1.16 keV (at 18 V). The lowest resolution value, obtained at 12 V, is 0.62 keV and this is really an optimum result. A further increase of the bias voltage gives rise to an increase of the noise and to a drift of the baseline, which make the energy resolution rapidly worse. This worsening probably arises when the intensity of the electric field starts to become significant also in the regions close to the intrinsic lateral surface and near the detector corners. In fact we have to take into account the unusual and irregular shape of this diode, characterized by a small n^+ spot at the center of the front side with intrinsic surface all around. In Ref. [48] it is demonstrated that passivated intrinsic surfaces generate a dead layer below them. As it is known, dead layers negatively influence the charge collection thus affecting also the energy resolution. To conclude the analysis of Fig. 6.6, it should be said that with this irregular geometry, the full depletion and maximum counting rate are achieved to the detriment of the energy resolution. This is another strong reason to continuing the research in order to apply the process to more conventional geometries.

For the collection of definitive gamma spectra of ^{241}Am, ^{133}Ba and ^{152}Eu sources, the reverse bias voltage of 12 V was chosen, which is a good compromise between high counting rate and optimum energy resolution. In Fig. 6.7, we report all the spectra, which have also been used for determining the energy calibration. The spectra show that the detector is capable to measure the gamma rays emitted by the three sources with energy up to 383.85 keV, corresponding to the transition line of ^{133}Ba. Only the higher-energy gamma rays of ^{152}Eu above 400 keV (not shown in the Figure) cannot

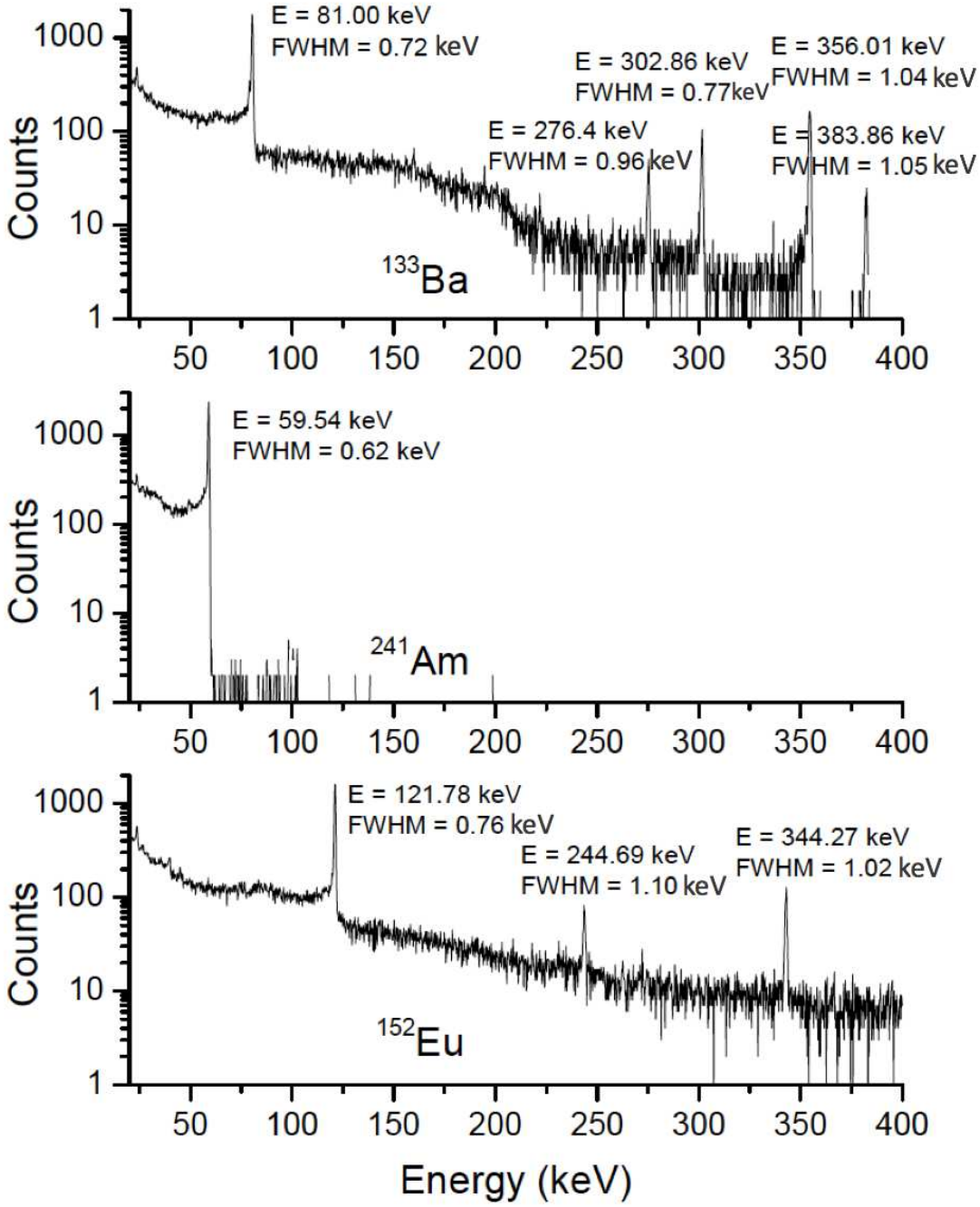

Figure 6.7. Gamma spectra of ^{241}Am, ^{133}Ba and ^{152}Eu.

be detected maybe because of their very low intensity. It is noteworthy that even for the higher energy peaks the energy resolution keeps good, as can be appreciated.

6.3 Conclusions

A new method for the n^+ contact formation in a HPGe diode was successfully applied. A first diode prototype, characterized by irregular geometry but optimum rectifying capability has been created and tested. A reverse current of $\sim$10 pA at 20 V and $\sim$1 nA at 34 V, was measured. This values were confirmed by the measurement done on a replica of the prototype. The quality of intrinsic surface passivation turned out to be crucial.
For what concerns the operation of this diode prototype as a radiation detector, a reverse current ranging from the pA to the nA was measured in the interval of bias voltages 20-32 V, within which a full depletion is expected. The result is very good considering the fact that there isn't any guard ring, so we are counteracting the surface leakage just with the chemical passivation of intrinsic surfaces. Moreover, this result also means that the junction leakage is very low even at full depletion, thus the Sb-contact provides an effective energy barrier against hole injection from the metal into the semiconductor.
After this outcome the diode was reversely biased and put under three calibrated sources: ^{241}Am, ^{133}Ba and ^{152}Eu. With the americium source, a study of the variation of the photopeak integral and energy resolution as functions of the applied voltage was done. A really optimum value of 0.62 keV, for the energy resolution of the 59.4 keV photopeak was measured at about 12 V. This optimal voltage, corresponding to the best energy resolution and intermediate counting rate was chosen, even though it didn't allow a full depletion of the diode, and definitive gamma spectra for all the three sources were collected. This preliminary detector prototype exhibited a very good energy resolution even at the higher gamma-ray energies (300-400 keV).
All the key parameters for the operation of this structure as a diode and as a detector, that are reverse current, depletion voltage and charge collection, are subject to the field line distortion which occurs near the upper corners of this particular geometry. Therefore, a more standard planar structure with guard ring (as the one described in appendix) should be fabricated and tested. Before doing this, a further development is needed to scale the process to a larger size or alternatively lithographic procedures should be adopted for implementing guard ring and segmentation on small dimensions.
These perspectives open the route for further tests and investigations that will go

beyond the purpose of the present thesis.

Conclusions

In this thesis, equilibrium and out-of-equilibrium n-type doping processes have been developed on Ge and HPGe. An electrical characterization of contaminant shallow doping defects induced inside HPGe bulk after thermal processes has been performed, followed by a data analysis carried out through an empirical model and useful for defect identification. In the last part, a preliminary diode prototype in HPGe is fabricated by implementing Sb diffusion by laser thermal annealing doping technique. Its diode characteristic has been measured and it was also tested as a gamma detector.

Phosphorus Spin-On Diffusion (SOD) technique was already documented in the literature, with various papers devoted to Si doping. For Ge, the process protocol and final characterization were incomplete. In this thesis the process has been widely experimented on Ge and, with the help of many characterization steps, a clear experimental protocol was defined, leading to optimum Ge surface quality, tunable thickness (200 nm - 1μm) high doping level (5x10^{19} cm^{-3}) and full electrical activation. This technique, whilst showing good results also on HPGe in terms of doping parameters, has proven to be unsuitable for the fabrication of gamma detectors. Spike thermal annealing in standard furnace promotes the diffusion of doping impurities inside the underlying HPGe bulk, affecting its pureness. This technology could be favourably employed on microelectronic grade Ge for applications requiring highly-doped junctions, such as multijunction solar cells and photonic devices.

Equilibrium Sb (another group V n-type dopant) diffusion from a pure sputtered thin film is an innovative approach. This approach is interesting for two reasons. First, sputtering sources can be alternative to ion implantation that is more expansive and may induce huge damage due to the heavy mass of Sb. Secondly, with respect to HPGe, Sb sputtering sources are available at very high purity reducing in principle the risk of contamination. It was shown that the direct sputtering of a 20 nm source over Ge causes the formation of relatively large surface defects, during the following annealing. We discovered that this can be avoided when the sputtered Sb source is moved at a distance of 8.5 mm over Ge surface, by using a Si sample

with a sputtered Sb layer as a remote source. In this case, surface damages due to the formation of $GeSb_x$ interphase nanograins, didn't occur. Surface was mirror-like and a homogeneous doped layer was formed, with a low maximum concentration (1.2x10^{18} cm^{-3}) and 150 nm thickness.
When tested on HPGe, also this equilibrium diffusion technique has proven to induce doping impurity diffusion inside the HPGe bulk. Contamination does not occur specifically for the presence of Sb, but occurs due to the furnace annealing process. It is worth to note that both SOD and Sb doping can be exploited by keeping a level of contamination less than 10^{12} cm^{-3}. While this level is not suitable for gamma ray detectors that work at low temperature, it is clearly good for all other room temperature applications: since thermal carriers in Ge at 300 K are 2x10^{13} cm^{-3}, any doping below such value can not modify the carrier concentration of devices.
From the electrical characterization of shallow doping defects induced inside HPGe bulk after doping processes, it was found that these defects are of acceptor type and their density is higher close to surfaces. By analysing data through an empirical model it was demonstrated that defect diffusion is induced by high thermal budget annealings and a single value of activation energy was found, equal to 2.1$\pm$0.1 eV. All evidences leads to the confirmation of the hypothesis that shallow acceptor levels are due to copper contamination, coming not necessarily from the furnace but also from the external environment.
By calculating also the activation energy for P and Sb solid diffusion in Ge, it was also shown that performing an equilibrium diffusion of P or Sb in HPGe without inducing Cu contamination of the bulk is extremely difficult, if not impossible. Anyway, it is evident from results that optimal diffusion treatments should be sought for shorter times, entering a regime of strong out-of-equilibrium diffusion. Flash lamp annealing (FLA) and laser thermal annealing (LTA) could be suitable techniques to reach those conditions.
In order to enhance Sb diffusion from an ultra-thin film (of just 2 nm) directly sputtered on HPGe, laser thermal annealing was used. The UV irradiation of one laser pulse (7 ns duration) melts only the first 150 nm of HPGe, by taking it at least to 938.2 °C. In molten HPGe, the physics of diffusion changes and dopants liquid diffusivity, which is about seven orders of magnitude higher than the solid one, is exploited. The very thin layer and fast process avoid the formation of defects, an optimum quality surface and a sharp diffusion profile were obtained, the latter characterized by a maximum concentration of 2.5x10^{21} cm^{-3} and a thickness of 35$\pm$5 nm. Through preliminary electrical measurements, done on an irregular sample geometry, an estimate of the electrical activation was done. An active dose between 20% and 50% of

the total chemical dose of Sb atoms was obtained, corresponding to an active carrier concentration in the range (4.0-9.3)x10^{20} cm^{-3}, well over the Sb solid solubility in Ge. This results is very interesting not only for gamma-ray application.
The high doping level, in further investigations, may be interesting for other applications (plasmonic sensors, lasers). Moreover, to our knowledge, this is the first time that germanium is doped by combination of surface film deposition and laser annealing, while usually an ion implantation step is performed with higher cost and process complexity. Since the contamination test showed that laser annealing affects to a minor extent the purity of HPGe, all these properties made it a good candidate for Li substitution in HPGe devices.
A preliminary proof of LTA effectiveness has been demonstrated in this thesis, with the fabrication of a small detector prototype 1.8 mm thick and 10x10 mm large. Once cooled at 90 K and placed under ^{241}Am, ^{133}Ba and ^{152}Eu sources, it exhibited an optimum energy resolution of 0.62 keV for the 59.4 keV photopeak of ^{241}Am, and very good resolutions even at higher gamma-ray energies of 300-400 keV for ^{133}Ba and ^{152}Eu sources.
The results presented in this work represent a step forward in the research of innovative doping methods for Ge. As well as they provide a new technological approach for the n-type contact formation in HPGe gamma detectors.
Future perspectives include both a deeper physical understanding of Sb incorporation during LTA of a deposited source and investigations of many technological aspects, in order to allow the implementation of Sb LTA technique on more standard detector geometries. About the first point open questions are: Why not all Sb is active? Is it possible to improve it? What is the stability of such dopant? The last question is crucial for application but it is also a fundamental aspect dealing with the fact that out-equilibrium processes often produce metastable structures.
About the technological implementation in gamma detectors the outstanding issues are: the coverage of large areas, since it is not known what happens by overlapping two or more laser spots on Ge surface; the choice and the effects of metal pads on this kind of n-contact, since we just tested indium pads, not deposited metal layers; the effects of radiation-damage recovery annealing on the shape of the Sb concentration profile (this is of course connected to the stability of the contact mentioned above). Moreover, given the simplicity and affordability of this doping method, the study of p-type doping by LTA of an Al source is ongoing.

Appendix

P/p-HPGe/B diode prototype

The diode structure matter of this appendix was created to test the rectifying properties of the n^+-type contact done by P spin-on diffusion on a p-HPGe substrate. On the other side of the sample, the ohmic contact was formed with ion implantation of boron, thus obtaining an n^+/p-HPGe/p^+ structure. A CrAu guard ring was sputtered on the B-doped side.
In chapter 5 it was proved that P spin-on diffusion introduces about 2x10^{11} cm^{-3} of p-type contaminants inside the underlying HPGe bulk, with the treatment up to 610 °C for 10 min. Thus, this doping technique can not be aimed at gamma detection. Anyway, a study of its rectifying properties could be interesting for other applications.

Experimental

For the fabrication of the structure, we started from a p-type HPGe square sample, 1.8 mm thick and of 1 cm^2 area, and as first we created the p^+ contact. This contact was done on one side of the sample by a standard boron ion-implantation process, in a thickness of ∼150 nm. See paragraph 2.4.4 for the results of SIMS and electrical measurements done on this B-implanted layer.
The n^+ contact was done on the other side with respect to the B-implanted one. It was created by spin-on diffusion of phosphorus. The technique had already been described in detail in paragraph 3.1, so here it will be briefly recalled. Before spinning the P-containing precursor, the lateral surface of the sample was covered with Kapton adhesive, in order to protect it and the rear B-implanted side. Then the source was deposited by spin-coating, forming a thin film that was cured at 130 °C for 30 minutes, in N_2 flux at the 10% of relative humidity. After that, the sample was capped on both sides with Si, the whole clamped between two quartz slides and it was spike-annealed up to 610 °C in 10 minutes. Finally, after slow cooling, the P source film was removed through a dipping in HF 10%.
Through SIMS the P concentration profile was measured. It is reported in Fig.

8, together with the profile of a layer produced with the same technique in a conventional microelectronic Ge substrate (n_{growth} $\sim 10^{16}$ cm^{-3}). They look equal, thus P spin-on doping technique doesn't give unexpected results on HPGe.

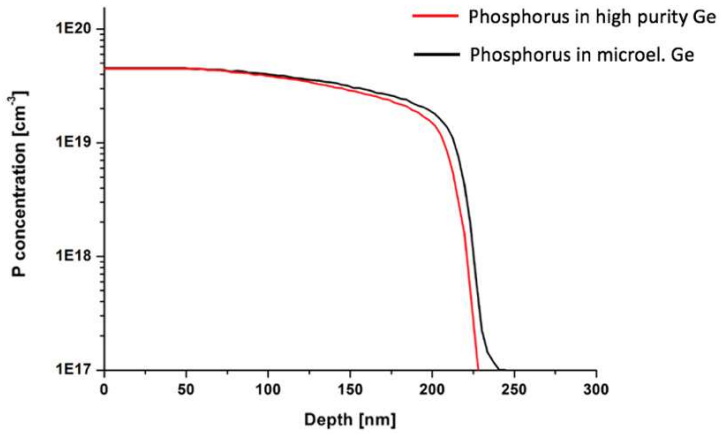

Figure 8. SIMS concentration profiles of phosphorus diffused at equilibrium from spin-on doping sources in an HPGe sample and in a standard Ge sample.

After the formation of the two contacts, CrAu electrodes were deposited on the B-implanted side by sputtering: a central circular electrode and a guard ring around, shown in Fig 9a. The guard ring is an electrode that during the measurement of a diode characteristic is kept at the same potential as the central electrode. It has the role to collect the current flowing along the lateral intrinsic surface, in order to separate this contribution from that actually passing through the p-n junction.
After CrAu sputtering, the final steps for the fabrication of the structure were: the digging of a trench between the central pad and the guard ring, in order to interrupt the underlying B-doped layer and isolate the two electrodes; the chemical passivation of the lateral intrinsic surface to minimize surface currents. The latter process is not fundamental when using a guard ring electrode, but we did it to be on the safe side. Through a wet chemical etching in HNO_3(65%):HF(40%) 3:1 solution for 20 s, the B-layer was digged and with a rapid quenching of the etching in methanol, also the passivation of surfaces was carried out.
The measurement setup used for diode characterization has been described in paragraph 6.1.2.

Results

In Fig. 9b, a schematic representing a section of the diode is reported. The

back contact was easily done while inserting the diode in the measurement setup, by placing an indium foil between the rear side of the sample and the metal support of the instrument.

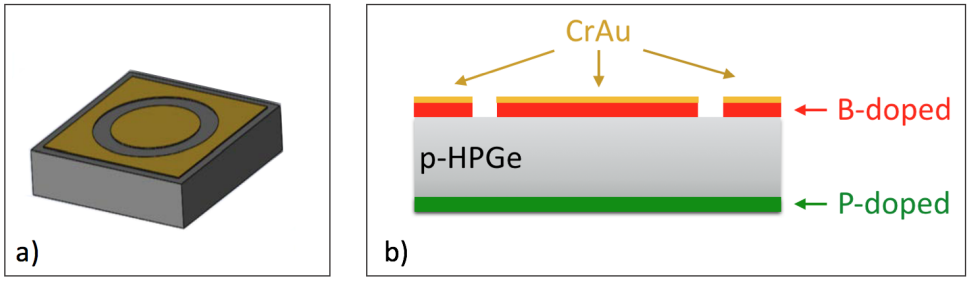

Figure 9. P/p-HPGe/B diode prototype. a) 3D schematic of the diode. The central electrode and the guard ring, both in CrAu, are visible. b) A section of the diode.

Reverse bias was applied between the central CrAu pad (on p^+ contact) and the indium foil (on n^+ contact). Then, reverse current was measured on both the front CrAu electrodes: the central pad and the guard ring. Results are plotted in Fig. 10. In the graph, there is, in red, the reverse current measured between the central

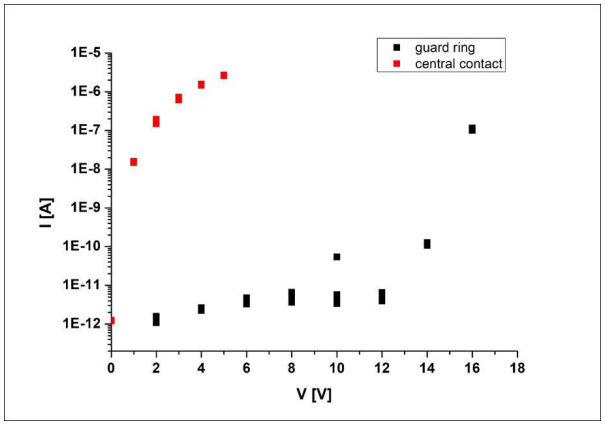

Figure 10. Reverse bias I/V characteristic for the diode prototype with the P-doped n^+ contact. The current measured between the guard ring and the back contact (in black) is very low for a few volts but then it increases rapidly.

CrAu pad and the back contact of the diode while, in black, the reverse current measured between the guard ring and the back contact. The first (central-back) is really high, on the order of μA; while the second current (guard-back) is very low until 8V, about 10 pA, but then it increases very rapidly due to some leakage.
Probably, regarding the central region of the diode volume, some defects have seriously damaged the junction and they act as leakage points for the current

collected at the central electrode. Actually, looking at the sample rear side with scanning electron microscopy, a marked accidental scratch was visible in the central part (Fig. 11). For what concerns the reverse current measured between the guard ring and the back contact, its rapid increase over 8 V could be the result of a mixing with the high leakage current flowing in the central zone of the diode.
In conclusion, this I/V characterization shows that n^+ Ge layers, produced by P spike annealing from spin-on-doping sources, can form rectifying junctions characterized by low reverse current, about 10 pA until 8 V.

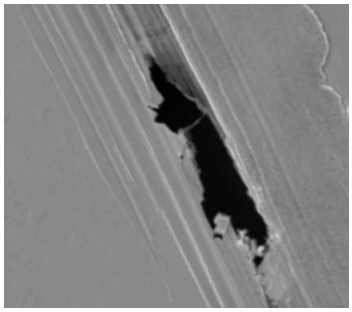

Figure 11. SEM image of a marked accidental scratch found in the center of the rear side of the sample, where there is the P-diffused contact. This scratches could have damaged the junction, being the cause of high leakage.

List of publications

1. **Optimal process parameters for phosphorus spin-on-doping of germanium**
   V. Boldrini, S.M. Carturan, G. Maggioni, E. Napolitani, D.R. Napoli, R. Camattari, D. De Salvador
   Applied Surface Science 392 (2017) 1173

2. **Diffusion doping of germanium by sputtered antimony sources**
   G. Maggioni, F. Sgarbossa, E. Napolitani, W. Raniero, V. Boldrini, S.M. Carturan, D.R. Napoli, D. De Salvador
   Materials Science in Semiconductor Processing 75 (2018) 118-123

3. **New developments in HPGe detectors for high resolution detection**
   D.R. Napoli, G. Maggioni, S. Carturan, J. Eberth, V. Boldrini, D. De Salvador, E. Napolitani, P.Cocconi, G. Della Mea, M. Gelain, R. Gunnella,M.G. Grimaldi, M. Loriggiola, G. Mariotto, N. Pinto, W. Raniero, S.J. Rezvani, S. Riccetto, D. Rosso, F. Sgarbossa, S. Tati
   Acta Physica Polonica B 48 (2017) 387

4. **Electrical Activation Measurements on Ge Doped by Spin-On Diffusion**
   V. Boldrini, S. Carturan, L. Gastaldello, G. Maggioni, D. De Salvador, E. Napolitani, D.R. Napoli
   INFN-LNL Annual Report (2015) 112

References

[1] L. Łukasiak, A. Jakubowski
History of semiconductors
Journal of Telecommunications and Information Technology 1 (2010) 3-9

[2] S. Bidwell
On the Sensitiveness of Selenium to Light, and the Development of a similar Property in Sulphur
Proceedings of the Physical Society of London 7 (1885)

[3] B. Gudden
Electrical conductivity in semi-conductors
Phys. Med. Soz. Erlangen 62 (1930) 289

[4] J.R. Woodyard
Nonlinear circuit device utilizing germanium
U.S. Patent 2,530,110 (1950)

[5] M. Sparks
Method of Making P-N Junctions in Semiconductor Materials
U.S. Patent 2,631,356 (1953)

[6] *November 17 - December 23, 1947: Invention of the First Transistor*
APS News 9 (2000) 2

[7] K. Kita et al. *Control of high-k/germanium interface properties through selection of high-k materials and suppression of GeO volatilization*
Applied Surface Science 254 (2008) 6100-6105

[8] M.D. McDaniel et al. *Atomic layer deposition of crystalline SrHfO3 directly on Ge (001) for high-k dielectric applications*
Journal of Applied Physics 117 (2015) 054101

[9] A. Chroneos et al. *Implantation and diffusion of phosphorous in germanium*
Materials Science in Semiconductor Processing 9 (2006) 640-643

[10] P.S Goley and M.K. Hudait *Germanium Based Field-Effect Transistors: Challenges and Opportunities*
Materials 7 (2014) 2301-2339

[11] C. Claeys and E. Simoen *GERMANIUM-BASED TECHNOLOGIES From Materials to Devices*
2007 Elsevier

[12] J.Y.J. Lin et al. *Increase in current density for metal contacts to n-germanium by inserting TiO_2 interfacial layer to reduce Schottky barrier height*
Appl. Phys. Lett. 98 (2011) 092113

[13] T.H. Loh et al. *Selective epitaxial germanium on silicon-on-insulator high speed photodetectors using low-temperature ultrathin $Si_{0.8}Ge_{0.2}$ buffer*
Appl. Phys. Lett. 91 (2007) 073503

[14] D. Ahn et al. *High performance, waveguide integrated Ge photodetectors*
Opt. Exp. 15 (2007) 3916-3921

[15] C. Wang et al. *High-Performance Ge p-n Photodiode Achieved With Preannealing and Excimer Laser Annealing*
IEEE PHOTONICS TECHNOLOGY LETTERS 27 (2015) 1485-1488

[16] M.E. Kurdi et al. *Band structure and optical gain of tensile-strained germanium based on a 30 band k•p formalism*
Journal of Applied Physics 107 (2010) 013710

[17] T.K.P. Luong et al. *Making germanium, an indirect band gap semiconductor, suitable for light-emitting devices*
Adv. Nat. Sci.: Nanosci. Nanotechnol. 6 (2015) 015013

[18] J. Liu et al. *Tensile-strained, n-type Ge as a gain medium for monolithic laser integration on Si*
Opt. Express 15 (2007) 11272-11277

[19] L. Guangyang et al. *Strong electroluminescence from direct band and defects in Ge n^+/p shallow junctions at room temperature*
Appl. Phys. Lett. 108 (2016) 191107

[20] R.E. Camacho-Aguilera et al. *An electrically pumped germanium laser*
Opt. Express 20 (2012) 11316-11320

[21] L. Carroll et al. *Direct-Gap Gain and Optical Absorption in Germanium Correlated to the Density of Photoexcited Carriers, Doping, and Strain*
Phys. Rev. Lett. 109 (2012) 057402

[22] S. Wirths et al. *Lasing in direct-bandgap GeSn alloy grown on Si*
Nature Photonics 9 (2015) 88-92

[23] A. Kitai *Principles of Solar Cells, LEDs and Diodes*
John Wiley & Sons, Ltd (2011)

[24] P. Pichler
Intrinsic Point Defects, Impurities, and Their Diffusion in Silicon
Springer-Verlag Wien GmbH 2004

[25] S.M. Hu
Nonequilibrium point defects and diffusion in silicon
Mater. Sci. Eng. Rep. 13 (1994) 105-192.

[26] M. Mastromatteo
PhD Thesis "Mechanism of fluorine redistribution and incorporation during solid phase epitaxial regrowth of pre-amorphized silicon
Università degli Studi di Padova

[27] R.J.D. Tilley
Defects in solids
John Wiley & Sons, Inc (2008)

[28] H. Bracht
Copper related diffusion phenomena in germanium and silicon
Materials Science in Semiconductor Processing 7 (2004) 113-124

[29] S. Brotzmann, H. Bracht
Intrinsic and extrinsic diffusion of phosphorus, arsenic, and antimony in germanium
Journal of Applied Physics 103 033508 (2008)

[30] E. Bruno et al.
Mechanism of B diffusion in crystalline Ge under proton irradiation
Phys. Rev. B 80 (2009) 033204

[31] S. Mirabella et al.
Mechanisms of boron diffusion in silicon and germanium
Journal of Applied Physics 113 (2013) 031101

[32] F.A. Trumbore
Solid Solubilities of Impurity Elements in Germanium and Silicon
THE BELL SYSTEM TECHNICAL JOURNAL (1960)

[33] V.I. Fistul
Impurities in Semiconductors: Solubility, Migration, and Interactions
CRC Press, Florida (2004) pg. 157

[34] J. Vanhellemont and E. Simoen
Brother Silicon, Sister Germanium
J. Electrochem. Soc. 154 (2007) H572

[35] R. Milazzo
DOPING OF GERMANIUM BY ION-IMPLANTATION AND LASER ANNEALING IN THE MELTING REGIME
Università degli Studi di Padova (2015)

[36] E. Bruno et al.
High-level incorporation of antimony in germanium by laser annealing
Journal of Applied Physics 108 (2010) 124902

[37] G. Thareja et al.
High n-Type Antimony Dopant Activation in Germanium Using Laser Annealing for n^+/p Junction Diode
IEEE Electron Device Letters 32 (2011)

[38] G. Impellizzeri et al.
B activation and clustering in ion-implanted Ge
Journal of Applied Physics 105 (2009) 063533

[39] R. Milazzo et al.
N-type doping of Ge by As implantation and excimer laser annealing
Journal of Applied Physics 115 (2014) 053501

[40] *http://staff.orecity.k12.or.us/les.sitton/Nuclear/The%20Momentum%20of%20a%20Photon%2*

[41] G.F. Knoll *Radiation Detection and Measurement*
John Wiley & Sons. Inc. (2000)

[42] K.S. Krane *Introductory Nuclear Physics*
John Wiley & Sons. Inc. (1988)

[43] J. Eberth, J. Simpson
From Ge(Li) detectors to gamma-ray tracking arrays - 50 years of gamma spectroscopy with germanium detectors
Progress in Particle and Nuclear Physics 60 (2008) 283-337

[44] W.L. Hansen
High-purity germanium crystal growing
Nuclear Instruments and Methods 94 (1971) 377-380

[45] Z. He
Review of the Shockley-Ramo theorem and its application in semiconductor gamma-ray detectors
Nuclear Instruments and Methods in Physics Research A 463 (2001) 250-267

[46] C. Fleischmann et al.
Impact of ammonium sulfide solution on electronic properties and ambient stability of germanium surfaces: towards Ge-based microelectronic devices
Journal of Materials Chemistry C 26 (2013)

[47] P.W. Loscutoff, S.F. Bent
Reactivity of the germanium surface: Chemical passivation and functionalization
Annual Review of Physical Chemistry 57 (2006) 467-495

[48] G. Maggioni et al.
Characterization of different surface passivation routes applied to a planar HPGe detector
Eur. Phys. J. A 51 (2015) 141

[49] http://ns.ph.liv.ac.uk/research_centres.html

[50] Website: http://nucalf.physics.fsu.edu/ riley/gamma/gamma3.html

[51] https://www.agata.org/

[52] S. Paschalis et al.
The performance of the Gamma-Ray Energy Tracking In-beam Nuclear Array GRETINA
Nuclear Instruments and Methods in Physics Research A 709 (2013) 44-55

[53] https://nau.edu/cefns/labs/electron-microprobe/glg-510-class-notes/instrumentation/

[54] J.I. Goldstein et al.
Scanning Electron Microscopy and X-Ray Microanalysis
New York: Plenum Press (1981)

[55] J.I. Goldstein et al.
Scanning electron microscopy and x-ray microanalysis
Springer (2003)

[56] S.M. Sze
Semiconductor devices physics and technology
John Wiley & Sons (2002)

[57] F. Keywell and G. Dorosheski
Measurement of the Sheet Resistivity of a Square Wafer with a Square Four-Point Probe
Review of Scientific Instruments 31 (1960)

[58] L.J. Van der Pauw
A method of measuring the resistivity and Hall coefficient of lamellae of arbitrary shape
Philips technical review 20 (1958/59)

[59] L.J. Van der Pauw
A method of measuring specific resistivity and Hall effect of discs of arbitrary shape
Philips research reports 13 (1958)

[60] R. Nipoti et al.
Conventional thermal annealing for a more efficient p-type doping of Al^+ implanted 4H-SiC
J. Mater. Res. 28 1 (2013) 17

[61] K. Seeger
Semiconductor Physics: An Introduction
Springer (1973)

[62] S. Mirabella et al.
Activation and carrier mobility in high fluence B implanted germanium
Appl. Phys. Lett. 92 (2008) 251909

[63] V.M. Babich et al.
Ukrain Fiz. Zhumal (1969) 418
in: http://www.ioffe.ru/SVA/NSM/Semicond/Ge/electric.html#Hall

[64] R. Chwang et al.
Contact size effects on the Van der Pauw method for resistivity and Hall coefficient measurement
Solid State Electron. 17 (1974) 1217

[65] M.A. Green and M.W. Gunn
The evaluation of geometrical effects in fur point probe measurements
Solid State Electron. 14 (1971) 1167

[66] D.J. White et al.
Application of difference equations to a square Hall plate with finite interior driving and Hall electrodes
Journal of Applied Physics 44 (1973) 1870

[67] M. Yamashita
Geometrical correction factor for resistivity of semiconductors by the square four-point probe method
Japanese Journal of Applied Physics 25 (1986) 563

[68] E.J. Zimney et al.
Correction factors for 4-probe electrical measurements with finite size electrodes and material anisotropy: a finite element study
Meas. Sci. Technol. 18 (2007) 2067-2073

[69] D.S. Perloff
Four-point sheet resistance correction factors for thin rectangular samples
Solid State Electron. 20 (1977) 681

[70] M.G. Buehler and W.R. Thurber
Measurement of the resistivity of a thin square sample with a square four-probe array
Solid State Electron. 20 (1977) 403

[71] W. Versnel
ANALYSIS OF SYMMETRICAL VAN DER PAUW STRUCTURES WITH FINITE CONTACTS
Solid State Eleclron. 21 (1978) 1261-1268

[72] J. Weiss et al.
A derivation of the van der Pauw formula from electrostatics
Solid-State Electronics 52 (2008) 91-98

[73] J. Weiss
Generalization of the van der Pauw relationship derived from electrostatics
Solid-State Electronics 62 (2011) 123-127

[74] J. Weiss
Electrostatics analysis of two Hall measurement configurations
Solid-State Electronics 75 (2012) 37-42

[75] J. Shi and Y. Sun
New method of calculating the correction factors for the measurement of sheet resistivity of a square sample with a square four-point probe
Review of Scientific Instruments 68 (1997) 1814

[76] J.R. Brauer at al.
Finite Element Analysis of Hall Effect and Magnetoresistance
IEEE TRANSACTIONS ON ELECTRON DEVICES 42 (1995) 328-333

[77] D.B. Cuttriss
Relation Between Surface Concentration and Average Conductivity in Diffused Layers in Germanium
THE BELL SYSTEM TECHNICAL JOURNAL 40 2 (1961) 509-521

[78] S.S. Bennett and N.E.B. Cowern
Doping characterization for germanium-based microelectronics and photovoltaics using the differential Hall technique
Appl. Phys. Lett. 100 (2012) 172106

[79] N.E. Posthuma et al.
Emitter Formation and Contact Realization by Diffusion for Germanium Photovoltaic Devices
IEEE TRANSACTIONS ON ELECTRON DEVICES 54 (2007) 1210-1215

[80] J. Sharp et al.
A novel technique for degenerate p-type doping of germanium
Solid State Electron. 89 (2013) 146

[81] V. Sorianello et al.
Spin-on-dopant phosphorus diffusion in germanium thin films for near-infrared detectors
Phys.Status Solidi C 11 (2014) 57

[82] M. Nolan et al.
Boron diffusion from a spin-on source during rapid thermal processing
J. Non Cryst. Solids 254 (1999) 89

[83] A.Z. Al-Attili et al.
Spin-on doping of germanium-on-insulator wafers for monolithic light sources on silicon
Jpn. J. Appl. Phys. 54 (2015) 052101

[84] C.J. Brinker and G.W. Scherer
Sol-gel Science: the Physics and Chemistry of Sol-gel Processing
Academic Press, San Diego (1990) 515

[85] V. Boldrini et al.
Optimal process parameters for phosphorus spin-on-doping of germanium
Appl. Surf. Science 392 (2017) 1173-1180

[86] T.L. Chu and R.W. Kelm
The Etching of Germanium with Water Vapor and Hydrogen Sulfide
J. Electrochem. Soc. 116 (1969) 1261

[87] M. Inoue
Etching of Germanium with Water Vapor
Jpn. J. Appl. Phys. 11 (1972) 1147

[88] P.D. Maniar
US Patent n. 5817582 (1998)

[89] S.A. Kamil et al.
Characterization of Spin-on Dopant by Sol-gel Method
AIP Conf. Proc. 1017 (2008) 124

[90] J. Hwang et al.
Photocurrent Mapping in High-Efficiency Radial p-n Junction Silicon Nanowire Solar Cells Using Atomic Force Microscopy
J. Phys. Chem. C 115 (2011) 21981

[91] J. Livage
"Biological applications of sol-gel glasses" in: M.A. Aegerter, M.Mennig (Eds.), "Sol-gel Technologies for Glass Producers and Users" Kluwer Academic Publishers (2004) 399

[92] M. Guglielmi and G. Carturan
PRECURSORS FOR SOL-GEL PREPARATIONS
J. Non Cryst. Solids 100 (1988) 16

[93] R.M. Almeida and C.G. Pantano
Structural investigation of silica gel films by infrared spectroscopy
J. Appl. Phys. 68 (1990) 4225

[94] P. Innocenzi
Infrared spectroscopy of sol-gel derived silica-based films: a spectra-microstructure overview
Journal of Non-Crystalline Solids 316 (2003) 309-319

[95] P. Innocenzi
Densification of sol-gel silica thin films induced by hard X-rays generated by synchrotron radiation
J. Synchrotron Radiat. 18 (2011) 280

[96] A. Fidalgo and L.M. Ilharco
Chemical Tailoring of Porous Silica Xerogels: Local Structure by Vibrational Spectroscopy
Chem. Eur. J. 10 (2004) 392

[97] L. Todan et al.
Thermal behavior of silicophosphate gels obtained from different precursors
J. Therm. Anal.Calorim. 114 (2013) 91

[98] D.P. Poenar et al.
lnfrared Spectroscopic Analysis of Phosphosilicate Glass Films for Micromachining
J. Electrochem. Soc.143 (1996) 968

[99] H.J. Lee et al.
Characteristics of silicon solar cell emitter with a reduced diffused phosphorus inactive layer
Curr. Appl. Phys. 13 (2013) 1718-1722

[100] M. Zaharescu et al.
Hydrolysis-Polycondensation in Binary Phosphorus Alkoxides-TEOS System Studied by GC-MS
J. Sol-Gel Sci. Technol. 8(1997) 59

[101] M. Anastasescu et al.
Loss of phosphorous in silica-phosphate sol-gel films
J. Solgel Sci. Technol. 40 (2006) 325

[102] N. Ioannou et al.
Germanium substrate loss during low temperature annealing and its influence on ion-implanted phosphorous dose loss
Appl. Phys. Lett. 93 (2008) 101910

[103] S. Chapman and T.G. Cowling
The Mathematical Theory of Non-uniform Gases
Cambridge University Press (1970)

[104] E.E. Haller et al.
Physics of ultra-pure germanium
Advances in Physics 30 (1981) 93-138

[105] T. Nishimura et al.
Evidence for strong Fermi-level pinning due to metal-induced gap states at metal/germanium interface
Appl. Phys. Lett. 91 (2007) 123123

[106] K. Gallacher et al.
Ohmic contacts to n-type germanium with low specific contact resistivity
Appl. Phys. Lett. 100 (2012) 022113

[107] J.Y. Spann et al.
Characterization of Nickel Germanide Thin Films for Use as Contacts to p-Channel Germanium MOSFETs
IEEE ELECTRON DEVICE LETTERS 26 3 (2005) 151-153

[108] A. Firrincieli et al.
Study of ohmic contacts to n-type Ge: Snowplow and laser activation
Appl. Phys. Lett. 99 (2011) 242104

[109] H. Miyoshi et al.
Low nickel germanide contact resistances by carrier activation enhancement techniques for germanium CMOS application
Jap. J. Appl. Phys. 53 (2014) 04EA05

[110] T. Grzela et al.
Growth and evolution of nickel germanide nanostructures on Ge(001)
Nanotechnology 26 (2015) 385701

[111] B. Sapoval and C. Hermann
Physics of semiconductors
Springer-Verlag (1995)

[112] G. Ottaviani et al.
Hole drift velocity in high-purity Ge between 8 and 220 K
J. Appl. Phys. 44 6 (1973) 2917-2918

[113] O. Golikova et al.
Sov. Phys. Solid State 3 10 (1962) 2259-2265

[114] C. Jacoboni et al.
Electron′ drift velocity and diffusivity in germanium
Phys. Rev. B 15 (1981) 1014

[115] P.P. Debye and E.M. Conwell
Electrical Properties of N-Type Germanium
Phys. Rev. 93 4 (1954) 693-706

[116] S. Prucnal et al.
Ultra-doped n-type germanium thin films for sensing in the mid-infrared
Nat. Publ. Gr. (2016) 1-8

Acknowledgments

The greatest thanks goes to my supervisor, Prof. Davide De Salvador, brilliant mind and great humanity, it was an honor to work with you.
Another great thanks goes to Prof. Enrico Napolitani, naturally for the help in interpreting results, but also for his inspiring proficiency and precision.
Then, I want to thank Dr. Sara Carturan, Dr. Gianluigi Maggioni and Dr. Daniel Ricardo Napoli, who have welcomed me to the Legnaro Laboratories as a friend when I was just a student, following me in experimental work and giving me valuable scientific and human teachings.
I am grateful to my office mates Ruggero Milazzo, Massimo Mastromatteo and Francesco Sgarbossa, loyal and trustworthy guys, always ready to listen and help. I will remember you forever, all laughs and discussions, especially on January 8th...
I want to thank Luca Bacci, Renzo Storti, Nicola Argiolas and Walter Raniero for their precious technical support and Adriana Schiavon for the friendship and joy she always brings with her.
To all friends met at the Physics Department, a huge thank you for the long carefree lunches, laughs and tales of life. Each of you left me something, a reflection, an inspiration, an emotion.
Last but not least, I would like to thank my family for teaching me the beauty of knowledge and nature. Maurizio, for his love. My friends because they are the best.